

UC Berkeley

UC Berkeley Electronic Theses and Dissertations

Title

Electron Dynamics and Symmetries at the Metal-Molecule Interface Probed by Two Photon Photoemission

Permalink

<https://escholarship.org/uc/item/9xb089pd>

Author

Muller, Eric Anton

Publication Date

2012

Peer reviewed|Thesis/dissertation

**Electron Dynamics and Symmetries at the Metal-Molecule Interface Probed by
Two Photon Photoemission**

by

Eric Anton Muller

A dissertation submitted in partial satisfaction of the
requirements for the degree of
Doctor of Philosophy

in

Chemistry

in the

GRADUATE DIVISION
of the
UNIVERSITY OF CALIFORNIA, BERKELEY

Committee in charge:
Professor Charles B. Harris, Chair
Professor Gabor A. Somorjai
Professor Roger W. Falcone

Fall 2012

**Electron Dynamics and Symmetries at the Metal-Molecule Interface Probed by
Two Photon Photoemission**

Copyright 2012
by
Eric Anton Muller

Abstract

Electron Dynamics and Symmetries at the Metal-Molecule Interface Probed by Two Photon Photoemission

by

Eric Anton Muller

Doctor of Philosophy in Chemistry

University of California, Berkeley

Professor Charles B. Harris, Chair

Femtosecond, angle resolved two photon photoemission spectroscopy is used as a probe of the metal-molecule interface. In four related investigations, monolayer or submonolayer coverages of a molecule are adsorbed onto an Ag(111) surface under ultrahigh vacuum conditions. Studies use an optically excited electronic probe to investigate to probe the energetic landscape experienced and the response of a molecular adsorbate to an excess charge. Energy levels, electronic population, and band structure reveal molecular structure and mechanisms of dynamic response to an injected charge.

Room temperature ionic liquids (RTIL), consisting of charge separated anions and cations, represent a new and poorly understood class of electrochemical solvents. The mechanism of electron solvation has been proposed to be vastly different at the electrode interface than has been observed in bulk studies. Optical excitation into the RTIL conduction band results in a localized excess charge, as measured by band dispersions. Electron solvation is measured directly as the photoemitted kinetic energy. Solvation by $200 - 540 \text{ meV}$ is found to occur rapidly on the timescale of 350 fs , supporting previous predictions of fast charge solvation at the interface. Further, a previously proposed phase transition is observed between a low temperature ordered phase and high temperature disordered phase. This phase transition, which occurs at 250 K , is quantified by both the change in workfunction and a change in the energy of solvation between the two phases.

The image state is often used as a sensitive probe of molecular films, however, the electronic potential experienced by the image state electron is poorly understood. Theoretical predictions of image state energy in molecular films with a positive electron affinity are often wrong by $1 - 3 \text{ eV}$, and descriptions of the band structure typically remain limited to a measurement of effective mass. An image state is investigated within a film of metallated phthalocyanines. Phthalocyanines crystallize laying flat on the substrate, with a nearly square unit cell of $14 - 15 \text{ \AA}$ on a side. Angle resolved measurements into the second Brillouin zone reveal folding of the image state due to interactions with the screened potential energy surface within the molecule. The bandgap, measured to be 150 meV , can be used to estimate the corrugation of the energy landscape. Further, a Kronig Penney model is quantitatively compared to the first several backfolded image bands. Comparison between theory and experiment reveals the effects of the fourfold symmetry of lattice on the image state bandstructure.

The morphology and crystal structure of thin film molecular semiconductors is well known to directly influence the band structure and electronic properties of the material. Further, several morphologies and crystal structures can result from epitaxial growth of a single molecule on a metal

surface. Although phase transitions in 2D-atomic systems have been well studied for over 80 years, molecular systems are less well understood due to their larger size and the complex interplay of relatively weak forces that govern the crystalline packing. Three phases of metallated phthalocyanines are studied as a function of substrate temperature and submonolayer coverage. Three phases, the 2D-gas phase, the low temperature commensurate phase, and the high temperature incommensurate phase, are each studied using TPPE and low energy electron diffraction. The image state is found to be an excellent probe of the local crystal structure and local workfunction. Preliminary studies focus on the temperature and coverage dependent energies and intensities of the image state peak in domains of each phase. Temperature dependent studies reveal a pseudo-isosbestic point in the transition from the low temperature commensurate to the high temperature incommensurate phases. Coverage dependence reveals a redshift of the image state with increasing molecular density and decreasing workfunction, and low temperature studies reveal long time scale kinetics of reorganization. Preliminary experimental results are interpreted with the aid of kinetic monte carlo simulations. Further studies will aim to obtain quantitative thermodynamics of these submonolayer coverages.

Two photon photoemission spectroscopy has proven to be a powerful tool for understanding basic surface physics of atomic and molecular systems. In particular, the image state has proven to be a powerful probe of the first $1 - 2 ML$ coverage of a molecular system. In order to improve the applicability of TPPE to answer device relevant questions, the technique will need to resolve, identify, and characterize molecularly derived bands and excitonic states. The basic selection rules for metal-molecule charge transfer excitations and exciton formation at a surface are understood, but it is not agreed upon whether hot-electrons or interfacial electronic coupling allow for excitations that break normal selection rules. Further, classical dipole quenching is expected to play a strong role in the exciton lifetimes in molecules adsorbed on metal or semiconductor surfaces, though no TPPE study up to this point has been able to observe the expected distance dependent lifetimes. In this final chapter, selection rules and classical dipole quenching are briefly discussed, and general trends are derived for molecular systems adsorbed on highly oriented metal surfaces. Our work up to this point suggests that selection rules are followed rigorously in molecular adsorbates on Ag(111).

To my family.

Contents

List of Figures	iv
List of Tables	vi
1 Introduction	1
1.1 Surfaces and Interfaces in Electronic Devices	1
1.2 Electronic States at Surfaces and Interfaces	3
1.3 Time and Angle Resolved Two Photon Photoemission	4
2 Experimental	8
2.1 Overview of TPPE Apparatus	8
2.2 Ultrafast Laser System and Electron Detection	10
2.3 Ultrahigh Vacuum Chamber and Sample Handling	12
3 Charge Injection in the Electrochemical Double Layer of Room temperature Ionic Liquids	16
3.1 Introduction	16
3.2 Experimental	17
3.3 Results and Discussion	18
3.4 Conclusions	22
4 Image State Band Folding in Phthalocyanines	25
4.1 Introduction	25
4.2 Experimental	25
4.3 Results	27
4.4 Coupled Quantum Well Model	33
4.5 Discussion	35
4.6 Conclusion	36
5 Phase Changes in Submonolayer Phthalocyanines	38
5.1 Introduction	38
5.2 Experimental	40
5.3 TPPE Results	40
5.4 Kinetic Monte Carlo Simulations	44
5.5 Kinetic Monte Carlo on a Discrete Lattice	46
5.6 Monte Carlo Results	47
5.7 Non-Equilibrium Kinetics	48
5.8 Future Work	49

6	Selection Rules and Classical Quenching at the Molecule / Metal Interface	52
6.1	Introduction	52
6.2	Orbital Symmetry and Optical Selection Rules	53
6.3	Identifying Excitons	56
	Bibliography	59
7	Appendix A	66
8	Appendix B	75

List of Figures

1.1	a) Diagram of a schematic of a poly-3-hexylthiophene (P3HT) / Phenyl-C61-butyric acid methyl ester (PCBM) Bulk Heterojunction photovoltaic. b) Diagram of a typical Organic Field Effect Transistor (OFET).	2
1.2	Caption for image state figure	3
1.3	Schematic of TPPE.	5
1.4	a) Energy versus momentum dispersion of an electronic band. b) Detection Scheme. c) Energy versus angle for localized and delocalized bands.	6
2.1	Schematic showing laser system, ultrahigh vacuum chamber, and sample preparation	9
2.2	Polarization dependence of photoemission	12
2.3	Determining crystal angle cut by TPPE.	14
2.4	Multicrucible effusion cell with a) electron beam heated crucible and b) knudsen cell crucibles.	15
3.1	TPPE of $[Bmpyr]^+[NTf_2]^-$ / Ag(111)	17
3.2	Schematic showing a) a molecular film of $([Bmpyr]^+[NTf_2]^-)$ on Ag(111). In TPPE a UV pulse excites an electron from the substrate into the molecular film, and a visible pulse photoemits it to a detector. An energy diagram b) shows the conduction band located 3.25 eV above the Fermi level.	19
3.3	Schematic of workfunction shift observed by TPPE.	20
3.4	A conduction band peak solvates dynamically a). Angle resolved spectra b) reveal a localized state. The rates of decay to the metal c) and solvation d) remain constant at low and high temperatures, while the total energy of solvation d) is much greater at 300 K than 130 K.	20
3.5	a) The work function shows a temperature dependent phase transition. The energy of the CB and high energy cutoff are constant with temperature. b) The transition between phases is also observed by the reorganizational energy of solvation	23
4.1	A): Phthalocyanine structure. M= Fe or Cu; R= H. B): Schematic of phthalocyanine lattice showing high symmetry directions. C) Predicted LEED for FePc/Ag(111). D) Experimental LEED for FePc/Ag(111).	26
4.2	Left: Simulated LEED spectrum for CuPc/Ag(111) produced by LEEDSIM simulation program. Rotated domains are visible as different shades of green dots. Right: Experimental LEED spectrum obtained for CuPc/Ag(111)	28
4.3	Commensurate and Point-On-Line growth of FePc and CuPc.	29
4.4	Wavelength surveys for FePc (left) and CuPc (right)	30

4.5	Fit to a spectra of 1 ML FePc/Ag(111) taken at 14. This angle is given as an example to show the $j=(1,1)$ (red) peak and $j=(2,1)$ (cyan) peak at similar intensities, while the $j=(3,1)$ / $(1,3)$ peak (purple) moves above the high energy cutoff. The scattering background was fit to an exponential (yellow). The total fit is shown in green, against the original, unsmoothed data shown in blue.	31
4.6	Schematic of TPPE. A pump pulse excites an electron from the Ag (light blue) into the FePc adlayer (light green) before photoemission. Energies are referenced to the vacuum level. B): Cut through of the modeled potential energy surface showing a series of quantum wells parallel to the surface. C): Band structure of the lowest several states, calculated along high symmetry directions.	32
4.7	Experimental band structure and photoemission intensity for FePc (A), CuPc (B), and predicted photoemission for FePc (C). Peak centers shown with blue circles. (D) Comparison between predicted observable band structure (black) and experimental peak fits (blue) with error bars 1/4 FWHM of the fit.	34
4.8	Anisotropy results in different dispersions and for the $j=(1,3)$ and $(3,1)$ bands as seen experimentally in FePc (A), and CuPc (B). Modeling predicts the $j = (1, 3)$ band to return below the HEC in FePc at high momenta (black dots), while it rises monotonically above the HEC in CuPc.	36
5.1	Dosing survey of Copper Phthalocyanine a) and Titanyl Phthalocyanine b).	39
5.2	Dosing survey of Copper Phthalocyanine a) and Titanyl Phthalocyanine b).	41
5.3	Image state probe of local work function of gas and island phase phthalocyanines.	42
5.4	Temperature dependent phase transition from the island to gas phase showing a pseudo-isosbestic point (a) and a shift in energy of the gas phase peak with increasing gas-phase density.	43
5.5	Slow kinetics of condensation at 0.1 ML coverage and 200 K. The gas-phase peak decreases in intensity due to condensation while the peak due to bare Ag(111) increases in intensity.	45
5.6	Monte Carlo results showing a) dosing dependent relative coverages of each phase and b) temperature dependence of the relative coverages of island and gas phases for 0.4 ML total dosing.	48
5.7	Hysteresis in the relative coverages of each phase upon dosing and removal indicates a nonequilibrium first order phase change.	50
6.1	a) Optical selection rules for CuPc / Ag(111). b) symmetry of the LUMO and LUMO+1. c) TPPE spectrum of the LUMO+1	54
6.2	Lifetimes from classical quenching of the top monolayer of thick films of ZnPc / Ag(111)	56
6.3	Exciton or low energy scatter of CuPc / Ag(111)	57

List of Tables

6.1	Correlation tables for gas phase and adsorbed CuPc and C_{60}	55
-----	---	----

Acknowledgments

First and foremost, I need to thank my family for the constant support, guidance, and nurturing. My parents have devoted themselves to raising my brothers and I, and I think that half of graduate school has been the application of things I learned at home before the age of 15. My brother Leland has been a great motivation, always going forth and doing great things, always achieving them with unprecedented excellence, and always pushing whatever he is doing to a next level, which was often unseen beforehand. I'd like to acknowledge my brother Scott, for his reminders that life isn't about what you're doing, or where you are, it's about the experience of doing it. I constantly need to remind myself, "why are you walking so fast?" and to, "stop and smell the roses, you know?" I continue to miss you every day.

I acknowledge my advisor, Charles Harris, who has encouraged an intellectually fruitful environment. I thank Charles for allowing me the freedom to pursue my scientific interests. Charles has nurtured a group of graduate students to act as a cohesive team in approaching any challenge.

I would like to thank Aram Yang and Matt Strader, for teaching me Two Photon Photoemission Spectroscopy. They have shown incredible patience with my plodding learning style. They have also shown me the importance of perspective in science, as they each approach similar scientific questions from very different angles. Their collective pedagogy was invaluable. To any of my numerous questions, Aram would inevitably hand me a book, and if I was still lost, Matt would just tell me the answer. This proved to be a fruitful (and entertaining) teaching method.

James Johns has also been an incredible personal mentor for my first four years of graduate school and beyond. During his time in the Harris lab, he maintained a critical eye at every moment, and kept up the intellectual rigor of the lab. James can always help me through my scientific questions, offer good new perspectives through his voracious reading, and he is always willing to put in the work to find and fix a problem when I've gone way off track. I can say this with all honesty, it is invaluable to have someone who you can count on to tell you you are wrong sometimes. James has also, through much effort, even taught me to occasionally think like a scientist.

The younger members of surface side have been wonderful to work with. Without Ben Caplans, I think all of our computers have irreparably broken years ago, and he has an uncanny ability to fix and upgrade any piece of electronics in lab. David Suich and Alex Shearer have also provided fresh new perspective and energy on every project. Our many discussions have really pushed me to rethink what it means to be have an interesting scientific question, and you have each been incredibly creative in addressing the problems that peak your intellectual curiosity.

I'd also like to thank the members of the Harris group with whom I haven't worked directly. My officemate, Karma Sawyer, really made the first two years of graduate school more bearable with laments about cabonyls, exclamations about the greatness of TAC, and the occasional glimpse of Fun Karma. Jacob Schlegel has made life better for everyone through his ability to cook everything we've never heard of, well, and then bring it in to share. Matt Zoerb has been and a great friend, in lab and out, keeping me simultaneously grounded and entertained with his anecdotes of Tennessee, bobcats and miniature donkeys. Son Nguyen has provided a great perspective on life in the Real World, while Justin Lomont has provided a great perspective on life at the Jersey Shore. I'd also like to thank Adam Hill, who is always happy to share his heartfelt opinion about everything.

I'd like to thank Charles Biddle-Snead. Charles has been constant friend, and I think it has been a group effort to maintain a level of stability and sanity as we have both struggle through graduate school, so far from home. Charles has led me through the nuanced links from a physical constant, to a line of code, to the electrical and chemical communications from one cell to its neighbor, to the social importance of a vintage barcade, to the simple joy of turning it all off and running in a big circle for an hour or two.

Finally, Anne Perring has opened my eyes to a bigger world. Anne has an amazing energy in everything she does, from treks through the wilderness to traversing the globe in the hopes of saving humanity. Anne has (re)introduced the concept of hobbies and outside interests into my life, waiting with her bike at the top of the hill when I'm slow, carrying me across the peaks of the Sierras when I'm too tired, all the while reminding me there is a reason we came to grad school, and showing me you can really help the world if you try.

This work was supported by the Director, Office of Energy Research, Office of Basic Energy Sciences, Chemical Sciences Division of the U.S. Department of Energy, under Contract No. DE-AC02-05CH11231.

Chapter 1

Introduction

1.1 Surfaces and Interfaces in Electronic Devices

Future energy needs require the development of new, carbon neutral, and renewable energy technologies. Photovoltaics will likely be a major component of energy production in a future economy, because solar irradiation is one of the only renewable sources with the required output capacity. Solar energy has, up to this point, not been utilized on a broad scale due to the prohibitive cost of crystalline Silicon and moderate efficiencies achieved in current generation devices. Silicon solar cells, for example, have relatively high efficiencies near 20%, but are too costly on a large scale. Organic photovoltaics (OPV), on the other hand, are inexpensive and can be roll printed for large scale production, but suffer from very poor efficiencies of only 6 – 10% in the laboratory setting. Efficiency limitations result from inadequate open circuit voltage and short circuit current. Much of this can be tied to bulk properties, including low charge mobilities. While Silicon has charge mobilities near $900 \text{ cm}^2/Vs$, typical small molecules have mobilities of 1×10^{-2} – $1 \times 10^2 \text{ cm}^2/Vs$, and polymeric materials have mobilities in the range 1×10^{-7} – $1 \times 10^{-4} \text{ cm}^2/Vs$. If polymeric photovoltaics mobilities could be increased one to two orders of magnitude their use would be widespread in scientific and industrial applications.

States existing at the interface present another major limitation to implementation of organic photovoltaics and organic electronic devices. In a photovoltaic cell, charge transfer from the n-type material to the p-type material is defined by the band alignment and electronic coupling at the interface between the two materials. Band alignment in photovoltaics is dependent on the band gap of each material, the ionization potentials in vacuum, built in molecular dipoles, and the density of free charge carries. Surface induced trap sites can also appear both at the interface between the two materials and the grain boundaries between crystallites of the same chemical identity. Trapped electronic states at grain boundaries are known to limit charge mobility, and they have more recently been shown to induce quenching of excitons via coupling to the electronic dipole. The importance of interfaces becomes particularly important in plastic photovoltaics relying on bulk heterojunctions 1.1. In plastic materials, the exciton cannot migrate more than a few nm before decaying. This dictates the necessity for complex, highly nonplanar interfaces, and bulk regions no more than 10 – 20 nm wide. Further, the low crystallinity of these materials creates a high density of grain boundaries and trap sites.

Electronic properties at the molecule-metal and molecule-inorganic interfaces also determine both the functionality and the efficiency of several current and emerging technologies. At the heterogeneous interface, an electron can be injected from the substrate into a molecular adsorbate. In an organic light emitting diode, for, example, the band alignment between the metal and the

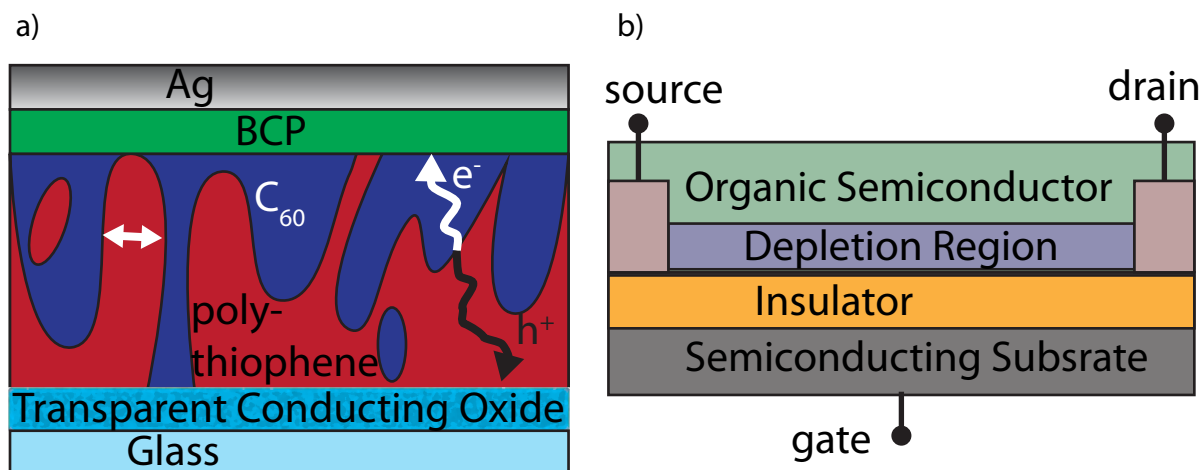


Figure 1.1: a) Diagram of a schematic of a poly-3-hexylthiophene (P3HT) / Phenyl-C61-butyric acid methyl ester (PCBM) Bulk Heterojunction photovoltaic. b) Diagram of a typical Organic Field Effect Transistor (OFET).

organic semiconductor determines the charge injection efficiency, and this is known to effect the overall performance of the device[91]. Organic field effect transistors (OFET) are also becoming more competitive with their inorganic counterparts. Figure 1.1 shows a typical OFET. In this device, a gate voltage controls the availability of free carriers in the organic semiconductor. Conductivity through the organic semiconductor region occurs only through the depletion region, which extends only a few molecular layers into the organic semiconductor. As a result, interface and trap states existing in the first few molecular layers near the insulator and near the source and drain electrodes are integral to the performance of the device. The most efficient OFET have been designed using single-crystal materials with high carrier mobilities.

In devices grown via molecular beam epitaxy, the growth of the first monolayer will affect overall performance. The first monolayer may have a crystal structure different from the subsequent layers. Further, in many cases, the crystal structure of the first monolayer is known to template the crystalline growth of subsequent monolayers. In molecular epitaxy, three main growth modes are considered. In layer-by-layer growth, molecules typically do not have enough energy to translate across the interface, and growth occurs randomly with new molecules stacking upon lower layers. In island-type growth, the binding to the substrate is much weaker than the binding between molecules, and molecules will translate across the surface, clustering together into clusters, droplets, or needle crystals. In wetting-layer plus island, the molecules have a stronger binding energy to the substrate than to each other, and they will form a uniform uniform monolayer or bilayer. Growth beyond the first monolayer, however, occurs in an island type fashion.

In addition to the macroscopic morphology, the intermolecular coupling in each growth mode can be very different. Because layer-by-layer growth mode is often characterized by a minimal available for reorganization, molecules will typically pack in a non-crystalline manner with weak intermolecular coupling. Further, intermolecular binding energies are typically weak and competitive with steric hindrance, the energies associated with commensurate and incommensurate packing with respect to the substrate, and kinetic or entropic effects. As a result of these competing factors, several surface crystal structures are often possible within a growth mode depend upon sample preparation conditions.

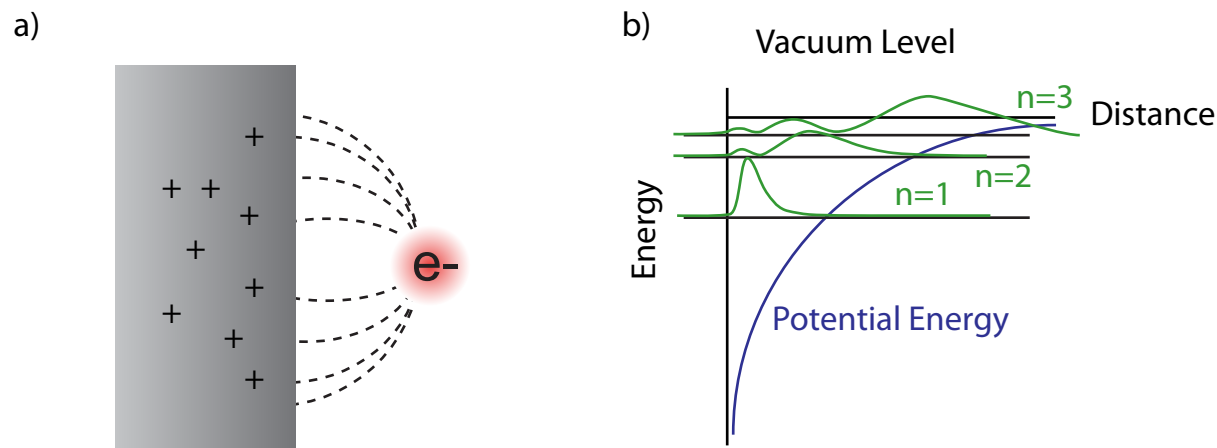


Figure 1.2: Caption for image state figure

1.2 Electronic States at Surfaces and Interfaces

Interface states include both molecular HOMO and LUMO derived states as well unoccupied image potential states (IPS) and occupied surface states. The IPS is a state that occurs above well-ordered, highly polarizable surfaces, and it has proven to be a strong and reliable probe of the electronic landscape in the immediate vicinity of the surface.

The image state results from the polarization induced in a conductive surface^{1,2}. As an electron approaches a metallic surface, electrons at the surface reorient themselves to expose the positive potential of the underlying nuclei. For a perfectly conducting surface, if electric field emanating from the electron were to have a component parallel to the surface; this results in a movement of electronic charge within the substrate. Solving Poisson's equation, the resulting charge within the metal substrate is equivalent to a positive charge of equal charge to the electron and an equal distance in the metal. This results in an attractive potential proportional to the inverse of the electron's distance from the surface. In analogy to a Hydrogen molecule, a one-dimensional rydberg series of bound states forms, extending out from the surface^{1,2}. For a clean metal, the allowed states have energies:

$$E_n = \frac{-0.85eV}{(n+a)^2} + V_0 \quad (1.1)$$

The IPS state can act as a good probe of thin molecular adsorbates because of its close proximity to the surface. On a clean metal, the $n = 1$ IPS has a probability density with a typical distance of 3 Å from the metal, while the $n = 2$ state resides 10-12 Å from the metal. In the absence of competing effects, the $n = 1$ IPS will act as an excellent probe of the first several atoms thickness of an adlayer.

The lifetime of the image state is directly proportional to its electronic coupling to bulk states in the substrate. At the surface of an atomically smooth metal orient to expose a high symmetry plane, surface band gaps appear. In cases where the allowed energy of the image state is within the surface bandgap, the the lifetime of the IPS is extended dramatically compared to bulk metal states. For Ag(111), the $n = 1$ image state is found within the surface bandgap, and it is measured to have a lifetime of 22 fs. The $n = 2$ -inf image states lie above the surface bandgap. The competition between a decreased barrier to electronic coupling with the bulk and having a

probability maximum farther from the surface results in a slightly decrease lifetime of $22 fs$ for the $n = 2$ state.

An image potential state above a clean metal is typically delocalized in the plane of the surface. Because there forces parallel to the plane of the surface, electrons bound by the image potential normal to the surface will retain a free-electron-like dispersion along the two dimensional surface. Localization of the IPS may result from electron injection into a defect site, with a local potential energy landscape differing from that of the rest of the surface[25]. Here the electron is injected directly into a localized state. The IPS electron may also reside in an initially delocalized state that later becomes localized[49]. This occurs dynamcally through trapping in self-induced potentials. An initially delocalized electron will interact with either a local molecular dipole or induced dipole. This causes the electron to begin to localize near the lower potential of the trapping site[73]. As the electron begins to localize, increased interactions with the local solvent dielectric cause further reorientation of nearby solvent molecules and further shrinking of the electronic wavefunction.

The dynamic localization of an electronic wavefunction is often accompanied by a corresponding shift in the energy level of the state, or solvation, as the nearby molecules rearrange their dipoles into more favorable orientations[4]. In many cases, and increased tunneling barrier back to the metal surface results. The lifetime of electrons localized in trap sites has been found to increase exponentially as a function of well depth. As a reult, IPS bound deep traps have lifetimes lasting several picoseconds or longer.

1.3 Time and Angle Resolved Two Photon Photoemission

Two photon photoemission spectroscopy is used to investigate occupied and unoccupied electronic states at the molecule-metal interface. This technique has the advantage of surface sensitivity and the ability to measure the full bandtstructure of electronic states with femtosecond resolution.

In this technique, a pump pulse from a femtosecond laser pulse, with energy $h\nu_1$ stimulates an electronic excitation to an initially unoccupied energy level, referred to as the intermediate state. After a variable delay time, a probe pulse $h\nu_2$ excites the intermediate state to a continuum level about the vacuum level. The final state is a free-electron plane wave, and the energy of the final state energy is measured by a detector.

By subtracting the energy of the probe pulse energy from the measured kinetic energy, the intermediate state energy can be determined. In cases where $h\nu_1$ and $h\nu_2$ have different energies, a wavelength survey is performed to identify the pump and probe pulse. The slope of the measured kinetic energy versus the photon energy of the probe pulse will have a slope of one. In the case where photoemission results from a two photon process, the slope will equal the sum of the energies of the two pulses.

The workfunction can also be measured by two photon photoemission by two possible methods. In the first, the wavelength of the probe pulse is varied over a range near the workfunction of the sample. The workfunction is measured by the onset of single photon photoemission. In the second method, the energy range of nonresonant excitations is measured. Nonresonant excitations are allowed through excitation to scattering states. The high energy cutoff of the nonresonant background in two photon photoemission corresponds to the energy of the Fermi level plus the sum of $h\nu_1$ and $h\nu_2$ photon energies. Similarly, the low energy cutoff corresponds to the vacuum level. Subtraction determines the workfunction.

An electron interacting with a periodic solid is a quasiparticle with an effective mass m^*

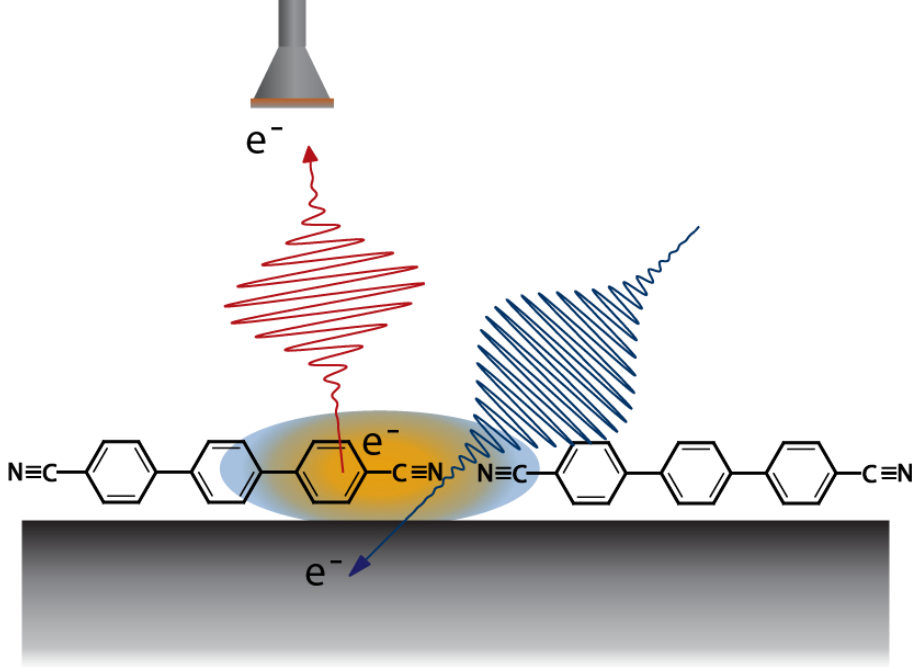


Figure 1.3: Schematic of TPPE.

with a dispersion measured relative to the dispersion of a free electron m_e . An electronic state with only weak interaction with the material is expected to have an effective mass near unity, which can be measured by the energy versus momentum of the state, also referred to as the band curvature, as shown in Figure 1.4. Within increasing lattice interaction, this effective mass is expected to increase, with an effective mass of infinity (flat band) corresponding to a completely localized state.

Angle-resolved measurements are used to observe the band structure or localization of an electron in a manner analogous to photoemission spectroscopy. An electron ejected from the surface will have a momentum perpendicular to the surface, k_{\perp} , as a result of its energy above the vacuum level, plus an additional momentum parallel, k_{\parallel} . Because light carries a negligible momentum compared to that of the electron, the momentum of the electron parallel to the surface after photoemission is the same as that before the probe pulse interacts with the electron. Angle resolved measurements are performed by rotating the angle of the sample relative to a stationary detector as shown in Figure 1.4 b). The energy versus momentum dispersion relation characterizes the band structure and coupling in a material. The angle, θ , and momentum parallel to the surface, k_{\parallel} , of the photoemitted electron are related by the measured energy $E_{\text{photoemitted}}$ and the mass, m_e , of an electron:

$$k_{\parallel} = \sqrt{\frac{2 \cdot m_e \cdot E_{\text{photoemitted}}}{\hbar^2}} \cdot \sin(\theta) \quad (1.2)$$

The angle θ is measured relative to surface normal, which represents the $\bar{\Gamma}$ point in the Brillouin zone. The measured effective mass is subsequently used to determine the localization or delocalization of the sample.

An angle resolved measurement of an initially delocalized state will provide the two dimensional band structure of that state. In a localized state, however, k_{\parallel} is no longer a good quantum number, and a localized electron can be represented by localized a wavepacket composed of a super-

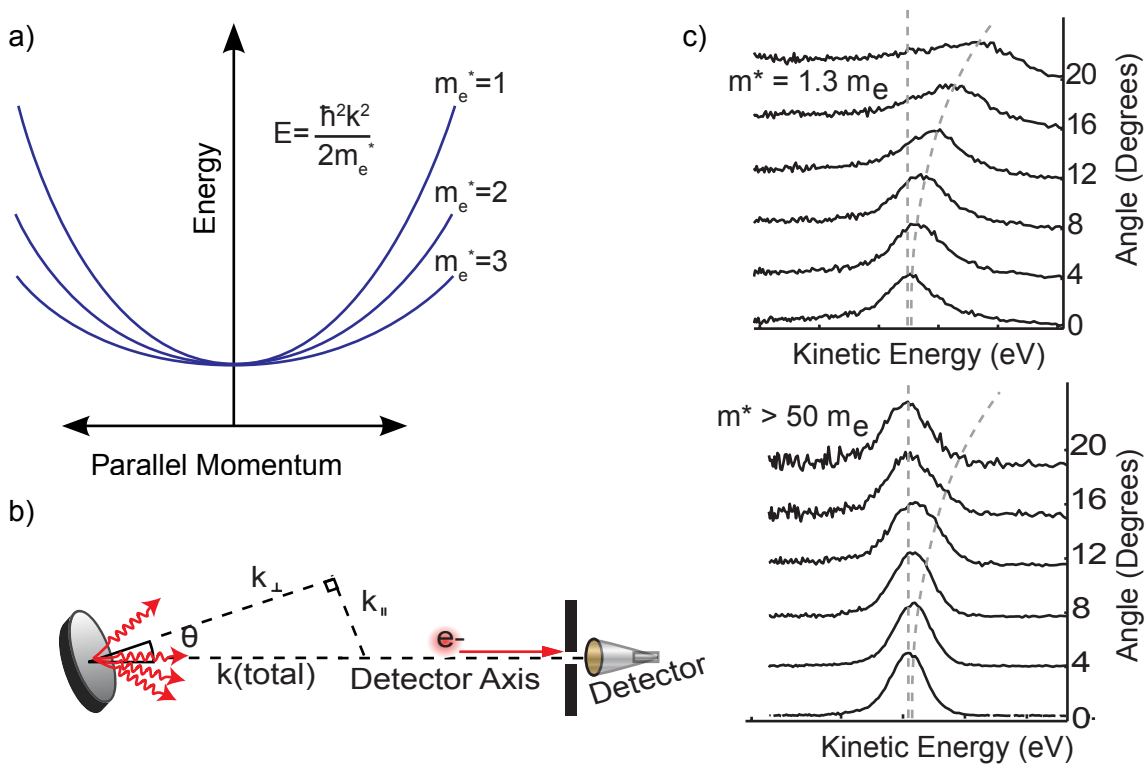


Figure 1.4: a) Energy versus momentum dispersion of an electronic band. b) Detection Scheme. c) Energy versus angle for localized and delocalized bands.

position of plane waves. A measurement of the population of a delocalized electron versus parallel momentum maps the distribution of plane waves, the fourier transform of which is the spread of the wavefunction in two dimensions[59]. Using angle resolved two-photon photoemission we are able to characterize both the two-dimensional band structure of delocalized electrons and the momentum representation electron localization at a surface. Finally, time resolved measurements of an electronic state, show that the band structure is not a static parameter. The collapse of an electron from a delocalized to a localized electronic state can occur due to, for example, localization on a trap site or small polaron formation.

Chapter 2

Experimental

2.1 Overview of TPPE Apparatus

Two photon photoemission is a surface sensitive technique uniquely capable of interrogating electronic levels of the metal-molecule interface. In this technique, a pump pulse excites an electronic excitation from below the Fermi level to an initially unoccupied state above the Fermi level. After a variable delay time, the electron is photoemitted to a detector. The energy measured at the detector can be directly related back to the energy of the electron before photoemission by subtracting the known energy of the photoemitting laser pulse.

The apparatus required for this type of investigation can be broken into two parts, the spectroscopic apparatus, consisting of a laser and detector, and the sample handling apparatus, consisting of vacuum chambers for substrate and adsorbate preparation. An ultrafast laser system is required to excite the electron first into an unoccupied level and then to couple this intermediate state to the continuum of states above the vacuum level. The surface sensitivity of this experiment stems partly from the short mean free path of a photoemitted electron. An ultrahigh vacuum chamber is thus required to house the sample. A typical chamber pressure of 2×10^{-10} torr ensures that an electron with a typical photoemitted kinetic energy of 1 eV will not scatter off residual gas in the detection flight tube. Further, low pressure is required to ensure sample cleanliness, especially at the low temperatures where sticking coefficients may be high for molecules in the chamber. At pressures in this range, the sample will remain clean for a minimum of 3 hours assuming unit sticking coefficient of residual gases (Langmuir conditions), and it is found to remain clean for at least 24 hours while cooled with liquid nitrogen. Finally, the sample itself must be on a conducting substrate, and a single crystal substrate is required for the highly ordered samples necessary. Samples are typically grown using molecular beam epitaxy. It is found that molecular beam growth from a Knudsen cell in a side chamber is sufficient to produce highly ordered morphologies and layer-by-layer growth.

The basic setup for our apparatus is shown in Figure 2.1. Here, a tunable laser excites an electronic energy level in the sample, followed by photoemission to the time-of-flight detector. A single crystal Ag(111) substrate is housed in a vacuum chamber. A Knudsen cell is used to dose molecular samples onto the substrate. This is housed in a side chamber backed by a turbo pump, which can be separated from the main chamber by a gate valve. Other standard surface science analysis methods are also included on the main chamber including low energy electron diffraction (LEED), Auger spectroscopy, and temperature programmed desorption.

The details of our apparatus has been discussed in detail in several theses. The range of apparatus used for two photon photoemission spectroscopy is also exhaustively discussed in the

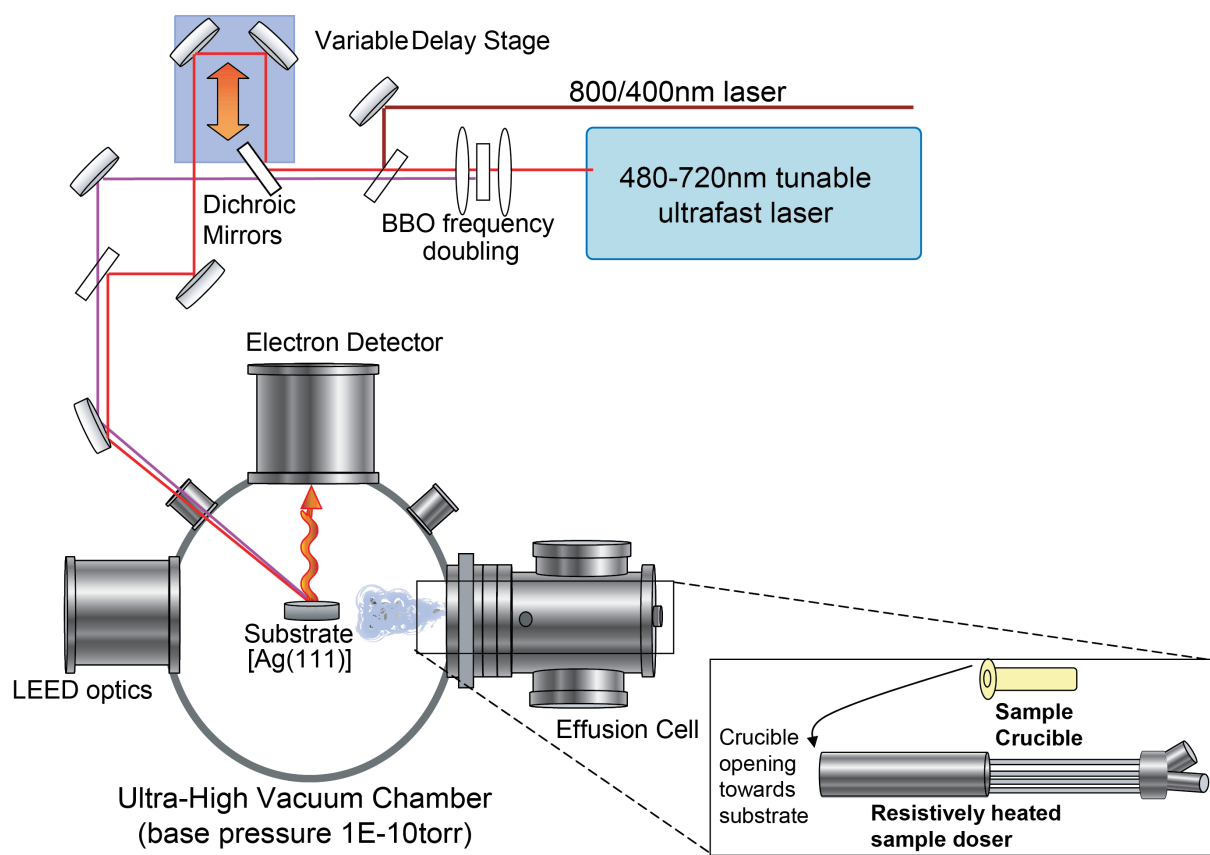


Figure 2.1: Schematic showing laser system, ultrahigh vacuum chamber, and sample preparation

literature. We review here the requirements necessary for obtaining high signal-to-noise two photon photoemission, as well as the sample preparation techniques used to obtain high purity, uniform and ordered molecular films. We will focus on sources of error in our instrumentation as well recent additions to the apparatus.

2.2 Ultrafast Laser System and Electron Detection

The laser source used for these experiments is a commercially available Ti:Sapph system available from Coherent. Here a 5.5 Watts of 532 nm CW laser light from a Verdi V-18 are split off by a dichroic mirror to pump a Mira 900 oscillator. This results in a short pulsed source operating at 76 MHz with a center wavelength of 800 nm. The remaining 12.5 W of light from the Verdi pump laser are used to pump a Rega 900 amplifier, seeded by the Mira. The Rega is capable of outputting $6 \mu J$ pulses at a repetition rate of 225 or $7 \mu J$ at 100 kHz.

The high repetition rate of this laser is required for our setup due to the use a time-of-flight detection scheme with a single microchannel plate electron detector. The time-of flight electronics rely on a start pulse provided by a laser pickoff mirror and photodiode, which is correlated with a known time zero. A constant fraction discriminator (Tennelec TC455) then picks out a voltage spike from the an anode at the back of the multichannel plate detectors which acts as a stop pulse. The time between the start and stop pulses is measured by a Canberra 2043 time-to amplitude converter. This time is stored as a single count in a multichannel analyzer.

This detection scheme requires a high repetition rate laser source for several reasons. First, space charge effects can affect the observed energy of the counted electrons if too many electrons are present at once in the $13.5cm$ flight tube. The timing electronics are also only capable of detecting a single electronic stop pulse per start pulse. If two electrons are photoemitted by the probe pulse, only the higher energy of the two will be detected. As a result, the number of two electrons must be kept low. Because the probability of photoemitting a second electron is equal to the probability of the first, a photoemission rate of $1/10$ the pulse rate will result in a 1% double count rate. This limits count rates to be a maximum of $22kHz$.

The multichannel analyzer (Ortec 918A Adcam Multichannel Buffer) also has a finite response time of $12 \mu s$. This response time is approximately three times the time between pulses of the laser. In order to maintain proper intensity information, this additional time, during which stop pulses cannot be detected, is recorded as a dead time and added to the end of the scan. With this buffer, significant dead times occur at higher repetition rates, resulting in diminishing detection efficiency at higher repetition rates. The maximum effective count rate of this system is only 10 kHz. In order to overcome this, a faster multichannel analyzer (Ortec 927 Multichannel Analyzer) was installed, with a response time of only $2 \mu s$. This has significantly reduced dead times, and count rates above 30 kHz are achievable on clean Ag(111) without either diminished detection efficiency or measurable experimental artifacts.

The pump pulse of the laser is used to excite an electronic transition in the sample, while the probe pulse photoemits the electron. The probability of excitation followed by photoemission is dependent of the pump pulse multiplied by that of the probe. In the case of one photon photoemission, however, the photoemission intensity is dependent on the intensity of a single pulse. In the case where the probe pulse has greater energy than the workfunction, one photon photoemission is allowed, and the intensity of this process is much greater. Because of both the limited count rate and the possibility for space charge broadening in the flight tube, the photon energy is typically kept below the workfunction of the sample.

This is not a fundamental limitation of two color two photon photoemission. Under condi-

tions where the pump pulse is the high energy pulse, the probe pulse can be made several orders of magnitude more intense than the pump pulse without inducing space charge effects on the surface of the sample. Here two photon photoemission is competitive with one photon photoemission, and both signals can be seen. These conditions are often hard to achieve, however, and a hemispherical energy analyzer with a 2D detector is typically used, which have acceptance rates of 150 kHz or greater. In our case, both pump and probe pulses must be kept below the energy of the work function.

In order to tune the energies of the two pulses, the output of the amplifier pumps a optical parametric amplifier (Coherent OPA 9400). Tuneable visible pulses are needed to excite resonant or nonresonant electronic excitations in the sample or across the metal-molecule interface of the sample. This OPA is capable of producing 60-100 fs pulses, tuneable between 480 and 720 nm, with a typical pulse energy of $100nJ$. In typical two color TPPE, the fundamental pulse is then frequency doubled in a B-Barium-Borate (BBO) crystal to produce a UV pulse. These pulses act as the pump and probe pulses in a TPPE experiment.

This experimental setup is ideal for examination of image potential states on samples with intermediat (3.8-4.9 eV) workfunctions. For samples with low workfunction or samples in which a bandgap greater than or equal to half the work function is probed, these wavelengths are unsuitable. The laser setup has been recently modified to allow more wavelength control in these experiments. Attempts were made to try to run two OPA's in parallel, however, it was found that this was untenable given the low pulse powers from the amplifier. Instead, alternate laser lines have been added of the first, second, and third harmonic of the RegA output. These laser lines (800, 400, and 267 nm) can be used as pump or probe pulse in combination with the fundametal or frequency doubled output of the OPA. These new laser lines add substantial tunability to the laser system while maintaining laser power and stability.

TPPE is typically performed with p-polarized light. Selection rules for photemission require that the probability of photoemitting an electron is dependent upon the surface normal component of the electric field vector. This is shown in Figure 2.2. Here, a $\lambda/2$ polarizer is used to rotate the polarization of the probe pulse. The photoemission intensity of the $n=1$ image state is plotted versus the probe polarization, showing a good fit to the expected Cos^2 intensity prediction. It is found that less than 5% of the intensity remains with s-polarized photoemission. Similar polarizers are used to control the polarization of the pump pulse. A metal-molecule charge transfer excitation, such as and excitation to an image state, also requires p-polarized light. The polarization dependence of measured intensity can be used to aid in identification of electronic peaks.

The ultimate energy resolution required by this experimental setup should be ideally comparable to thermal energy of the sample, which is approximately 12 meV at the base temperature of 120 K. The resolution of the laser setup is determined by errors in time of flight detection and the bandwidth of the laser. The bandwidth of the laser is typically near 30 meV. This bandwidth is an table comprmise between time resolution and energy resolution for a near bandwidth limited pulse. To first order, error in time-of-flight results from the sub-nanosecond time resolution, the flight tube length of 13.5 cm, and the sample position stability of approximately $100 \mu m$. These result in an error of less than 10 meV for a typical pothoemitted electron kinetic energy of 1 eV.

An additional error arises for angle resolved measurements, due to the finite acceptance angle of the detector. The detector consists of a matched pair of multichannel plates and a copper anode, with diameters of 40 mm. These are placed behind a machined slit in the flight tube in order to improve energy resolution. The acceptance angle of this slit is $\pm 1.5^\circ$ in the direction of crystal rotation and $\pm 4^\circ$ in the direction perpendicular to the direction of crystal rotation. For a

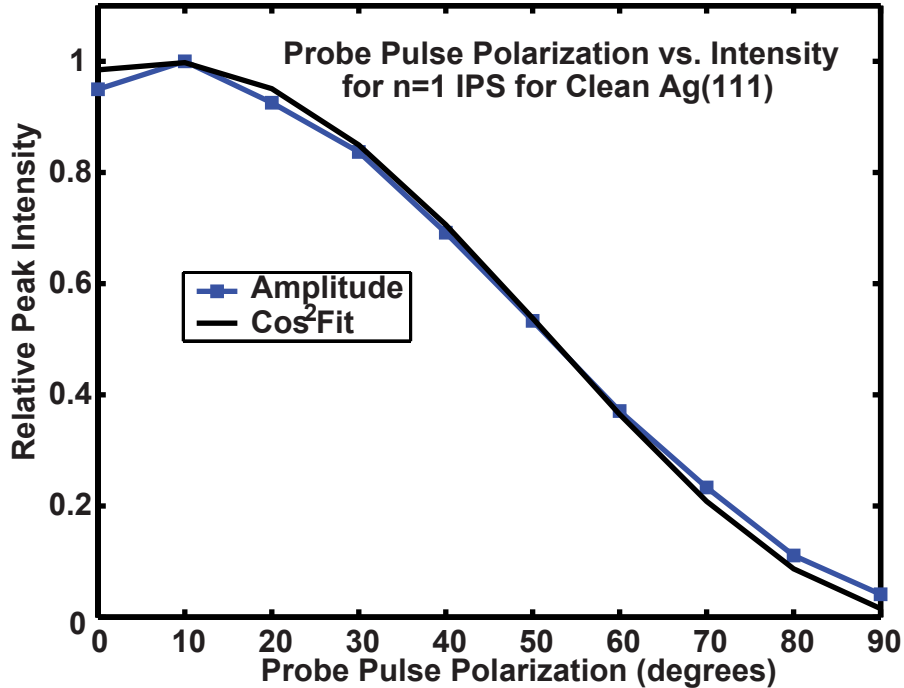


Figure 2.2: Experimentally observed photoemission intensity versus probe pulse polarization (blue) and theoretical intensity (black).

1 eV electron, this results in an acceptance of $\pm 0.05 \text{ \AA}^{-1}$ at the $\bar{\Gamma}$ point. For an electron with a parabolic band curvature, this does not lead to a measurable energy broadening at the $\bar{\Gamma}$ point. At crystal high angles of up to 26° , the error due to finite angular acceptance is only 10 meV for a state with a dispersion equal to that of a free electron and kinetic energy of 1.5 eV. Error due to finite angular acceptance remains less than the thermal energy, and can typically be ignored in this experiment.

2.3 Ultrahigh Vacuum Chamber and Sample Handling

The sample substrate, a 12.5 mm diameter single crystal Ag(111) disc, is held at the end of a 5 axis manipulator arm. The manipulator arm is used to orient the sample towards the time of flight tube for TPPE spectroscopy. The sample can also be rotated towards different ports for standard surface science analysis techniques including Low Energy Electron Diffraction Spectroscopy (LEED), Auger Spectroscopy, Temperature Programmed Desorption, and more recently, Kelvin Probe. An atomically clean substrate is prepared by Ar^+ sputtering. The sample is held at 500 K while Ar^+ ions bombard the sample with a voltage of 500 V for 20 minutes, followed by annealing the sample at 725 K for 20 minutes. Sample cleanliness is determined by a combination of Auger and LEED. The density of defects and terraces is examined semi-quantitatively by performing angle and time resolve TPPE. The image state is known to scatter off terraces and step edges, and a high density of step edges increases the effective mass of the image state relative to the known effective mass of $1.3 m_e$.

Although the sputtering process is highly effective in preparing atomically smooth Ag(111) from a relatively smooth and flat sample, or in removing organic materials, defects can develop

and propagate. Sputtering by 1000 V ions is necessary to remove some organic films, such as fullerenes, and this often causes deeper defects. These defects will occasionally grow rather than anneal out during subsequent cleaning procedures, resulting in patches with visible white haze. Visually similar defects propagate on the surface due to alloys or surface alloys formed with metal films that are grown on the sample.

Cleaning of an Ag substrate sample with deep defects is not possible by Ar^+ sputtering and annealing procedures. Here the two options are replacement of the substrate with a new crystal or manually polishing the crystal outside of vacuum. Because crystals must be custom grown and machined, this option is significantly less cost and time effective. A procedure was developed to repolish old Ag crystals, following literature guidelines for cleaning of single crystal metals.

A glass plate is first prepared with a vacuum compatible MoO paste as a slip film. The Ag(111) sample is placed on the slip film with the side to be polished facing the glass plate. A custom machined and polished aluminum cylinder was manufactured with an inner hole slightly larger than the diameter of the Ag disc and height approximately twice the thickness of the Ag. The aluminum cylinder serves as a polishing plate to align the Ag against a polishing wheel. These two were both clamped against the glass plate, using soft plastic clamps to prevent damage. A thermally softening glue (Crystal Bond) was melted onto the Ag and aluminum. After cooling, the Ag substrate, aluminum cylinder, and plastic tip of the clamp are firmly glued together. The removable plastic tip serves as a grip point for handling.

The first step in polishing is wet-sanding on a piece of 600 grit sandpaper adhesively mounted on a glass plate. This leaves a flat, though rather rough surface. After this, the sample is polished on a 12 inch polishing wheel rotating at 360 rpm. The sample is polished with successively smaller diamond paste: 6, 2, 1, and $0.25 \mu m$. Transfer of grit between successive steps results in deep, irremovable grooves. Between each polishing step, the sample is cleaned twice by sonication, for 5 minutes each, in deionized water. Sonication heats the water, and warm water is found to melt the glue, so care must be taken to keep the water cool. A new polishing wheel is necessary for each polishing step, and gloves must be changed at both the start and end of each polishing step. In the final step, the sample is released from the glue and aluminum ring using acetone. The sample is subsequently sonicated briefly in water and methanol to remove any remaining glue or other contaminants. It is typical at the end of metal polishing to etch the sample with potassium dichromate. This was found to diminish the mirror finish of the substrate, and it is not necessary unless long term storage of the crystal under atmospheric conditions is a goal.

The procedure leaves some room for having a high terrace density due to a misorientation of the Ag(111) surface relative to the polishing well. A high defect density results in poor surface ordering of thin film samples, and can be measured by the effective mass of the $n=1$ image state. Further, the samples are originally machined with a wedge of $7^\circ \pm 0.5^\circ$ on the back edge to increase the angular range of our TPPE experiment. We have found experimentally that the wedge machining tolerance is much greater than this, and wedge angles $6 - 9^\circ$ are common. Angle resolved TPPE must be performed to find both the curvature and minimum of the parabola. These are plotted for a polished crystal in Figure CutAngle. The minimum of the parabola corresponds to a cut angle of $8^\circ \pm 1^\circ$. The effective mass of $1.97 m_e$ fit here is slightly higher than the expected mass of $1.3 m_e$ and improved upon subsequent sputter and anneal cycles. TPPE measurements confirm a successful method for repolishing Ag substrate crystals.

Thin films of molecular semiconductors are typically grown using a molecular beam from a Knudsen cell. Langmuir dosing through a leak valve is also used in the case of volatile organics. Knudsen cell dosing can be qualitatively compared to Langmuir dosing in which a solid or powdered sample is heated in a crucible in order to increase the vapor pressure of the material. Using a Boltzmann or Arrhenius analysis, one can calculate that the vapor pressure of a given material will

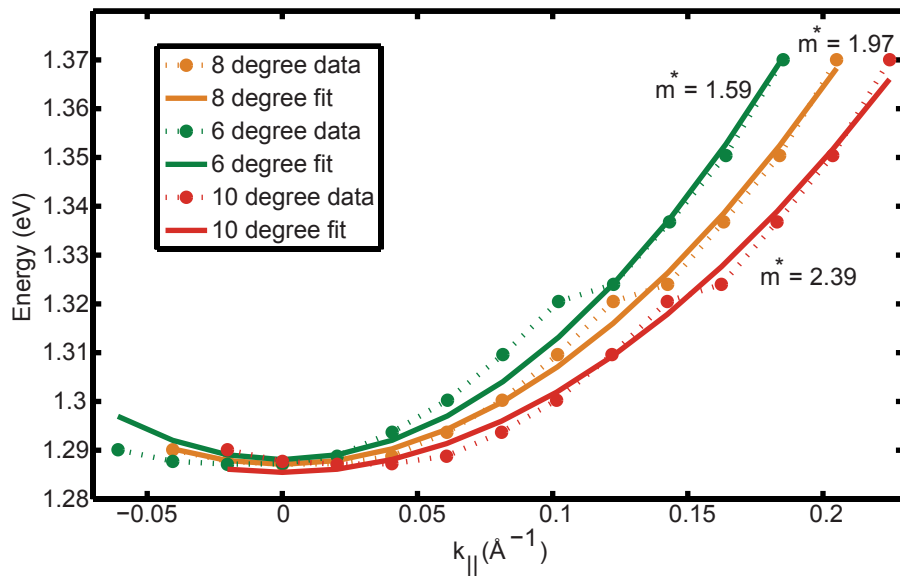


Figure 2.3: Determining crystal angle cut by TPPE.

approximately double for a $10K$ increase in temperature in the typical energy region of $300 - 700K$. In Knudsen cell dosing a molecular beam is produced with a flux equivalent to a backing pressure in the range of $10 \times 10^{-7} \text{ torr}$. The resulting film is somewhat different, however, as the molecules have typical sticking coefficients near unity, and they are generally less mobile on the surface as compared to small molecules with high vapor pressures.

A small side chamber houses the Knudsen cells used in these experiment. The side chamber is separated from the main chamber by a large gate valve, which serves to isolate the chamber from background vapor pressure due to a hot crucible. This also serves to isolate the main chamber under ultrahigh vacuum conditions while samples are changed in the side chamber, limiting time necessary for bakeout.

A single crucible effusion cell is used for most of the experiments discussed here. This effusion cell uses resistive heating of a ceramic crucible, controlled by a computerized Proportional-Integral-Derivative (PID) loop. A second, three crucible effusion cell was added. This effusion cell uses electron beam thermally emitted from a tungsten filament to heat molybdenum crucibles held at a variable positive voltage. Heating is caused by high energy electron bombardment of the crucible. This configuration is capable of reaching much higher temperatures than resistive heating (See Figure 2.4. Temperature gradients are maintained between each of the three effusion cells using a water-cooled copper jacket. Because this does not include a built in thermocouple, an ammeter is used to measure the vapor pressure of stray atoms and molecules ionized by the electron beam.

This configuration was initially designed for heating metal samples, and the manual provides specifications for dosing organic molecules as well. It was found that organic molecules do not dose repeatable with this configuration, however, and the electron emission filament will heat the sample crucible as high as $600K$ using the emission filament alone, without applying any voltage to the sample crucible. In order to surmount this problem while keeping the advantages of being able to dose multiple samples at high temperatures, a series of custom-machined Knudsen cells were manufactured. These Knudsen cells are switched in with drop-in capabilities. Crucibles are held

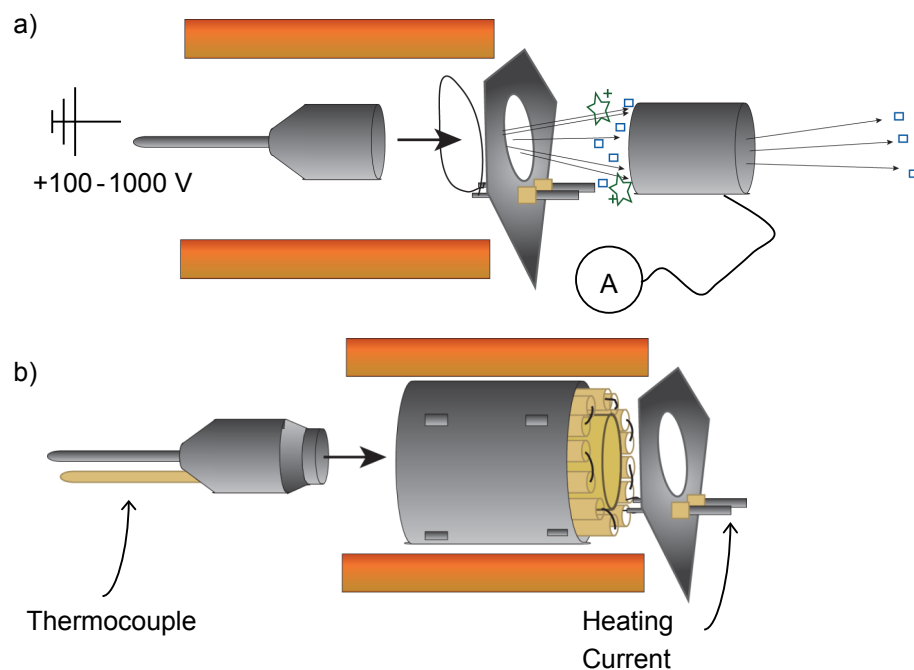


Figure 2.4: Multicrucible effusion cell with a) electron beam heated crucible and b) knudsen cell crucibles.

at a set temperature by a PID loop, and thermocouple monitoring shows a temperature stability better than $1K$. High temperature limitations of this setup are set by the crucible design, which is based on machined type 316L stainless steel. Stainless steel is only capable of temperatures up to 700 K , so temperatures at or above $700K$ will require either replacement with a Molybdenum crucible or switching that cell to the e-beam heating method. Because this is a drop-in setup for each of three crucibles, the triple effusion cell is capable of dosing using both metals and organics simultaneously using a combination of e-beam and PID heated cells.

Chapter 3

Charge Injection in the Electrochemical Double Layer of Room temperature Ionic Liquids

3.1 Introduction

Room temperature ionic liquids (RTILs) constitute a unique solvent class consisting of charge separated ion pairs, providing electrical conductivity without the need for solute ions. Steric hindrance by alkyl ligands and diffuse charge localization allow low temperature liquid behavior and a glass transition as low as 200 K[85, 90, 89]. These unique properties have resulted in increasing application of RTILs as "green" industrial solvents[20] and solvents for heterogeneous catalysis[57]. Electrochemical conductivity and stability have encouraged applications in Gratzel cells[84], and low vapor pressure may allow RTILs to be a safer solvent for automobile Li⁺ ion batteries[47, 55]. Numerous groups have studied the bulk solvation response of RTILs photoinjected free electrons or photoexcited dye molecules. These studies have generally found slow solvent re-sponse occurring inhomogeneously over timescales from ps to ns, while a subpicosecond component may contribute 10 – 50% of solvation[54, 15]. Slow response generally has been attributed to high viscosity and steric hindrance. Viscosity is proposed as a kinetic barrier to charge transport[90] and has prevented commercial implementation in batteries[90, 83]. A question remains whether the same mechanisms will dominate the solvent response at an electrode interface. Theoretical studies have, for example, found that 80% of the interfacial response to an applied voltage occurs on a homogeneous single exponential timescale as short as 200 fs[67]. Devices controlled primarily by interfacial response such as supercapacitors may be able to overcome kinetic barriers occurring in the bulk[88]. In supercapacitors, power is stored by a rearrangement of the first few molecular layers at the electrode interface, known as the electrochemical double layer. Fast response at the interface and a wide electrochemical stability window may allow high performance devices.

We present here the first experimental study, to our knowledge, examining charge solvation at the electrode interface. The low vapor pressure of these solvents allows studies to be performed in vacuum conditions on room temperature, liquid samples. Under ultrahigh vacuum conditions, molecularly thin films are grown from a molecular beam produced by a Knudsen cell. This allows direct investigation of the solvent-metal interface. Ultrathin films of RTILs are grown on the surface of a single crystal Ag(111) electrode. Dynamic solvation energy of an injected electron is examined as the RTIL electrochemical double layer reorganizes around the injected excess charge.

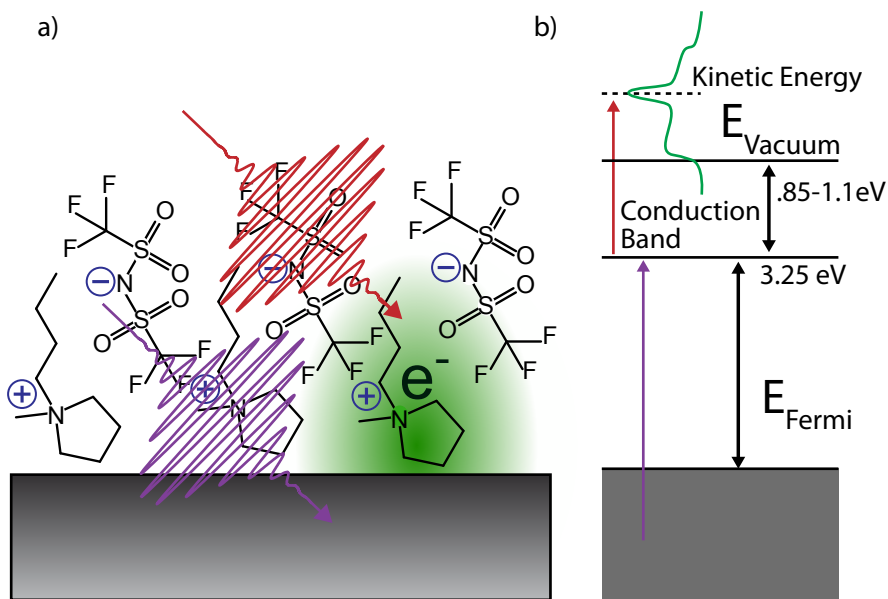


Figure 3.1: Schematic showing a) a molecular film of $[Bmpyr]^+[NTf_2]^- / Ag(111)$. In TPPE a UV pulse excites an electron from the substrate into the molecular film, and a visible pulse photoemits it to a detector. An energy diagram b) shows the conduction band located $3.25eV$ above the Fermi level.

3.2 Experimental

We present here an examination of electron solvation within RTIL adsorbed on a metal electrode. We utilize femtosecond time- and angle- resolved two photon photoemission spectroscopy (TPPE), (see Figure 1a-b). In this pump-probe spectroscopic technique, an ultraviolet pump pulse excites a charge transfer excitation from an occupied electronic state in a conductive substrate to an unoccupied state in an adsorbed film. After a variable delay time, a visible pulse photoemits an electron to a kinetic energy detector. With this technique, the energy of a transiently occupied state within the electrochemical double layer can be measured relative to the Fermi and vacuum levels with a typical energy resolution of 50 meV and time resolution of 100 fs. Liquid samples of anhydrous, 99% purity, were purchased from Sigma Aldrich. An atomically clean Ag(111) substrate was prepared by sputtering with $500eV Ar^+$ and annealing to 725 K. Samples are dosed via molecular beam from a Knudsen cell held at a temperature of 475 K onto a Ag(111) sample held at 300 K, following the method of Zaitsau et al[87]. In subsequent experiments, the sample temperature was controlled within $\pm 1K$ between 130 and 350 K using a liquid nitrogen cold finger and resistive heating.

TPPE investigations were carried out on $([Bmpyr]^+[NTf_2]^-)$. The cation, 1-Butyl-3-methylimidazolium $[Bmim]^+$ was also tested with two anions, bis(trifluoromethylsulfonyl)imide $[NTf_2]^-$ and hexafluorophosphate $[PF_6]^-$, though photoinduced sample degradation was found to occur within 5 minutes. The $[Bmpyr]^+[NTf_2]^-$ degraded more slowly, over 15 minutes or more. It is known that $[Bmim]^+$, $[NTf_2]^-$ and $[PF_6]^-$ ions are prone to chemical decomposition and photolysis[75]. Improved stability of $([Bmpyr]^+[NTf_2]^-)$ may be partly attributable to stability of its components. Stronger observed cation-metal binding of $[Bmpyr]^+$ [5, 31] versus $[Bmim]^+$ [17]

and subsequent exclusion of the anion from the metal may also limit catalytic photodegradation of the anion. In order to minimize sample degradation, all spectral acquisition times were kept shorter than 5 minutes, and the sample was moved with respect to the laser between spectra, in a raster pattern. Dynamic and temperature dependent spectra were taken in both forward and reverse directions and repeated on freshly prepared films to ensure reproducibility.

3.3 Results and Discussion

The two photon photoemission spectra are found to have a single peak resulting from a conduction band state (CB). In order to have accurate fitting of the peak intensity relative to a large background, and in order to accurately fit the high and low energy cutoffs, the full spectra are fit to a sum of contributions (Figure S1a). The CB peak is fit to a Voigt line shape. The background signal is fit to an exponential decay from the Fermi level. This has been previously shown to approximate the population of low energy scattering states in the sample. High and low energy cutoffs were treated as finite temperature Fermi-Dirac cutoffs. This is an accurate physical description for the high energy cutoff, which can be formally treated as a convolution of the initial density of states and the energetic width of the coherent two photon probe. At relatively low temperatures this is a good approximation for the low energy cutoff (vacuum level), within the Poisson counting error and time of flight detection linearity. This peak was fit to a Voigt lineshape with a typical FWHM of 400 meV. The background treated as scattered electrons with intensity decaying exponentially from the Fermi level. With increasing coverage, the peak was found to grow in monotonically with the disappearance of the image state and surface state of clean Ag(111). This is typical of layer by layer growth or the growth of a wetting layer followed by island-type growth. Increased degradation rates prevented examination of thicker films. We tentatively assign the coverage we investigate to a bilayer (cation plus anion) thickness with a similar growth mechanism to typical ionic salts. The bilayer assignment consistent with dynamic studies discussed below, though more detailed growth mechanism studies are necessary.

This fitting allows an accurate determination of the kinetic energy of the photoemitted electron. In order to measure the energy of the intermediate state relative to the vacuum and Fermi levels, the identity of the pump and probe pulses must be determined. A wavelength survey is performed in which the energy $h\nu_1$ is tuned. The second pulse, $h\nu_2$ is constrained to twice the energy of $h\nu_1$ by the frequency doubling setup. A slope of 1 in measured kinetic energy versus $h\nu_1$ corresponds to a $h\nu_1$ probe, while a slope of 2 corresponds to a $h\nu_2$ probe and $h\nu_1$ pump pulse. Similarly, a slope of zero results from a vacuum resonance and a slope of 3 results from photoemission from a bound state. In our experimental setup, the $h\nu_1$ and $h\nu_2$ are the tunable output of a visible optical parametric amplifier (1.75-2.58 eV) and the frequency double of that pulse. Varying the energy of the pump-probe pulse pair results a change in the photoemitted kinetic energy with a slope of one relative to the fundamental for a visible probe. The fit to the data in Figure S1b has a measured slope of 0.93 ± 0.3 , identifying this as a h 1 probe and h 2 state. Using the measured workfunction, the energy of CB is 3.25eV above the Fermi level.

A second determination of the identity of this peak is possible through a measurement of the sample workfunction. The workfunction is found to vary strongly as a function of temperature. The workfunction of the sample is measured as a function of the high and low energy cutoffs at temperatures in the range of 130 – 350K. Here, the Fermi level of the sample is held constant by a voltage bias between the sample and detector. Shifts in the workfunction are therefore observed solely through a shift in the vacuum level by a change in the surface dipole. In order to be able to observe the vacuum level cutoff, the detector is held at a constant positive bias of 0.5 – 1eV

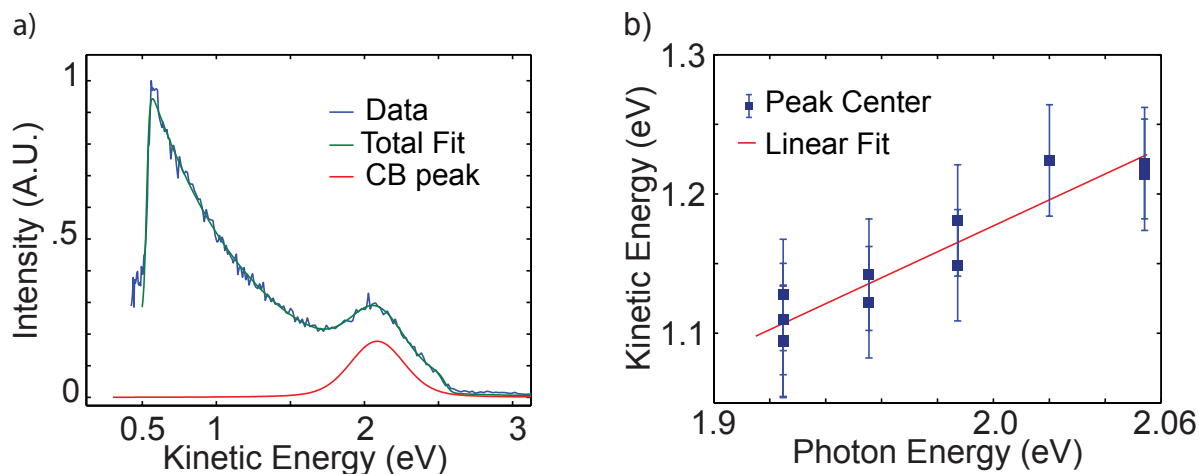


Figure 3.2: Schematic showing a) a molecular film of $([Bmpyr]^+[NTf_2]^-)$ on Ag(111). In TPPE a UV pulse excites an electron from the substrate into the molecular film, and a visible pulse photoemits it to a detector. An energy diagram b) shows the conduction band located 3.25 eV above the Fermi level.

relative to the sample. As shown in Figure WFscheme1, the sample vacuum level shift will be observed as a shift in the low energy cutoff. With an increase in the sample workfunction, the low energy cutoff shifts to higher energies. The energy of the CB peak is also monitored as a function of temperature. If this state were an IPS, it would be bound to the vacuum level, and it would shift with the vacuum level to first order. In the case shown here, however, the CB peak remains at a constant energy despite shifts in the vacuum level. We point out that the Fermi level, which is observed as the high energy cutoff at a kinetic energy of $h\nu_1 + h\nu_2$ minus the workfunction of the detector, will remain constant. Both the CB and high energy cutoff are found to remain at a constant energy despite vacuum level shifts, supporting our assignment as a conduction band.

The dynamic solvent response to the photoinjected electron is measured as a decrease in photoemitted kinetic energy as a function of delay time (Figure 2a). A wavelength survey identified this peak as an initially unoccupied intermediate state, see Supporting Information (SI). This state resides at an energy 3.25 eV above the Fermi level, as shown in figure 1b. This is assigned as a $[Bmpyr]^+[NTf_2]^-$ lowest unoccupied molecular orbital or conduction band state (CB) as will be discussed below. With increasing coverage, the CB was found to grow monotonically with the disappearance of the image state and surface state of clean Ag(111). This supports a layer-by-layer or wetting layer growth mode^[86], and agrees with observations of a wetting layer in previous studies of model RTIL by other vacuum techniques^[23]. Increased degradation rates prevented examination of thicker films. We tentatively assign the coverage we investigate to a bilayer (cation plus anion) thickness. Low energy electron diffraction observed residual diffraction spots from the Ag(111) substrate supporting our assignment of thickness ≈ 1 nm. A dosing rate of approximately 0.1 bilayers per minute is determined by the disappearance of the Ag(111) surface states and appearance of the CB. The energy of the CB is within the range that could be expected for $[Bmpyr]^+[NTf_2]^-$ based on cyclic voltammetry^[35, 7]. Cyclic voltammetry measures the charge injection barrier to form an anion in a conduction band state as the edge of the stability window. Here, we inject electrons with optical charge transfer excitation using a pump pulse near 4 eV.

Angle resolved measurements determine the CB localization or delocalization. Momentum is conserved upon photoemission, and the CB electronic momentum parallel to the Ag(111) sub-

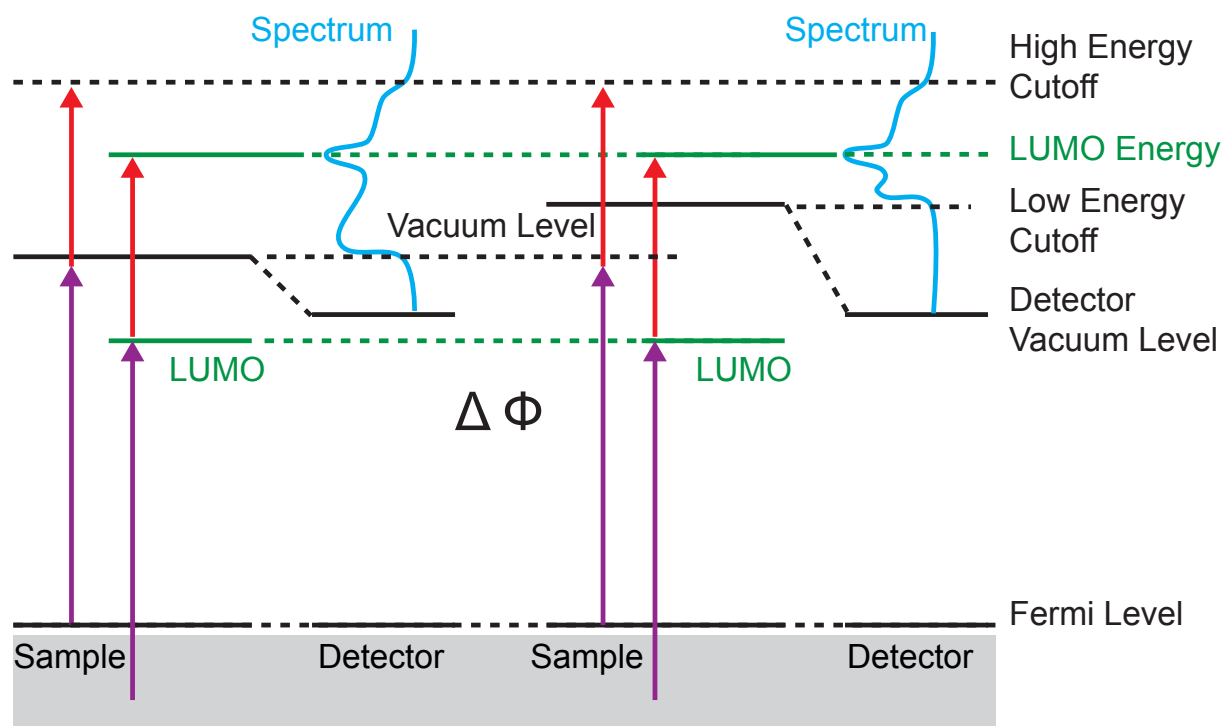


Figure 3.3: Schematic of workfunction shift observed by TPPE.

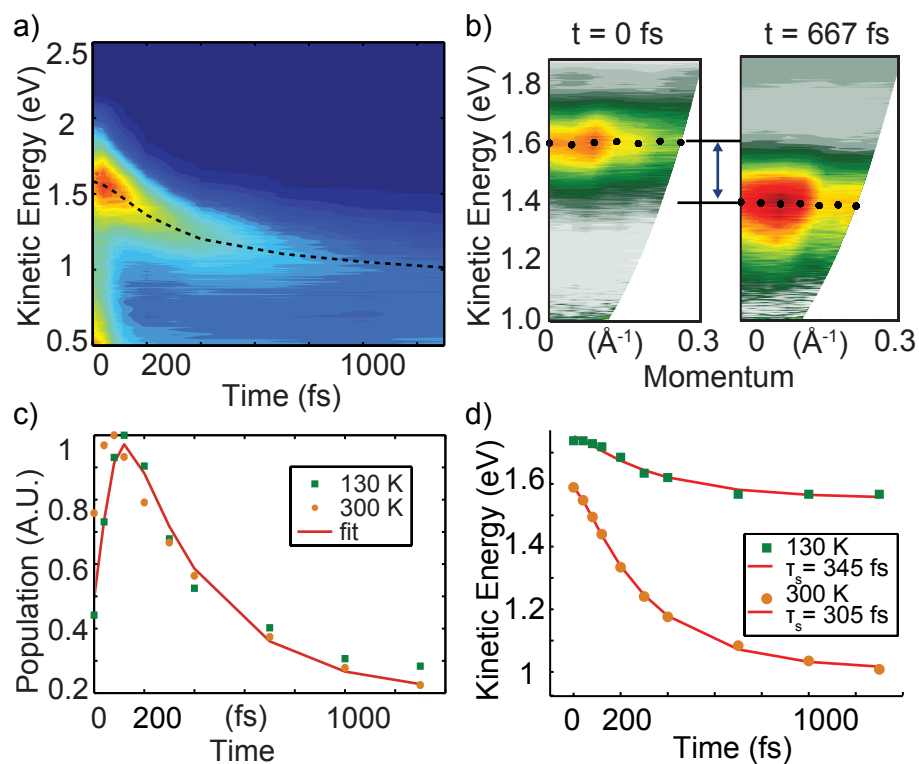


Figure 3.4: A conduction band peak solvates dynamically a). Angle resolved spectra b) reveal a localized state. The rates of decay to the metal c) and solvation d) remain constant at low and high temperatures, while the total energy of solvation d) is much greater at 300 K than 130 K.

strate can be measured as that of the photoemitted electron. A solid angle of momentum (k_{\parallel}) is detected by changing the substrate angle (Θ) relative to a detector, following the dispersion relation 3.1.

$$k_{\parallel} = \sqrt{\frac{2 \cdot m_e \cdot E_{\text{photoemitted}}}{\hbar^2}} \cdot \sin(\theta) \quad (3.1)$$

Here E_{kin} is the measured kinetic energy, and m_e^* is the band's effective mass relative to a free electron[80]. A large effective mass corresponds to a localized electronic state whereas an effective mass near unity corresponds to a nearly free electron. The CB has an initial band mass of $-15[+24, -11] m_e$ at zero time delay and 300 K (Figure 3b). At a time delay of 667 fs effective mass remains heavy, measured to be $-8[-5, -11]m_e$. A slight negative curvature is likely a systematic error in measurement, similar to that reported for electron solvation in ice[11]. Because we observe flat band dispersions at all times, we assign this state as localized to one or a few molecules.

The rate of electron solvation Figure refRTILangles fits to a single exponential with a typical time constant of 350 ± 150 fs. The CB energy shift measures the reorganizational response of the $[Bmpyr]^+[NTf_2]^-$ solvent due to the introduction of an excess charge. A trapping mechanism based upon diffusion to defect sites can be ruled out because the CB is localized at all times. Trapping by defect sites would also be expected to show separate peaks, rather than the continuous transition observed here. The time scale of this solvation also rules out purely electronic effects, as these would be expected to occur on a ~ 50 fs timescale. The observed 350 fs timescale is consistent with inertial response of the solvent or reorganization over a few librational periods. We also point out that the single exponential decay distinguishes this from bulk solvation mechanisms, which are typically stretched exponential. This response is consistent with predictions for interfacial solvent response being dominated by a single femtosecond reorganizational timescale[67] The work function shifts strongly as a function of temperature (Figure 3a). As the temperature increases, the work function decreases by $245 \pm 80 meV$. This appears as a shift in the vacuum level, while the Fermi level (determined by the high energy cutoff) remains constant. At 300 K, the CB is $3.25eV$ above the Fermi level and $0.85eV$ below the vacuum level, which could allow assignment either as a conduction band or an image state. The energy of an image state is bound to the vacuum level and will directly follow the vacuum level. The CB is found, however, to have constant energy with respect to the Fermi level, consistent with assignment as a conduction band. The change in work function ($\Delta\Phi$) can be attributed to a change in the surface dipole as a result of reorienting molecular dipoles (P), by equation 3.2,

$$\Delta\Phi = \frac{e}{\epsilon_0} \cdot P \cdot \frac{\Theta}{d^2} \quad (3.2)$$

where ϵ_0 is the vacuum permittivity, P is the molecular dipole, and Θ is the number of molecules per d^2 area of a molecule[26]. For $[Bmpyr]^+[NTf_2]^-$, the charge separated anion cation pairs constitute the molecular dipole. Using the measured work function change, and molecular unit cell 8AA on a side[14], we estimate the change in surface-normal projection of the intermolecular dipole to be $0.40 \pm .15 Debye$. Decrease in work function is likely due anion motion, as the cations bind strongly to the metal at the exclusion of the anions[5, 31, 45]. For an intermolecular dipole of 3 Debye[39], and charge separation of 5AA, this would result from a dipolar rotation of 10-30 and corresponding translation of the anion 1AA toward the vacuum interface.

We propose here that the solvated electron is localized to the cation, a topic which has recently been debated[52]. While the work function measures a significant temperature dependent motion of the anion, the CB lifetime remains constant within error of the measurement. The lifetime of photoinjected electrons is known to depend exponentially on the distance to the metal

substrate. Temperature independent lifetimes are consistent with localization on a cation which remains bound to the metal interface. Similar molecular rearrangements have been observed in both temperature and voltage dependent studies RTIL interfaces. A voltage-dependent change in x-ray reflectivity was observed in $[Bmppy]^+[NTf_2]^- / Au$.²⁷ This study found the Au interface remained cation rich at all voltages, while the vacuum interface was anion rich at positive voltages and mixed character at negative voltages. Orientation transitions have been observed in imidazolium ionic liquids as both a function of temperature^[41] and voltage,^[6] though both the cation and anion are found at the metal interface for imidazolium ionic liquids. This molecular reorientation can be treated as a temperature dependent phase transition of a two phase material at equilibrium. Spectroscopic investigations of equilibrium phase transitions have been shown to follow Boltzmann sigmoid^[37, 53, 19]. This results from modeling a spectroscopic observable ($\Delta\Phi$) of the partition function for a two state molecular system, 3.3:

$$\Phi(T) = \frac{\Phi_A}{1 + \exp(T - T_0/D)} + \frac{\Phi_B}{1 + \exp(T - T_0/D)} \quad (3.3)$$

Here T is the sample temperature, T_0 is the transition temperature. The variable D defines the width of the transition and is a measure of the enthalpy of the order-disorder transition and the size of molecular clusters. In this investigation, Φ_A and Φ_B are the work functions of the low temperature and high temperature phases and $\Phi(T)$ is measured work function of the sample. The work function shifts continuously due to phase coexistence. Clusters of each phase, which each have local work function of Φ_A or Φ_B , both exist within the transition region and contribute to the global work function. The work function in Figure 2A, is fit to a Boltzmann sigmoidal, with a transition temperature of $T_0 = 253 \pm 16K$ and a broadening, $D = 13 \pm 6K$.

The total change in energy upon solvation varies strongly as a function of temperature. The CB solvates by $530 \pm 40meV$ in the high temperature limit, while it solvates by only 200 meV at cold temperatures. Total energy of solvation versus sample temperature is fit to Eq. 2 with $T_0 = 242 \pm 10K$ and $D = 25 \pm 10K$ (Figure 3d). The T_0 measured by electron solvation magnitude matches that of the temperature dependent work function within error bars, which are reported as 95% confidence interval^[2]. The phase transitions observed by change in work function and energy of solvation can be assigned to the same mechanism.

3.4 Conclusions

The magnitude of solvation is sensitive to the molecular reorientation in these two phases. For comparison, solvation of an electron by small polaron formation was observed in thin films of ionic NaCl. The depth of the solvation in NaCl was observed to be 85 meV. Small polarons are energetically unfavored in bulk, and their presence is attributed to greater deformability of an NaCl thin film relative to bulk^[62]. The solvation we observe is 2-7 times as strong, likely due to increased mobility and deformability of the ionic liquids relative to inorganic salts. The difference in solvation energy between the low and high temperature phases may be due to this deformability. Mobility dependent solvation was observed in single monolayer versus bilayer dimethyl-sulfoxide (DMSO) on Ag(111)^[80]. Here strong substrate binding in single monolayer DMSO limits solvation, while the molecular dipole in the second monolayer is free to rotate, allowing a 220meV dynamic solvation. In the $[Bmppy]^+[NTf_2]^-$ data we present here, solvation magnitude may be due to deformability above and below an order-disorder transition.

We have observed charge injection and dynamic electron solvation at the interface of a $[Bmppy]^+[NTf_2]^-$ thin film and Ag(111) electrode. This study has quantified a previously

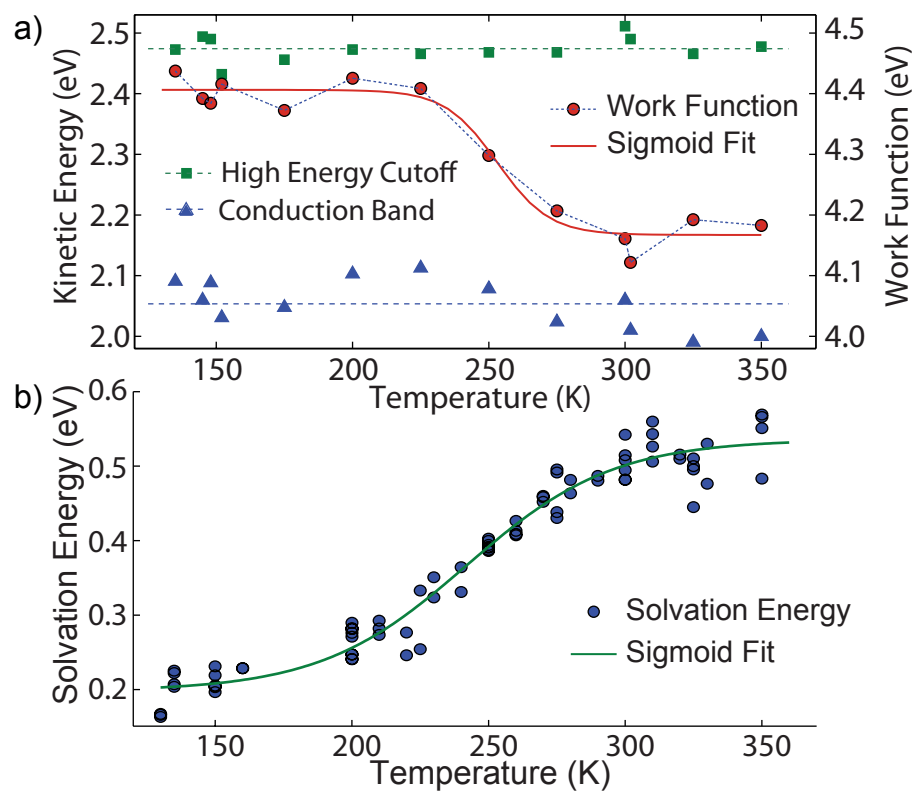


Figure 3.5: a) The work function shows a temperature dependent phase transition. The energy of the CB and high energy cutoff are constant with temperature. b) The transition between phases is also observed by the reorganizational energy of solvation

suggested interfacial phase transition. Angle and time resolved measurement support electron localization on the cation. A single temperature dependent phase transition is responsible for both a change in work function and a change in reorganizational energy associated with dynamic solvation of a localized CB state. Solvent response in the high and low temperature limits result from a reorientation of the anion at the vacuum interface. These results support previously proposed femtosecond reorganizational kinetics as the primary solvent response at the interface. We expect these results to be general and applicable towards an understanding of the molecular mechanisms governing supercapacitors and other electrochemical devices.

Chapter 4

Image State Band Folding in Phthalocyanines

4.1 Introduction

Much of the behavior in electronic devices and heterogeneous catalysts is defined by the energy level alignment, band structure, and spatial extent of electrons at the interface between two materials[48, 36, 38]. Much experimental success has been made recently in controlling and confining occupied surface state electrons using single atomic defects, quantum corrals and periodic nanoporous lattices on metal surfaces[18, 50]. Nanometer unit cell sizes approaching the Fermi wavelength allows direct modification of surface states with these scattering barriers.

Scattering models have had much success describing these surface modifications[44, 82]. Although atomistic and *ab initio* descriptions would be ideal, nanometer unit cells at a surface are prohibitively large to calculate, and DFT approaches do not properly treat unoccupied states[71, 16]. Instead, scattering models are computationally inexpensive and can be fit to with empirically derived model potentials[38]. Further, the analogy between a corral or porous lattice and scattering barriers makes such descriptions physically intuitive.

4.2 Experimental

In this work, we probe unoccupied electronic band structure in molecular thin films with photoemission spectroscopy, and we demonstrate that our results can be understood through similar scattering models. In a molecular film, the potential energy surfaces presented by different functional groups act as the quantum wells and scattering barriers experienced by an injected electron. Molecular semiconductors consist mainly of delocalized π - and π^* -orbitals interrupted by localized and directional σ -orbitals at the molecule edges, of which the latter acts as our scattering lattice. Building off the potential energy surfaces introduced by Kronig and Penney[43], we introduce a 2D model pseudopotential that is able to predict band folding, symmetry, and spatial extent of unoccupied surface electrons using only the symmetry and spatial extent of functional groups within the unit cell. These results compare well with our experimental observations. Our results highlight the importance of intermolecular coupling and symmetry in controlling band properties.

We report photoemission experiments of an injected electron in a crystalline monolayer film of metal-phthalocyanine (MPc). MPc's have been shown to achieve high efficiencies in molecular electronic devices[63], and as a result are increasingly studied as model molecules. Copper- and iron- phthalocyanines (CuPc and FePc), depicted in Figure 1A, were epitaxially grown on

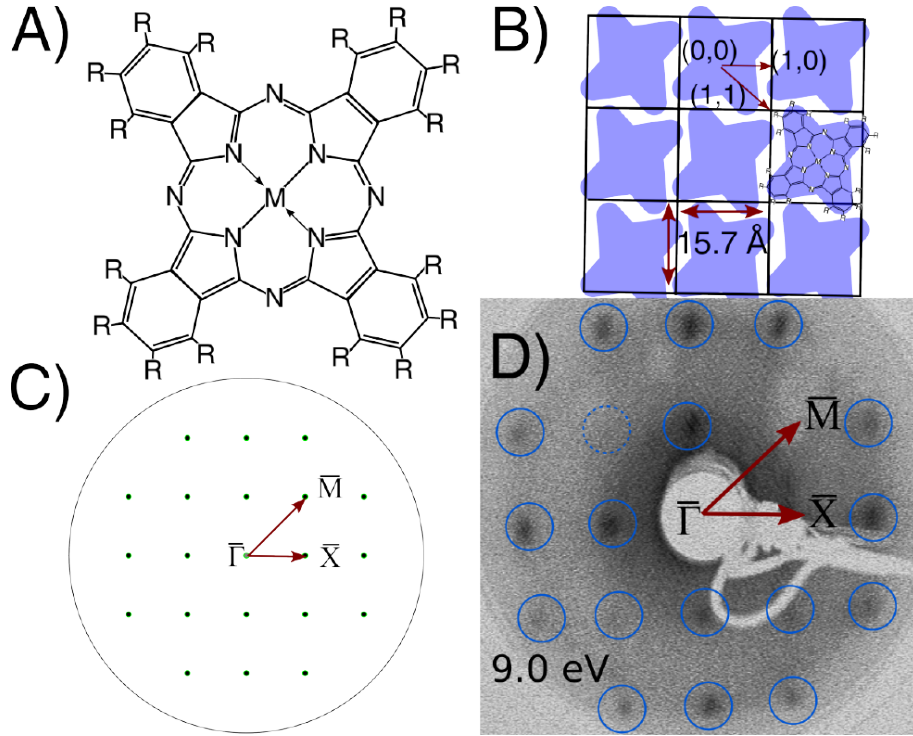


Figure 4.1: A): Phthalocyanine structure. $M = \text{Fe}$ or Cu ; $R = \text{H}$. B): Schematic of phthalocyanine lattice showing high symmetry directions. C) Predicted LEED for FePc/Ag(111). D) Experimental LEED for FePc/Ag(111).

an atomically smooth surface of Ag(111), prepared by (Ar^+) sputtering and annealing. Ordered layers were grown epitaxially on a Ag substrate held at 300K [81, 28]. In agreement with previous literature reports, a highly ordered and uniform single molecular layer formed after annealing a multilayer film up to 580K for 30 minutes followed by cooling to a base temperature of 130K [51]. This annealing process removed any evidence of second or higher monolayer coverages.

Low Energy Electron Diffraction (LEED) shows that both CuPc and FePc grow epitaxially in a square lattice, with a single molecule per unit cell and a repeat distance comparable to the literature value of 15 – 16 Å, (Figure 4.1) [42, 77, 65]. CuPc and FePc differ slightly in packing as a result of the symmetry of the substrate. Epitaxial growth on the six-fold symmetric Ag(111) substrate causes the CuPc to pack into 12 different domains rotated by 30° with respect to one another as shown in Figure 4.3. The FePc, however, packs as a single square lattice, while the other rotated domains are unobserved. The presence of only a single oriented domain in FePc may result from residual step edges growing laterally on the Ag(111) substrate [40, 65].

Angle- and time-resolved two photon photoemission spectroscopy (TPPE) is used to investigate the unoccupied electronic states in each system. In this technique, a femtosecond pump pulse excites an electron from below the Fermi level of the metal and into a previously unoccupied state. After a waiting time, a second, probe pulse photoemits the electron into a time-of-flight energy detector.

Angle dependent measurements resolve the electronic momentum, picking out solid angles of acceptance by rotating the sample with respect to a detector behind a slit, in a manner similar to one-photon angle resolve photoemission spectroscopy (ARPES). The angle, θ , and momentum parallel to the surface, $k_{||}$, of the photoemitted electron are related by the measured energy

$E_{\text{photoemitted}}$ and the mass, m_e , of an electron:

$$k_{\parallel} = \sqrt{\frac{2 \cdot m_e \cdot E_{\text{photoemitted}}}{\hbar^2}} \cdot \sin(\theta) \quad (4.1)$$

The energy versus momentum dispersion relation characterizes the band structure and coupling in a material.

Momentum dependent intensities have been previously shown to be related to the square modulus of the initial and final states, (Ψ_i and Ψ_f), coupled by the electromagnetic vector potential and electron momentum operators[9, 61]:

$$I \propto |\langle \Psi_i(x, y) | \hat{A} \cdot \hat{p}_z | \Psi_f(x, y) \rangle|^2 \quad (4.2)$$

The photoemitted intensity, I , measured at different angles, thus relates directly to the initial state k-space wavefunction by a simple transformation. ARPES experiments have observed k-space intensity fluctuations resulting from fourier transformed real space molecular orbitals[69]. Similarly, angle-resolved TPPE experiments have related gaussian intensity distributions to localized, trapped electronic wavefunctions[58].

4.3 Results

Here, an image potential state (IPS) electron probes potential energy corrugation in the MPc adlayer. Briefly, an IPS occurs when an electron ejected outside a metal surface induces a reorganization of charge inside the metal. On clean, high symmetry noble metal surfaces, a Rydberg series of bound states form, which remain delocalized parallel to the surface[21]. The $n=1$ IPS resides within the first few Å outside a bare metal or metal with an adlayer of attractive electron affinity. The IPS electron is thus an ideal probe of the first few adsorbed monolayers.

Three IPS are seen for monolayer coverages of both FePc/Ag(111) and CuPc/Ag(111). IPS binding energies are measured at -0.85eV , -0.55eV and -0.14eV in FePc, and at -0.90eV , -0.60eV and -0.19eV in CuPc, relative to the vacuum level (Figure 4.6A). The workfunctions, measured to be 4.15 ± 0.1 eV by the high and low energy photoemission cutoffs and the onset of one photon photoemission, places the observed energy levels in FePc and CuPc within instrumental error of one another. These states do not fit to the typical image state Rydberg progression. Further, the binding energy of the lowest state is below that of clean Ag(111), suggesting IPS mixing with one or more of the phthalocyanine LUMO of attractive electron affinity. The presence of multiple low lying LUMO states supports such a hybridization but prevent assignment to mixing with a single orbital[92]. Lifetimes, measured to be 30 ± 15 fs in all three peaks, determined with a pump-probe cross correlation of 100 fs, are also consistent with a LUMO hybridization. We introduce the progression of states here as $j = (1, 1)$, $j = (2, 1)$, and $j = (3, 1), (1, 3)$ backfolded bands of the $n=1$ IPS, as will be discussed below.

Phthalocyanine thin films were grown using molecular beam epitaxy from a knudsen cell held at 640 K. Layered For this experiment it was necessary to be able to identify the crystal structure of the phthalocyanine substrate. At low coverages, phthalocyanines have often been observed to behave as self-avoiding 2d gases. Under these conditions, the phthalocyanines are mobile and statistically distributed across the surface. We were able to avoid this by only examining complete monolayers, formed by annealing and desorbing multilayer coverages. Coverage determination was initially performed using TPPE, where new monolayers can be observed with the growth and disappearance of shifted IPS with the growth of each monolayer. Multilayers were grown at a rate of approximately $0.2 \text{ ML}/\text{min}$. The first and second monolayers each had clearly defined peaks

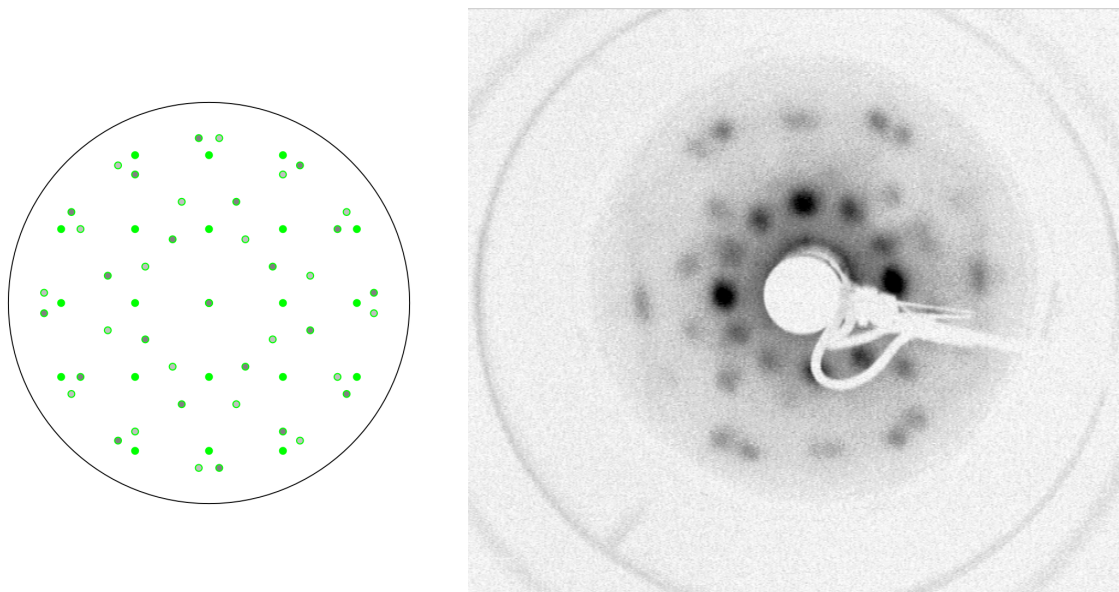


Figure 4.2: Left: Simulated LEED spectrum for CuPc/Ag(111) produced by LEEDSIM simulation program. Rotated domains are visible as different shades of green dots. Right: Experimental LEED spectrum obtained for CuPc/Ag(111)

associated with them, while thicker coverages appeared as a broadening of the IPS of the second monolayer. Upon annealing, a TPPE spectrum similar to first monolayer was obtained, while the IPS peaks were slightly sharper and shifted to slightly greater binding energies as compared to the unannealed monolayer, consistent with an increase in ordering.

To determine the morphology of our CuPc/Ag(111) and FePc/Ag(111) surfaces, we examined LEED spectroscopic images and modeled our system using the program LEEDSIM. In these LEED simulations, a Ag(111) monolayer substrate was defined using known unit cell parameters. The adlayer was modeled as a square unit cell matching the 14-16 Angstrom unit cell that others have observed via STM. The symmetry of the hexagonal substrate and square adlayer allow for 12 different rotations, of which 3 are symmetry unique. These will appear in the crystal structure as local domains of different rotations, and with a finite spot size it appears in the LEED structure as 3 overlaid sets of spots. LEEDSIM was used to directly output the spots of rotated domains (Figure 4.2). This matched the LEED pattern seen for CuPc. The FePc/Ag(111) only shows one domain, which can be predicted by disallowing rotations. It is also observed directly in the CuPc/Ag(111) predicted LEED spectrum as the bright green set of spots.

It is surprising that the FePc grew in only one of the possible domain rotations. The CuPc, in comparison, grew all three domains. We point out however, that the CuPc monolayer was observed to have different intensities for the three domains. The intensities of these domain spots were also not necessarily repeatable from day to day, suggesting that the CuPc may have also been susceptible to domain preference. The main difference between the CuPc and FePc crystal structures is that the FePc grows in a commensurate growth mode, while the CuPc grows in a point-on-line growth mode (Figure 4.3). This is a direct result of a stronger binding of the FePc to the Ag(111) substrate as compared to the CuPc. The point-on-line crystal structure requires a doubling of the unit cell length in one direction in order to preserve the rectangular symmetry of the CuPc molecules. The commensurate growth in FePc, however, involves only one molecule

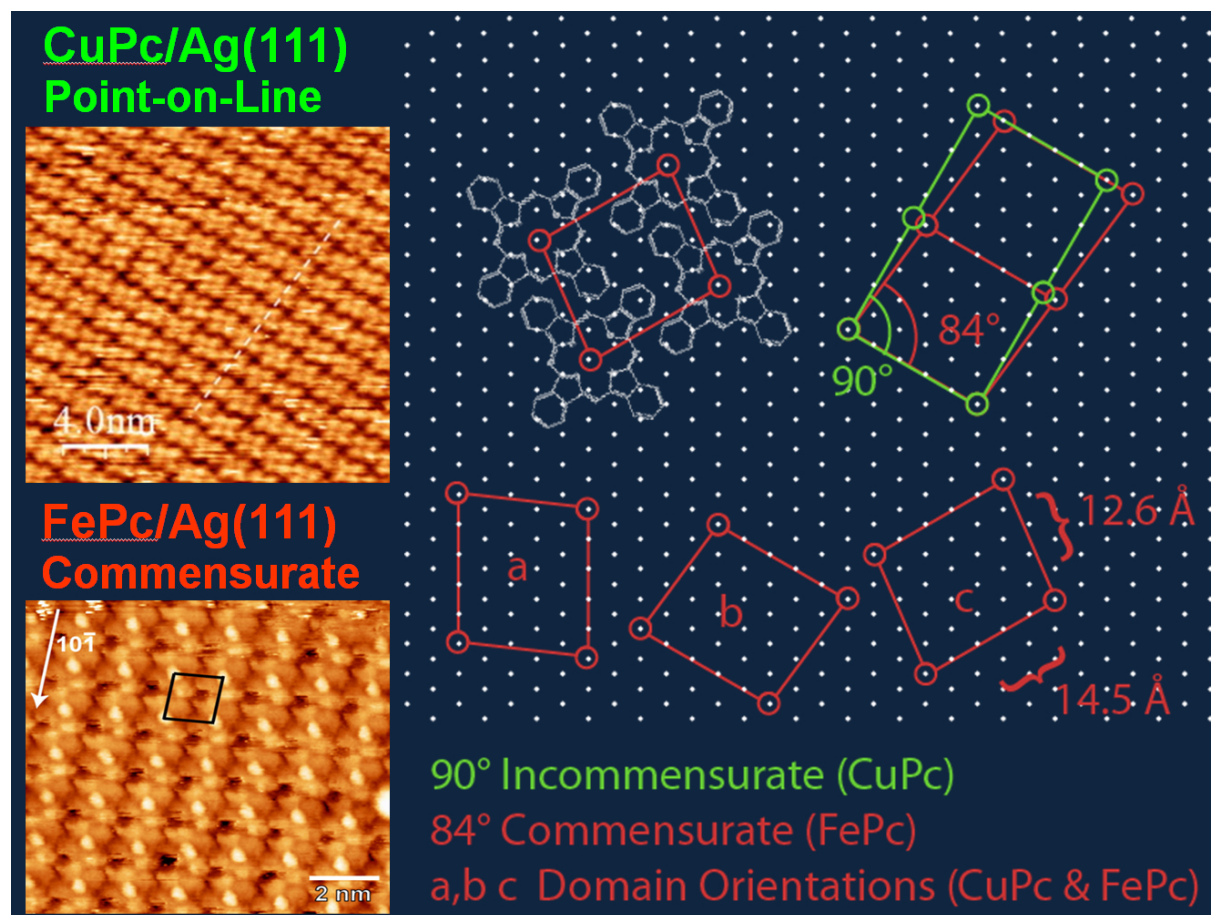


Figure 4.3: Commensurate and Point-On-Line growth of FePc and CuPc.

per unit cell in order to ensure that each molecule sits in a preferential orientation relative to the Ag lattice. This comes at the energetic expense of about an 8° distortion of the phthalocyanine unit cell angle. The stronger binding to the Ag(111) substrate will make the FePc more sensitive to remaining oriented terraces on the Ag(111) substrate. Templating by these terraces creates a preferential growth of a single domain rotation.

Spectroscopic investigations were performed using 2 color TPPE. In our setup, the UV pump pulse is produced by frequency doubling the visible probe pulse, and thus is constrained to be twice the energy. Identification of pump versus probe pulse is determined using a wavelength survey, as shown in Figure 4.4. A slope of 0, 1 or 2 in photon energy versus photoemitted electron energy corresponds to an above vacuum level resonance, visible probe, or UV probe. Wavelength surveys for the $j=(1,1)$ and $j=(2,1)$ were measured across a range of over 200 meV, resulting in fits to a slope of 1.0, consistent with the assignment as hybridized image states. The slope of the highest energy peak corresponding to the $j=(3,1)$ and $j=(1,3)$ states was limited by the vacuum level cutoff, and the minimum energy required to pump the pulse. Wavelength surveys for this peak were thus limited to a range of 100 meV, and thus represent the largest error in slope determination (see Supporting Figure 2). The wavelength survey for FePc/Ag(111) slopes are fit to: $j=(1,1), 1.290.44$; $j=(2,1), 1.350.16$; $j=(1,3)/(3,1), 1.280.43$. The wavelength survey for CuPc/Ag(111) slopes are $j=(1,1), 1.050.05$; $j=(2,1), 1.240.5$; $j=(1,3)/(3,1), 1.000.13$. Reported error bars represent 95% confidence interval calculated by a linear regression. These slopes confirm a UV-pump pulse and visible

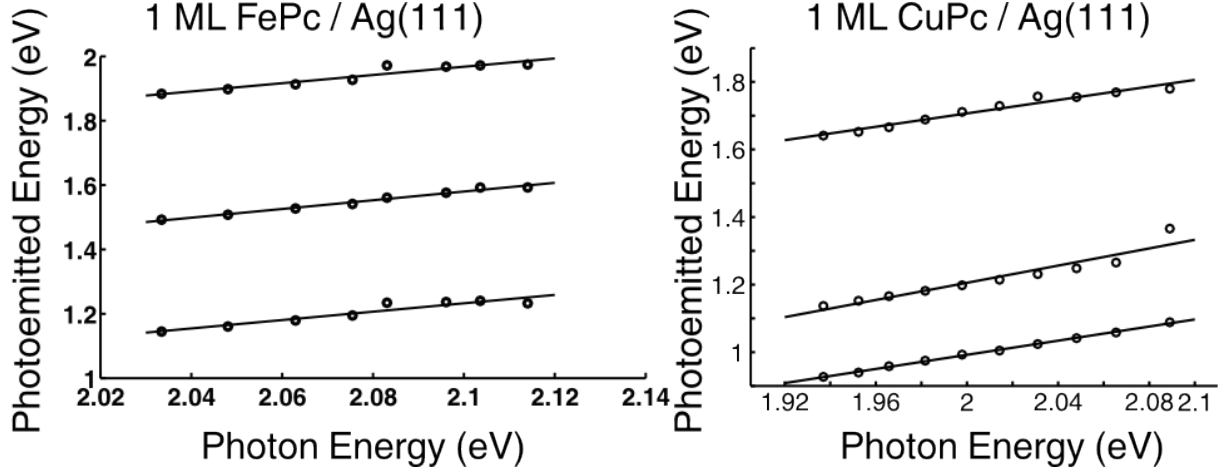


Figure 4.4: Wavelength surveys for FePc (left) and CuPc (right)

probe pulse and support the assignment of these peaks being in the energy region expected for image state peaks.

Angle dependent measurements were performed by rotating the angle of the crystal with respect to the detector, using horizontally (p) polarised light. Electrons were detected in a time of flight detector behind a rectangular slit with an acceptance angle of 1.5 in the direction of crystal rotation and 4 in the direction perpendicular. The resulting momentum acceptance of 0.05 \AA^{-1} for photoemission normal to the surface limits the ability to identify peak amplitudes and energies at the $\bar{\Gamma}$ point. Individual electron counts were stored in energy bins. The counts were first scaled to account for the angle dependent probability of photoemission and then scaled to convert from a constant angular acceptance to a constant momentum space area of acceptance. Figures 3 and 4 in the text show this type of graph plotted as scaled counts versus energy and momentum. Each background subtracted spectra was fit using MATLAB. Peaks are treated as variable width Voigt functions, and the baseline was fit to an exponential representing background scattering. The high energy cutoff was then treated as a fixed temperature Fermi-Dirac distribution. The addition of a Fermi-Dirac fit to the high energy cutoff allowed much more accurate fitting of the peaks as the $j=(3,1)$ peak moved above the high energy cutoff at intermediate angles (Figure 4.5).

The dispersion of FePc was probed along the $\bar{\Gamma}-\bar{X}$ direction as determined by LEED, while the CuPc dispersion was averaged across different directions resulting from the additional rotated lattice domains. These three image states have both positive and negative effective masses, measured to be 1.5, -2.0 and $1.1 m_e$ for the $j=(1,1)$, $(2,1)$ and $(3,1)$, $(1,3)$ states in FePc. While the small effective masses imply delocalization, the negative effective mass of the $j = (2,1)$ is unusual for a free-electron-like image state, implying significant interaction with the MPc lattice. Further, the $j = (1,1)$ and $j = (2,1)$ states have energetic minima and maxima at $0.21 \pm 0.03 \text{\AA}^{-1}$, which corresponds well to Brillouin zone folding with the periodicity of the MPc.

Lastly, sharp variation in photoemission intensity as a function of parallel momentum is observed. The $j = (1,1)$ and $j = (3,1), (1,3)$ bands have maximum intensity near the $\bar{\Gamma}$ point, while $j = (2,1)$ has a maximum intensity at the \bar{X} point of the adlayer, (Figures 3A and 3B). Momentum dependent intensities thus distinguish these hybridized IPS from free electrons, yet do not match molecular orbital descriptions, and new modeling is merited.

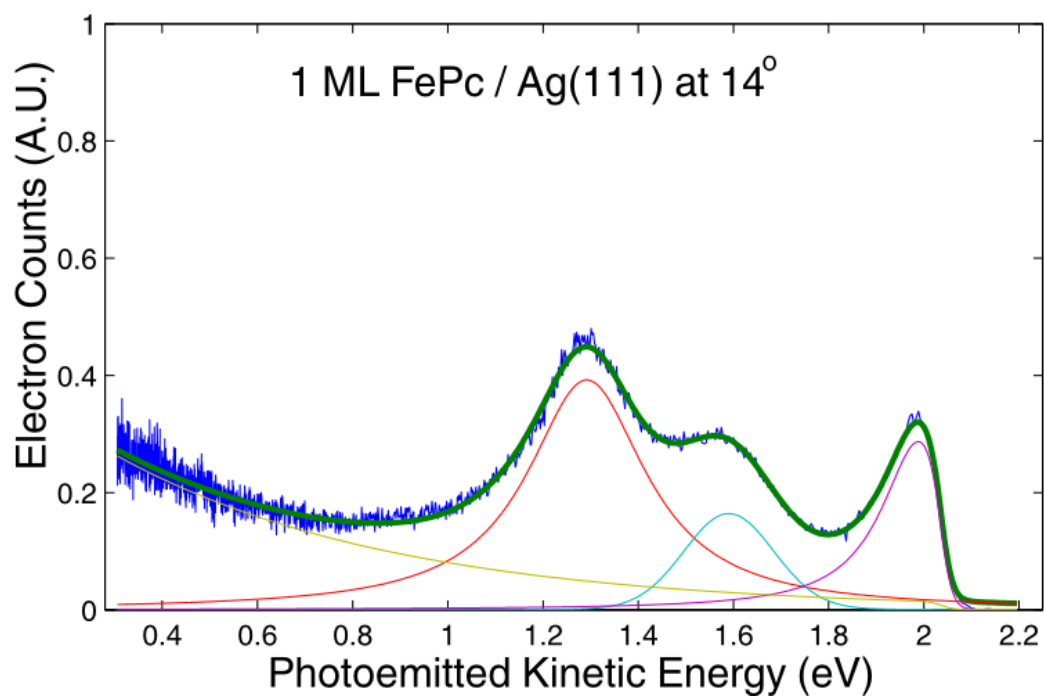


Figure 4.5: Fit to a spectra of 1 ML FePc/Ag(111) taken at 14° . This angle is given as an example to show the $j=(1,1)$ (red) peak and $j=(2,1)$ (cyan) peak at similar intensities, while the $j=(3,1)$ / $(1,3)$ peak (purple) moves above the high energy cutoff. The scattering background was fit to an exponential (yellow). The total fit is shown in green, against the original, unsmoothed data shown in blue.

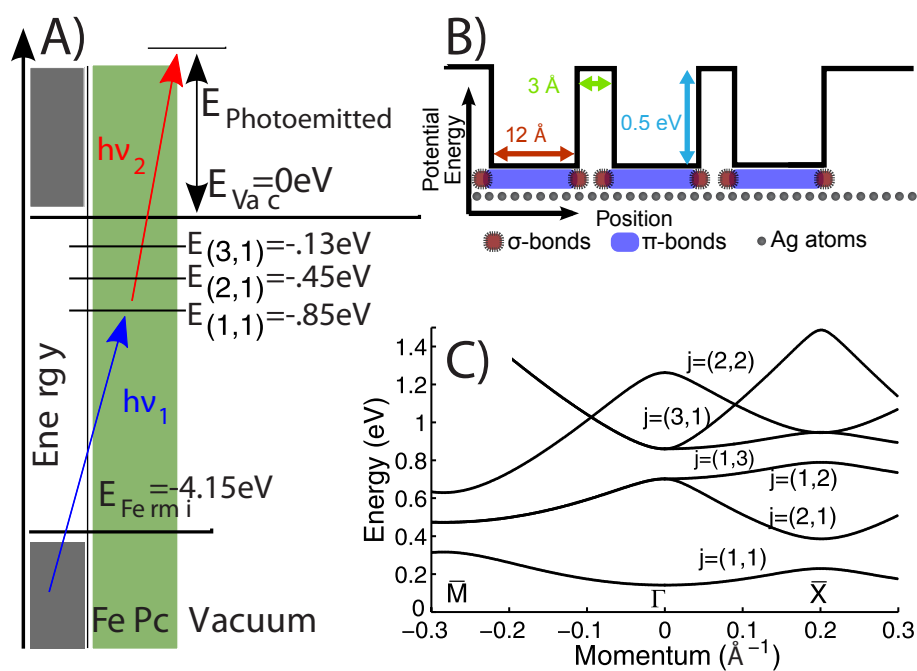


Figure 4.6: Schematic of TPPE. A pump pulse excites an electron from the Ag (light blue) into the FePc adlayer (light green) before photoemission. Energies are referenced to the vacuum level. B): Cut through of the modeled potential energy surface showing a series of quantum wells parallel to the surface. C): Band structure of the lowest several states, calculated along high symmetry directions.

4.4 Coupled Quantum Well Model

We model these results beginning with the square well potential originally discussed by Kronig and Penney[43]. A similar 1D model has successfully described photoemission intensity scattering on stepped metal surfaces[64]. Here, however, our potential energy corrugation results from the image electron coupling with different functional groups across the surface. The image electron couples with the aromatic core of the MPc, which acts as a smooth, attractive potential within the center of each molecule. This delocalized core, however extends only 12 – 13 Å across the 15 – 16 Å unit cell. The remaining 3 Å at the unit cell edges contains C-H bonds. Unlike the aromatic, π^* core, σ -orbitals along the C-H bonds are both directional and localized. Further, the lowest unoccupied (σ^*) orbitals residing on the C – H bonds are much higher in energy than the π^* LUMO orbitals. Interaction with the repulsive σ^* orbitals can thus be approximated by a higher effective potential energy surface in this region.

Considering these two components in constructing a pseudopotential, the σ^* orbitals act as a scattering barrier at the edge of the MPc, modeled as a potential step. The barrier height and width are the only adjustable parameters of the model, the latter of which was set to the approximate width of the C-H bonds. The barrier height was empirically set to 0.5 eV to obtain a best fit of energies near the $\bar{\Gamma}$ point. This energetic height is intermediate between the smaller, 0.1-0.25 eV, barriers that have been used to model the occupied surface state confined in nanoporous superlattices and the larger potential energy that could be expected from an unscreened interaction with the σ^* orbital[79]. This intermediate empirical value is consistent with qualitative expectations for an image electron, which has more electron density within the layer than a surface state electron, while still having electron density in both the metal and vacuum.

Separation of variables allows the scattering parallel to the surface to be treated independently from binding normal to the surface. The Matlab code for this is included in Appendix A. This simple Kronig-Penney model thus only explicitly treats the 2D potential parallel to the surface and assumes a bound state normal to the surface. Energies are obtained by finding the determinates of the Schrödinger equation:

$$(V_{\bar{x}} + V_{\bar{y}} - E)(\psi_{\bar{x},\bar{y}}) = \frac{\hbar^2}{2m_e} \nabla_{\bar{x}}^2 \nabla_{\bar{y}}^2 (\psi_{\bar{x},\bar{y}}) \quad (4.3)$$

Here m_e , is the mass of the electron, and $\psi_{\bar{x},\bar{y}} = (\psi_{\bar{x}}^0 \psi_{\bar{y}}^0 e^{i(\vec{k}_{x,y} \cdot \vec{r}_{x,y})})$ are the Bloch planewave solutions. Solutions are calculated using the finite difference method and periodic boundary conditions[56]. Eigenvalue energies, E, versus wave vector, $\vec{k}_{x,y}$, yield band dispersions. Each band, resulting from Brillouin zone folding, can be labeled in convention with the 2D quantum level nomenclature, where the quantum numbers, $j = (m, n)$, indicate the band folding in the k_x and k_y directions[46]. Band dispersions of the lowest energy states, $j = (1, 1)$ through $j = (3, 1)$ and $(1, 3)$, are plotted in figure 2C along the $\bar{\Gamma} - \bar{X}$ and $\bar{\Gamma} - \bar{M}$ directions. The former corresponds to the experimentally probed direction in FePc, while $\bar{\Gamma} - \bar{M}$ represents a rotation of 45° to the corner of the Brillouin zone.

Finally, the k-space probability density is calculated in order to recreate the intensity distribution. Bloch wavefunctions are first calculated as real space eigenvectors of equation 3. Fourier transforming and multiplication by the complex conjugate results in a normalized 2-dimensional probability density in k-space. Band energy and intensity are then calculated along the $\bar{\Gamma} - \bar{X}$ direction to match the probed orientation in FePc.

The resulting predicted spectrum measures electron probability density as a function of energy and momentum (Figure 3C). Lifetime and inhomogeneous broadening in energy are represented as a 250 meV Voigt line-width. It is immediately apparent that fewer bands are observed

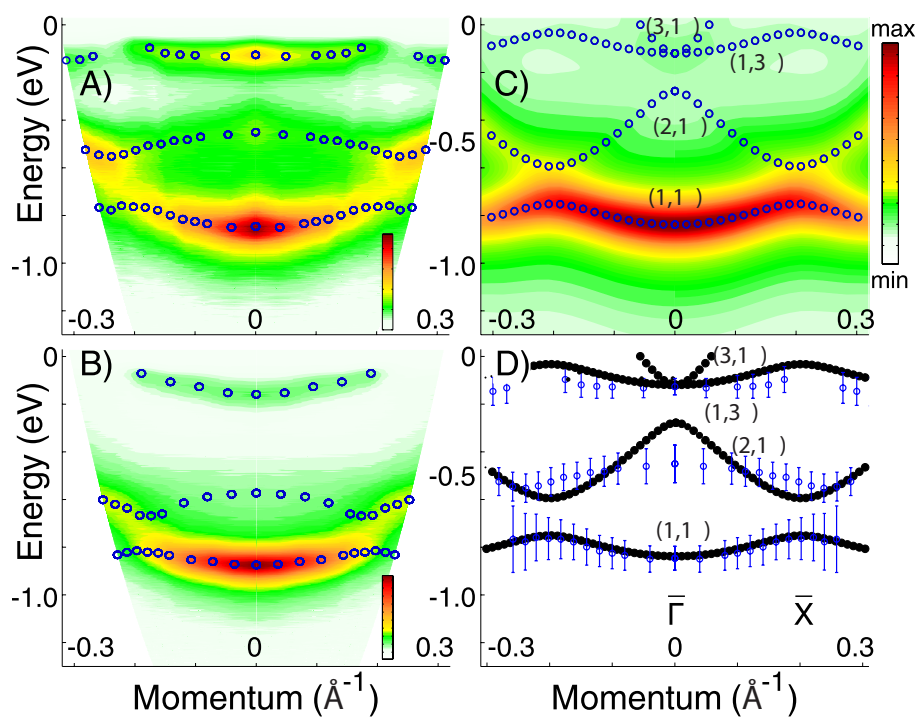


Figure 4.7: Experimental band structure and photoemission intensity for FePc (A), CuPc (B), and predicted photoemission for FePc (C). Peak centers shown with blue circles. (D) Comparison between predicted observable band structure (black) and experimental peak fits (blue) with error bars 1/4 FWHM of the fit.

here than exist in the full band structure (Figure 2C). Only the $j = (1, 1)$, $(2, 1)$, $(1, 3)$ and $(3, 1)$ quantum levels contribute significant intensity to the observed spectrum, while the $j = (1, 2)$ and $(2, 2)$ states have minimal intensity along the directions and momenta probed.

4.5 Discussion

Comparison between the modeled results and experimental spectra (Figure 3A-C) shows strong agreement. Three peaks are clearly visible in each spectra, arising from the $j = (1, 1)$, $(2, 1)$, $j = (1, 3)$ and $(3, 1)$ states. Intensities are observed as the square of the wavefunction probability density. Experimental intensities of the are strikingly similar to the 2D square well predictions, given the simplicity of the model. The $j = (1, 1)$ and $(1, 3)$ and $(3, 1)$ states, predicted to be *gerade* by the symmetry of the square well, are observed as *gerade* states with maximum intensity near the $\bar{\Gamma}$ point. The $j = (2, 1)$ state is predicted to be *ungerade* with one node at the $\bar{\Gamma}$ point, and experimentally has a single minimum at $\bar{\Gamma}$. The intensity does not fully reach zero at $\bar{\Gamma}$, which may be caused by finite angle resolution and broadening.

Finally, it is interesting to note that the relative intensities of observed bands relative to one another approximately match the intensities predicted by the normalized wavefunctions. In order for the final state photoemission intensities to match normalized predictions in the model, there must be near uniform occupancy of the backfolded band, and therefore similar excitation probabilities[60, 22]. The transition dipole for excitation from, and decay to the metal are both proportional to the extent of the wavefunction into the metal, and excitation and decay can be treated similarly [92]. Previous experiments on IPS suggest that coupling to the metal is relatively uniform within a single band[34]. Here, where we have treated bandfolding of the $n=1$ IPS parallel to the surface, we expect uniform penetration into the bulk. Uniform transition dipole moments are thus expected, and this is supported by the smiliarly short decay times measured in each of the three peaks.

The $n=2$ IPS, which is not observed above the background in our experiment, is expected to have a smaller transition dipole. The $n=2$ IPS extends futher into the vacuum and has less bulk penetration at a noble metal surface. This commonly results in longer $n=2$ lifetimes and peak intensities that may be smaller by two orders of magnitude[70, 74]. Although the lower intensity of the $n=2$ state is common to many systems, it is expected to be particularly true when both the $n=1$ and $n=2$ states are within the surface bandgap, as they are here due to the vacuum level shift and lowered workfunction.

Experimentally observed band dispersions for FePc are plotted in figure 3D against modeled predictions. States with predicted low intensity are omitted. The curvatures of the $j = (1, 1)$ and $j = (3, 1)$, $(1, 3)$ states fit the model to well within experimental results. The $j = (2, 1)$ state, however, has a bandwidth notably less than that of the model. Finite angular resolution at the detector contributes to the band narrowing. Band narrowing may also occur from finite temperature electron-phonon coupling, or potential energy corrugation unaccounted for in the course grained model[30].

Anisotropic dispersions distinguish between the FePc and CuPc films. While FePc is probed only along $\bar{\Gamma}-\bar{X}$, the CuPc dispersion is integrated over each rotated lattice domain. Summing calculations over angles rotated in 30° increments from $\bar{\Gamma}-\bar{X}$ mirrors the experimental integration over rotated domains. Modeling shows that the $j = (1, 1)$ state is nearly isotropic within the probed region, and is similar between FePc and CuPc. The $j = (2, 1)$ state varies greatly in bandwidth as a function of detection angle. The observed $j = (2, 1)$ curvatures in FePc and CuPc are similar, however, because the $\bar{\Gamma}-\bar{X}$ direction, probed in both systems, contains greater intensity

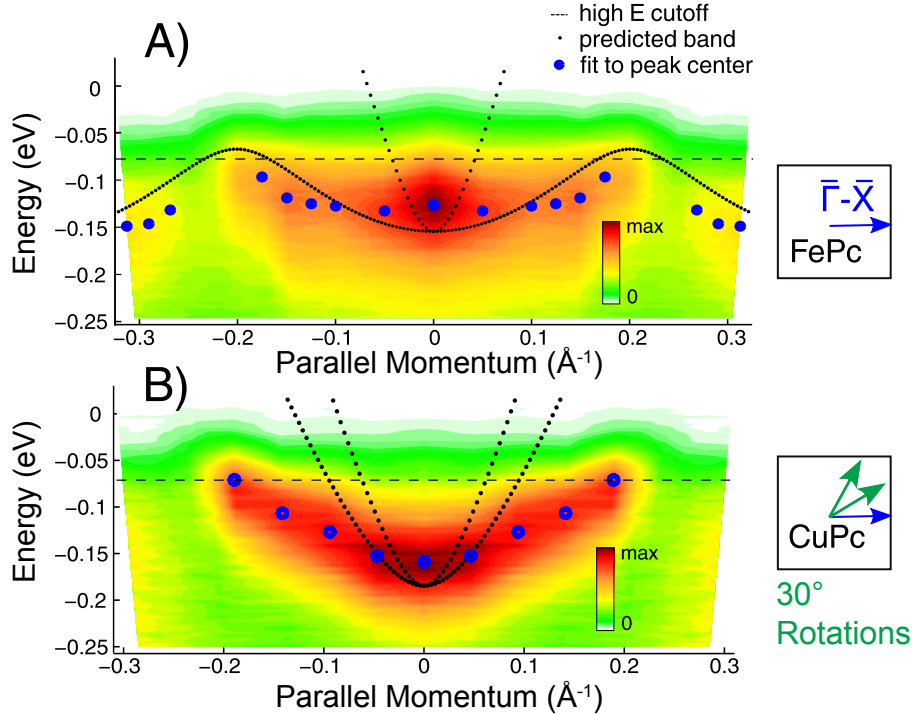


Figure 4.8: Anisotropy results in different dispersions and for the $j=(1,3)$ and $(3,1)$ bands as seen experimentally in FePc (A), and CuPc (B). Modeling predicts the $j = (1, 3)$ band to return below the HEC in FePc at high momenta (black dots), while it rises monotonically above the HEC in CuPc.

than the other rotated domains probed only in CuPc. As a result, the band curvature differs little, while the intensity of the $j = (2, 1)$ state is decreased in intensity relative to $j = (1, 1)$ in CuPc.

The $j = (1, 3)$ state shows more striking anisotropy. Along the $\bar{\Gamma}-\bar{X}$ direction of FePc, this state briefly rises above the high energy cutoff (HEC) becoming unobservable at intermediate momenta, before curving back below the HEC at large momenta (Figure 4A). In CuPc, however, dispersions along the rotated domains rise monotonically above the HEC (Figure 4C). Rotated domains thus cause the $j = (1, 3)$ intensity to decrease by a factor of 3 at high momenta in CuPc, and peaks are not observable above background noise. Anisotropic dispersions are thus able to distinguish between multiple and single crystal orientations using only a single detection axis.

4.6 Conclusion

Our results demonstrate a simple way of predicting band curvature, photoemission intensity and anisotropy in molecular thin films. Much of the electronic structure can be understood solely in terms of the symmetry and the locations of σ and π -bonds within the unit cell.

The results discussed here contrast other work studying surface electronic states and molecular semiconductors. Much work in this field focuses on the energy levels of molecularly derived orbitals, referenced to the isolated molecule. Similarly, band width is often treated as simply a measure of the strength of intermolecular coupling, ignoring symmetry and spatial extent. Our work, on the other hand, suggests that symmetry and lattice size may in some cases play a dominant role in the observed electronic structure, controlling and tuning the anisotropic band

splitting, quantum confinement, and wavefunctions.

We have developed here a simple and chemically intuitive picture of scattering and its effects on band structure in molecular crystals. While this type of lattice confinement is not expected to be observed for molecules or lattices <1 nm across, this type of band folding likely plays a role in defining the physical properties of a whole range of larger molecular and polymeric semiconductors, which are gaining ever more prominence in new devices.

Finally, these results directly examine a parameter for tuning charge carrier properties via lattice dimensions and the symmetry and extent of σ -bond scattering centers. Bands resulting from this type of scattering process will have altered mobility parallel to the surface, as well as charge injection and coupling across the interface. Further, the localization and symmetry of charge density will affect surface chemical bonding and orientation, both of which are important parameters in understanding catalytic processes.

Chapter 5

Phase Changes in Submonolayer Phthalocyanines

5.1 Introduction

Morphology of adsorbed layers is known to strongly affect reactivity and catalytic performance, and the morphology of the first monolayer is known to direct the packing of subsequent layers. Morphology and crystal structure of the first few layers in an epitaxially grown device directly controls intermolecular electronic coupling and electronic coupling to the substrate or electrodes.

The balance between mobile adatoms, which act like a 2D-gas or liquid and a condensed island phase has been a subject of interest to an understanding of thermodynamics for nearly 80 years[32, 33]. Several experimental techniques have been developed that measure phase transitions of adsorbed noble gas atoms or small molecules. For example, the equilibrium between a backing pressure of He gas and crystalline islands of He on a surface has been investigated for over half a century. Auger spectroscopy and work function measurements have been used to investigate equilibrium phase transitions in coverages approaching a monolayer. Helium scattering experiments have also been used to identify equilibrium phase transitions between 2D-island and a dilute 2D-gas of adsorbed Xenon. More recently, investigations of adsorbed metal atoms have found a complex interplay of both short and long range attractive forces with long range repulsive forces define the ensemble behavior[12].

These forces are more poorly understood and likely as complex in large organic molecules adsorbed on metal surfaces. During epitaxial growth, several different morphologies are possible with a given molecule and substrate. Several different crystal structures may occur for the same molecule, and these may be very different with relatively small changes in the molecular and substrate identities. Different phases will often grow depending upon relatively small changes in the sample temperature or dosing rate. Phase transitions of these adsorbates remain poorly understood because ensemble phase transitions do not directly provide information on the molecular and intermolecular forces driving them. Two dimensional phase transitions have provided a wide array of new physics in statistical modeling, but they are often more difficult to characterize experimentally. This experimental difficulty derives from a simultaneous need for molecular resolution, measurement of large scale ordered and disordered ensemble behavior, and often a need to characterize fast processes. Scanning tunneling microscopy, for example, has atomic resolution but is limited in size of scan range and in rate of measurement[8]. Diffraction techniques can observe large scale and ensemble phenomena but are less sensitive to disordered phases and cannot measure the important

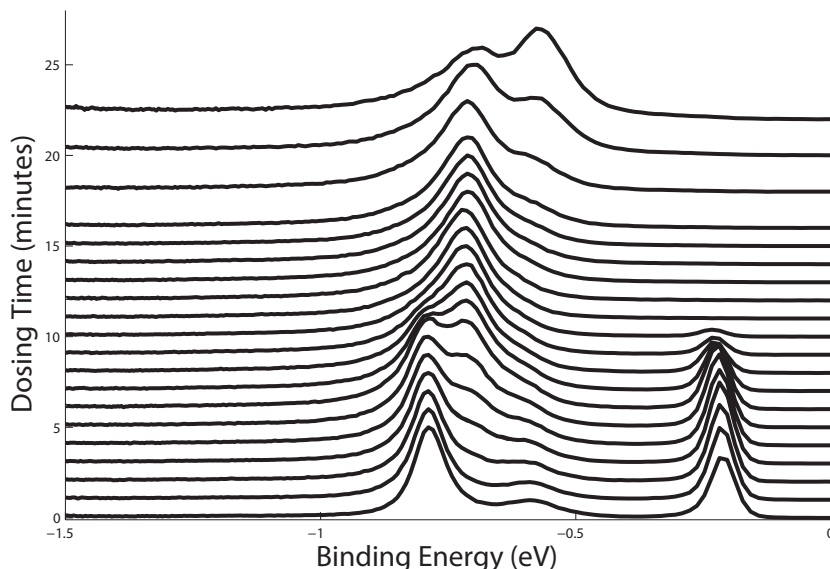


Figure 5.1: Dosing survey of Copper Phthalocyanine a) and Titanyl Phthalocyanine b).

changes in electronic properties.

TPPE has been previously shown to be sensitive to the crystalline phase of a material. In the chapter on room temperature ionic liquids, for example, a conduction band is found to be sensitive to an order-disorder transition occurring as a function of temperature. As discussed by Marks, et al, the image state (IPS) is sensitive to a temperature dependent structural phase transition in perfluoropentacene[53]. In this study, the image state intensity is found to be dependent upon the crystal structure, which is found to change as a function of temperature.

TPPE has been previously shown to different growth modes (layer-by-layer, island and wetting layer). In Figure 5.1, we show the results of a dosing survey on 3,4,9,10-perylene tetracarboxylic dianhydride (PTCDA). PTCDA is dosed on a Ag(111) single crystal held a 300 K using a dosing rate near 0.1 ML / min. In this figure, several TPPE spectra are stacked above one another, offset by a value proportional to the amount of material dosed, measured in minutes. Under these growth conditions, PTCDA is known to form a fairly crystalline layer-by layer coverage. As the first monolayer is dosed, the $n = 1$ IPS of clean Ag(111) is replaced by the $n = 1$ IPS existing within the PTCDA film. This image state has a different energy than that of the clean Ag(111) because it is bound to the local, well defined vacuum layer of the PTCDA. The image state also is further shifted slightly to lower energies due to the attractive electron affinity of the PTCDA layer, and it will experience a small confinement energy due to quantum confinement perpendicular to the interface.

As this film is grown, the submonolayer PTCDA forms large islands. These islands are large enough to have a local workfunction identical to the workfunction of the complete monolayer. The $n = 1$ IPS therefore has a well defined energy that does not change as a function of coverage. Because the intensity of the IPS is proportional to the number of allowed states and therefore to the relative areas of bare Ag(111) and PTCDA, the IPS of the 1 ML coverage is observed to replace that of the clean Ag(111). In the growth of the second monolayer, this trend is expected to continue, and the $n = 1$ IPS grows in at a new energy, defined by the workfunction, confinement, and electron affinity it experiences in the 2 ML coverage.

Several studies have found recently that large organic molecules may be mobile on the

surface at or below room temperature. These studies have also found that a single large organic molecule can exist in two or more phases in coverages less than a monolayer. These include a diffusive phase at low coverages, which behaves like a 2-dimensional gas. At higher coverages, the molecule may be found in one or more crystalline phase, where the molecules have aggregated in a well defined lattice.

The mechanism of molecular aggregation through attraction or avoidance is a topic of general debate. Recent studies have observed for example, a submonolayer coverage of 1,4,5,8-naphthalin-tetracarboxylicacid-dianhydride (NTCDA) showed an inverse melting transformation, disordering upon cooling, which was attributed to a temperature dependent bonding strength to the metal substrate[76, 72]. Subphthalocyanine, which has a similar open pi-bonding structure, orders upon cooling, which has been attributed to an oscillating attractive potential[8], a repulsive intermolecular potential [24, 66], and coverage dependent coupling to the substrate[27].

Here, we present a study of submonolayer coverage of copper and titania metallated phthalocyanines (CuPc and TiOPc), which have been shown to behave as a diffuse 2D gas near room temperature and coverages less than 0.9 ML[Berner2001, Yasufuyu2001]. Studies have found that cooling a submonolayer coverage of SnPc below 120 K results in island formation, which was modeled by a temperature dependent repulsive interaction[76].

5.2 Experimental

Metallated phthalocyanines are purchased with typical 95% purity, and purified by vacuum sublimation. During vacuum sublimation, a white powder is found to evolve from the phthalocyanines at a temperature near 500K. Following purification by vacuum sublimation under a roughing pump, the samples are loaded into Knudsen cell in a side vacuum chamber capable of pressures less than 1×10^{-8} torr, where the sublimation is repeated up to a temperature of 550K for 2 – 3 days during a bakeout.

MPc samples are dosed on a single crystal Ag(111) substrate at a rate of 0.01-0.2 ML/minute. The temperature of the sample is controlled in the range 120 – 350K using a liquid nitrogen cold finger and computer controlled resistive heating. In cases where a crystalline layer is formed, the 2-dimensional crystal structure is determined by low energy electron diffraction (LEED) spectroscopy. The LEED performs best with crystal structures in the range of a few AA, and it is capable of measuring capable of resolving crystal structures with repeat lattice as large as 2nm. LEED is, unfortunately, unable to resolve the ring associated with the radial distribution due to limitations in the instrumentation.

5.3 TPPE Results

The TPPE spectra of CuPc, FePc, and TiOPc were examined as a function of coverage. The workfunction of each material was determined by the high and low energy cutoffs of the spectrum as well as the onset of one-photon photoemission. In each sample, the workfunction was found to decrease monotonically from 4.55 to $4.2 \pm eV$ during the growth of the first monolayer. The initial work function is that of clean Ag(111). The final work function is nearly equivalent to that which could be predicted from a vacuum level alignment of the molecule with the Ag substrate. The ionization potential of most metallated phthalocyanines with out electron accepting or donating ligands is 5.2eV. The band gap of these materials is 2eV for CuPc and FePc, and slightly lower for TiOPc. This results in an expected workfunction of approximately 4.2eV based on vacuum level

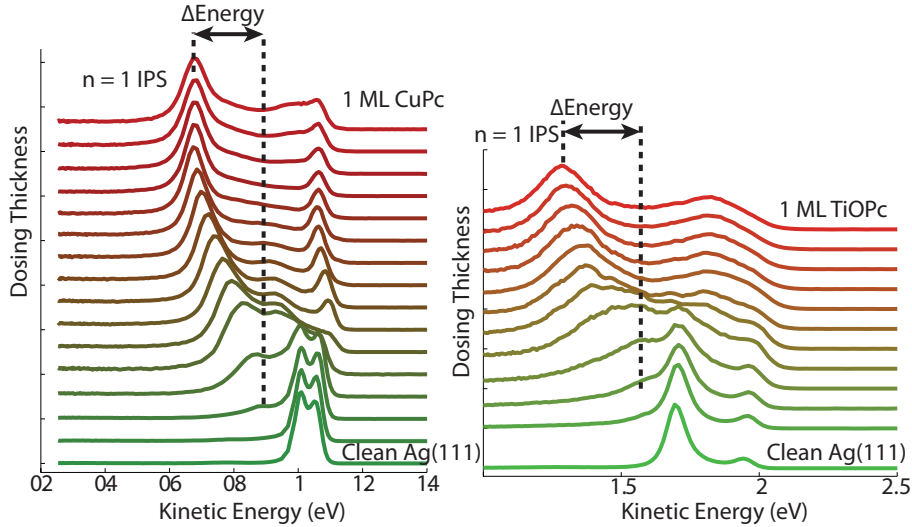


Figure 5.2: Dosing survey of Copper Phthalocyanine a) and Titanyl Phthalocyanine b).

alignment alone. Because the workfunction matches that of the vacuum level alignment, we can rule out strong electron transfer to or from the substrate.

The image state was found to follow the workfunction of the sample during this dosing survey. The image state is found to have an energy 0.9eV below the vacuum level at 1 ML coverage. At the lowest coverages where the image state of phthalocyanines can be measured, the IPS has an energy $0.1 - 0.15\text{eV}$ below the clean Ag(IPS). This is equivalent to having an energy 0.9eV below a local workfunction that has not shifted significantly from the 4.55eV work function of clean Ag(111).

This observation is qualitatively similar to observations by one- and two-photon photoemission (UVPES and TPPES) in films of TiOPc or VOPc / pyrolytic graphite (HOPG)[10, 78, 24]. These groups and others have attributed the vacuum level alignment and continuous work function shift of the phthalocyanines to a 2D-gas type growth mechanism. In this growth mechanism, phthalocyanine molecules remain far apart during growth. It has been shown that they are mobile on the surface, and the intermolecular distance is attributed to a repulsive mechanism. The large intermolecular spacing of isolated molecules results in a local work function that is intermediate between that of the clean Ag(111) and the phthalocyanine monolayer, with a work function shift proportional to the density of molecules.

Our measurement differs slightly from these measurements. In the TPPE measurements, the IPS shift was found to be approximately double that of the work function shift. Further, in UVPES, the HOMO and LUMO were found to shift slightly as a function of coverage. These observations, which were linked to complex mechanisms including molecular polarizability, are not observed in our study. The general trend is the same, however, with the molecular density acting as a measure of local density of molecules.

The image state of clean Ag(111) can be estimated to have an area of 750nm^2 , based upon the electronic scattering time of bulk Ag. Similarly, the image state of a full monolayer is found to be delocalized, with an effective mass near that of a free electron. The intermediate coverage is also found to have a free-electron-like dispersion. If we assume the electron is sensitive to an area equal over which it is delocalized, then the local work function experienced by the image state is

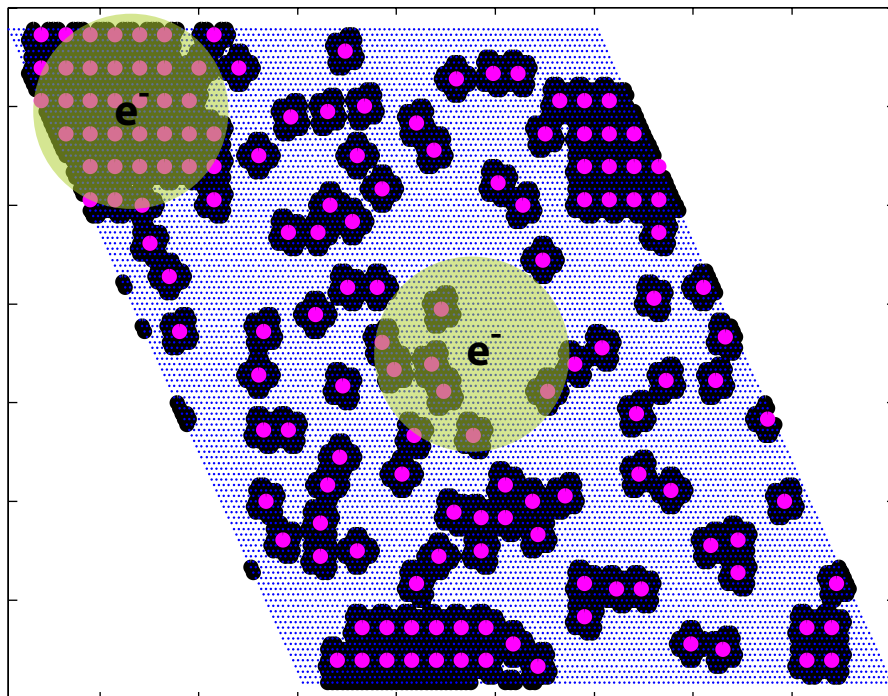


Figure 5.3: Image state probe of local work function of gas and island phase phthalocyanines.

near that occupied by 35 phthalocyanine molecules in the full monolayer.

Three phases of phthalocyanines have been observed by the Umbach group, using LEED spectroscopy[76]. The Umbach group used an advanced LEED spectrometer to observe the electron diffraction spectrum of Tin Phthalocyanines on Ag(111) as a function of coverage. Dosing surveys were performed at several substrate temperatures using *in situ* LEED spectroscopy. Using this technique, three crystal structures were observed. The first structure, occurring at high temperatures and low coverages, is a 2D gas growth mode, as observed by the ring of the radial distribution. The other two phases are two slightly different unit cells, both approximately square with sides of $1.5nm$ and 1 phthalocyanine per unit cell. The 2D gas phase at low coverages and high temperatures was attributed to an overall repulsive energy between molecules. The cluster formation at low temperatures was attributed to a second energetic interaction, in which, under conditions where the molecules have lower translational energy, they are able to find an ideal position with lower energy, allowing cluster formation.

The temperature dependence of these two peaks was also investigated at a constant coverage near $0.3ML$. At this coverage, the image state of the clean Ag(111) is no longer observed. The image state of the 2D-gas coverage is shifted to lower kinetic energies by about $100meV$. At this coverage, it is still approximately $200meV$ higher in energy than the image state of the crystalline monolayer.

Upon cooling to $120K$ over the course of 3 hours, the image state energy shifts to that of the full monolayer. This suggests the formation of islands with the density of the full monolayer and a size large enough that the local work function as seen by the image state is equivalent to the full monolayer.

This reversibility of this crystallization can be examined by heating the crystal. Figure 5.4 shows the TPPE spectra as a function of temperature upon heating. In this figure, phase coexistence of the clusters and 2D-gas can be observed by the presence of two separate peaks.

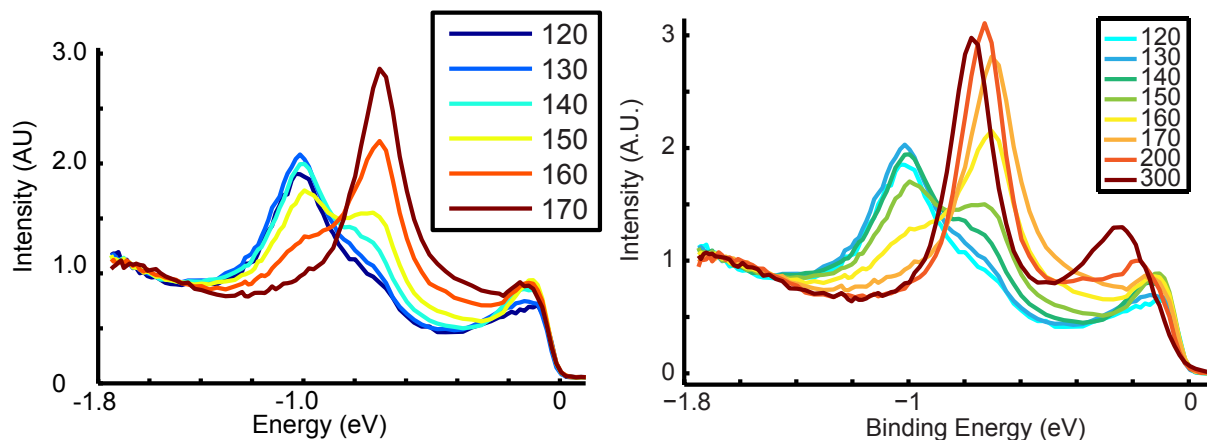


Figure 5.4: Temperature dependent phase transition from the island to gas phase showing a pseudo-isosbestic point (a) and a shift in energy of the gas phase peak with increasing gas-phase density.

In the range of 120 – 170K and approximate isosbestic point is observed. A true isosbestic point identifies one molecular species transforming into a second species with a 1-1 ratio. A true isosbestic point requires a concentration independent position of a spectroscopic peak, however, a condition which is not maintained here.

The image state energy is coverage dependent during dosing at 300K, and it is coverage dependent. At cold temperatures, the surface contains only crystalline islands. As the temperature increases, the number and density of the 2D-gas phase increases, and the image state moves to lower energies. This is observed in the TPPE spectrum at temperatures above 170K.

Repeating our TPPE dosing survey at 200K, at a dosing rate of 0.01ML/minute, the image state is found to grow in at a constant energy equal to the energy observed for the full monolayer. The image state experiences a local work function equal to the work function of the monolayer. In this case, we can conclude that the phthalocyanines cluster at cold temperatures, similar to the observation found by Umbach at all. Our LEED spectra of the low submonolayer coverages at cold temperatures cannot be distinguished from those observed at high coverages while dosing at room temperature. It is likely that the difference between the two crystal structures cannot be distinguished by the low resolution of our spectrometer.

Dosing TiOPc on a substrate held at 200K at a rate of 0.01ML/minute, the image state is found to have an energy slightly above that of the full monolayer. Further, the image state is found to "wobble" as a function of coverage. In the dosing survey, the phthalocyanines are dose in short bursts, followed by a short period of zero dosing rate while the crystal is first turned towards the detector, and then a spectra is taken. It is proposed that the "wobble" in the image state energy is due to a dosing rate faster than the phthalocyanines can collapse into clusters. The "wobble" is thus due to a slight difference in the rate at which the sample is manually turned towards the detector for each scan.

Slow diffusion and reorganizational kinetics may be important to the phase diagram of submonolayer phthalocyanines. A coverage near 0.2ML of TiOPc dosed on the crystal at 200K at a rate above 0.1ML/minute is assumed to be a rate faster than the sample is able to reach equilibrium. Following this, the sample is allowed to relax, while TPPE spectra are taken as shown in Figure 5.3. The initial spectrum shows two peaks, a sharp peak corresponding to the image state of regions of bare Ag(111) remaining on the sample. The second, broad peak results from a IPS

in the TiOPc coverage. The IPS observed here is non-gaussian, but it is in the range of 200meV above the energy of the IPS peak of the crystalline monolayer or clusters.

Over the course of 4 hours, this peak is found to shift to higher energies, while the IPS of bare Ag(111) increases in intensity. The $0.01\text{ML}/\text{minute}$ dosing survey showed that the equilibrium, or semi-equilibrium, growth mode is the crystalline growth mode. As the non-equilibrium coverage of 2D-gas like molecules collapse into islands, more regions of bare Ag(111) are exposed. The IPS of the island phase is too small to be observed at this low coverage. As the molecules condense into the cluster phase, however, the intermolecular distance of the 2D-gas-like molecules increases, causing the work function to increase and the peak to shift to higher energies. The intensity of the 2D-gas peak also decreases because the number of molecules in this phase decreases and the number of allowed states decreases.

This phase change is found to be nearly complete within 3 hours. It is possible that this is the time scale required for the phthalocyanines to diffuse to the closest small cluster, and form aggregates. The time required for the reorganization of 0.1ML of 2D-gas molecules into the cluster phase is equal to the total time required for the dosing survey from $0 - 1\text{ML}$ in the equilibrium growth of TiOPc at $0.01\text{ML}/\text{minute}$ in which the molecules are found to fall into only the cluster phase. If 3 hours were the timescale required only for diffusion of the 2D-gas molecules to clusters, a required dosing rate of $1e-3\text{ML}/\text{minute}$ would be required for equilibrium dosing. The discrepancy between the reorganizational kinetics of the non-equilibrium and equilibrium dosing suggests an additional kinetic barrier.

Preliminary results show a phase change between the 2D-gas and island phases on the surface, but they do not indicate the order of this phase transition. Further, they have not yet answered the question of whether these molecules have an attractive or repulsive intermolecular interaction.

5.4 Kinetic Monte Carlo Simulations

The Ising model, which is a two state variation of the generalized Potts model, is a powerful model for describing intermolecular interactions and phase transitions in systems containing only two states. The 2D-Ising model has thus been used extensively to understand behavior of ferromagnetic and antiferromagnetic materials near the Curie temperature.

Many different Monte Carlo implementations of the 2D-Ising model have been utilized. In each of these implementations, the spins of neighboring atoms or coarse-grained regions are treated as spins of $\pm\frac{1}{2}$. A distance-dependent energy of interaction is assigned to these spins, often simplified to a nearest neighbor attraction or repulsion. These simulations are able to identify order and disorder phenomena as a function of temperature, magnetic field (treated as an energy of interaction), and time.

The most common implementation of Monte Carlo simulation was the Metropolis algorithm. In this implementation, a spin is allowed to flip from $+\frac{1}{2}$ to $-\frac{1}{2}$ and vice versa during a given time step. This implementation does not conserve spin, and in the presence of a magnetic field or in the case of a small ensemble, the spins may all flip to $+\frac{1}{2}$ or $-\frac{1}{2}$. The Kawasaki implementation of Monte Carlo is spin conserving, such that only spins of opposite sign may exchange. A kinetic variation of this model allows spin exchange only between neighboring sites.

Here, we implement a Monte Carlo simulation that is an on-lattice implementation of a kinetic Kawasaki Ising model. The on-lattice implementation we use here is particularly suited to adsorbed molecules such as phthalocyanines on a single crystal metal surface. Molecules on a metal surface have a preferred orientation relative to the substrate crystal structure. A molecule

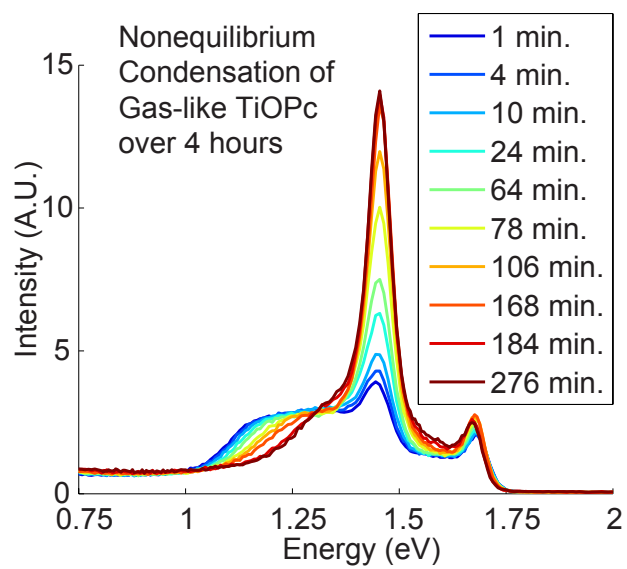


Figure 5.5: Slow kinetics of condensation at 0.1 ML coverage and 200 K. The gas-phase peak decreases in intensity due to condensation while the peak due to bare Ag(111) increases in intensity.

on a metal surface will hop between energetically favored positions which may be on top of a metal atom, on a bridge site or in a hollow site. In analogy to spins, which can flip up or down in a magnetic material, a molecule can be treated as having a spin of unity, and a vacant site can be treated as having a spin of zero. In this manner, molecules can be assigned a distance dependent energy of interaction, while the vacant sites do not directly contribute to the energy of the system. In this Kawasaki type model, molecules are allowed to move in a random walk to any adjacent site that is not occupied, i.e. one with a spin of zero. This type of model has distinct advantages because it directly simulates the diffusive motion of a molecule on a surface. This type of model can also be extended to an arbitrarily complex intermolecular potential, as has been suggested in the literature. For a large enough system, propagated for a long period of time, the statistical behavior of the kinetic Monte Carlo (KMC) simulation will approach thermal equilibrium.

5.5 Kinetic Monte Carlo on a Discrete Lattice

The Monte Carlo methods we employ involve the diffusive random walk of phthalocyanine molecules on a hexagonal lattice representing the Ag(111) lattice. Phthalocyanine molecules are allowed to hop diffusively across the surface. The molecules obey ‘hard sphere’ type motions, which is accomplished by rejecting any move that results in overlap of two molecules. Similarly, the force between molecules is treated as an energy calculated based upon proximity to other molecules.

The phthalocyanine molecules themselves are centered on a single Ag atom. Hops are discretized as being only to adjacent Ag atoms. This approximation is in line with experimental observations of commensurate packing in FePc/Ag(111) or point-on-line packing of CuPc/Ag(111). These observations support a favorable position of the phthalocyanine molecules relative to the Ag(111) lattice. The commensurate packing suggests a stronger molecule-metal binding affinity and requires a slight distortion of the phthalocyanine unit cell. These two packing arrangements can be treated by allowing either full-steps or half-steps to neighboring lattice sites. Typical runs involve a substrate size of at least 1×10^4 lattice sites. This simulation size corresponds to a Ag(111) terrace size of 300 Å on a side, which is comparable to the limits of experimentally achievable defect-free terraces. Edge effects are further reduced by using periodic boundary conditions.

The phthalocyanine molecules themselves are treated as an occupied region of lattice sites. The occupied region replicates the experimentally determined molecule size and orientation. The molecules appear as cross-shaped regions, with the lobes of the molecules oriented 30° from the Ag(011) lattice dimension.

A molecular move consists of either a rotation by 30° or a translation to one of six neighboring lattice sites, following detailed balance. A move attempt is accepted based upon the Metropolis algorithm. If the energy of the system is lowered after the move, then the move is accepted. If the energy of the system is increased after the move, then the move is only accepted based upon a Boltzmann acceptance rate for a given temperature.

In this simulation, a molecule is randomly selected for each move. A time-step is defined as the time required to probabilistically move each atom once. For N-atoms, there are N move attempts of randomly selected molecules in each time-step. In preliminary investigations, the necessary timescale for reaching equilibrium was estimated by allowing an ensemble of molecules to relax over 1×10^7 time-steps. The energy was measured at each time step. The energy was found to decay rapidly for the first 1×10^3 steps, and more slowly, with approximately exponential behavior subsequently. Subsequently, most investigations involve 1×10^4 time-steps for a given small perturbation to the system. The code was optimized for speed, such that 1×10^4 time-steps are achieved for a typical run size of 200 atoms within 15-20 minutes. Although significant speed

improvements may be possible through better coding or parallelization, a typical rate of 7×10^3 move attempts per molecule per second (on a modern desktop computer) was found to be adequate for our purposes.

In the simulation, the energy of the system is monitored by the total number of bonds formed between neighboring atoms. The crystallinity of the phthalocyanines allows formation of 0–4 nearest neighbor bonds. The number of gas phase and cluster phase molecules is also determined by a separate cluster counting script. The intermolecular separation is directly calculated as the radial distribution function, which is calculated with periodic boundary conditions.

5.6 Monte Carlo Results

Previous studies have suggested that phthalocyanine molecules adsorbed on a metal or graphite substrate have a repulsive intermolecular interaction, or a complex energy of interaction involving both repulsive and attractive components. In our simulations, we have only been able to achieve condensation of the phthalocyanine molecules with an attractive potential. Molecules with zero or negative energies of interaction were not found to crystallize even at high temperatures. Although a complex potential containing both attractive and repulsive terms is possible, we begin by treating only the purely attractive potential.

We employ the simplest potential possible, a single point, nearest neighbor attraction. The strength of this attractive potential was empirically set to 50meV . A phase transition is typically expected in a single particle system when the energy of interaction is in near $2 - 4k_B T$, the available kinetic energy of the system. This potential energy could be expected for a phase transition in the temperature range of $150 - 300\text{K}$. Coincidentally, one recent paper utilizing density functional theory has predicted a nearly identical energy of interaction. In this paper, they found an attractive energy of 50meV localized to a very small region of interaction between two CuPc molecules. They also found a repulsive interaction of 10meV at all greater distances. As this potential as flat as a function of distance, however, it does not have a potential energy gradient and cannot be predicted to affect a force on a molecular pair interaction. The localized attractive potential of interaction has a short ranged and sharp gradient of interaction and will create an attractive force between molecules.

The Monte Carlo simulation was used to predict the density dependent phase transitions previously observed in LEED simulation. In order to do this, molecules were added one at a time to an empty Ag(111) lattice. Between adding each new molecule, the system was allowed to relax for between 5×10^2 and 2×10^{10} time steps. This *in silico* experiment reproduces the experimental dosing survey. This technique is less standard in statistical simulations. In statistical simulations, it is much more common to have a constant number of molecules and change either the size of the molecules or the size of the system. As the molecules in this system have both well-defined size and shape, however, changing their size is not possible in a lattice model. Increasing or reducing the size of the lattice is also difficult in a lattice system as it is also difficult. Increasing the size of a lattice-constrained system is often accomplished by adding or removing a lattice row. This is difficult in our system due to the large likelihood of one or molecules crossing any lattice row that is added or removed.

In this simulation, the energy, radial distribution, and cluster size distribution were all calculated as a function of coverage. In this simulation, the system is allowed to relax for a constant 1×10^4 time steps with each addition of a molecule. Figure 5.6 shows the ratio of 2D-cluster to 2D-gas phase molecules as a function of coverage for several different substrate temperatures. The enthalpy of the system is proportional to the number of bonds. In the figure, the phases are defined

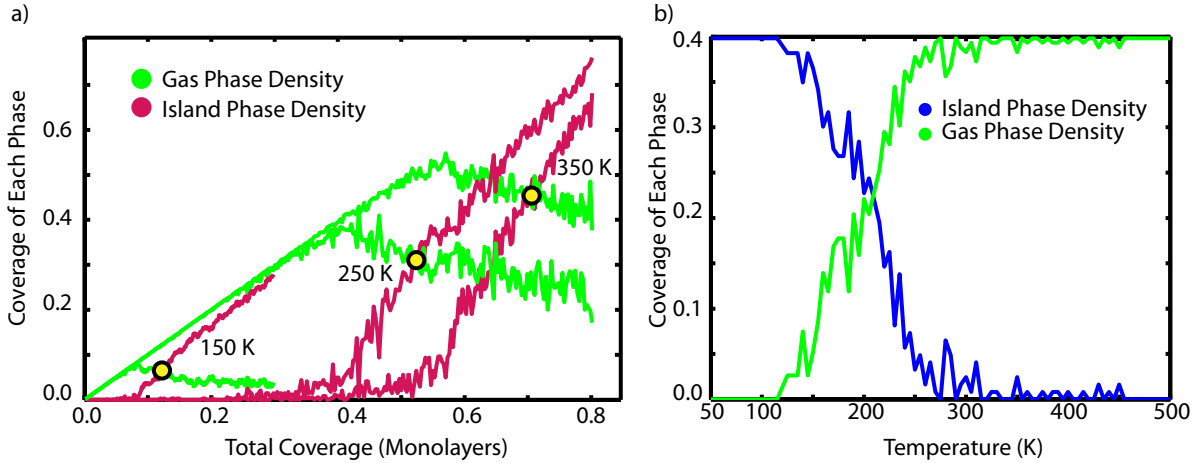


Figure 5.6: Monte Carlo results showing a) dosing dependent relative coverages of each phase and b) temperature dependence of the relative coverages of island and gas phases for 0.4 ML total dosing.

qualitatively, with the gas phase molecules being those with 0 – 1 bonds and the cluster phase defined as molecules with 2 or more bonds. Qualitative measurements are preliminary, and they will be replaced with more quantitative measurements.

It is found that the system remains entirely in the 2D gas phase up to some critical total coverage. Below this coverage the cluster phase density increases linearly, and it is equal to the total coverage. At the critical total coverage, the cluster phase begins to form. Above the critical coverage, all added molecules collapse to the condensed cluster phase. Further, the critical coverage required increases with the system temperature. Assuming equilibrium growth, the critical behavior can be described by the equation derived by Hill for 2D clusters of Helium [68].

$$\frac{d(\ln\Phi_{trans})}{d(1/T_s)} = \frac{H_{2g} - H_{2c}}{kT_s} \quad (5.1)$$

Here T_s is the substrate temperature and H_{2g} and H_{2c} are the enthalpies of the gas and cluster phases, respectfully. The variable Φ_{trans} is the critical 2D pressure corresponding to the phase transition. This equation predicts that for a first-order phase transition at equilibrium, the lower enthalpy cluster phase will begin to form at a critical pressure, as we see in our simulation results. This is also consistent with the previously published LEED experiment. Further, pressure and corresponding coverage of the molecular adlayer required to form the cluster phase will increase with increasing temperature. The slope of the 2D-gas/2D-cluster phase diagram results from the sign of the difference in enthalpy of the two phases.

5.7 Non-Equilibrium Kinetics

Up to this point, the system has been assumed to be at or near equilibrium. Although there has been some effort to quantify the ensemble relaxation and choose reorganizational time-scale accordingly, this does not guarantee equilibrium, especially in a KMC simulation. Here we have difficulties, as the experimentally denoted diffusion rate of a system is a required input parameter to a KMC simulation, but a simulation cannot be used to predict experimental diffusion rates.

Further, because there is a first order phase transition, two relaxation times may occur, one for the relaxation of individual molecules, and a second for obtaining equilibrium of clusters.

We explore this first in the context of obtaining equilibrium of individual molecules. In a first-order phase transition, discontinuity or kinetic effects are typically not observed as the temperature of the system is varied. In Figure 5.6, the temperature of an ensemble of 200 molecules with a packing density of 0.4 *monolayers* is varied. In the figure shown, the temperature decreases by 1K per 1×10^4 time steps. The observed number of molecules in the 2D-gas and 2D-cluster phases are plotted as a function of temperature. The observed density of each phase follows the sigmoidal shape expected for a temperature dependent change in phase, 5.2.

$$\Phi(T) = \frac{\Phi_A}{1 + \exp T - T_0/D} + \frac{\Phi_B}{1 + \exp T - T_0/D} \quad (5.2)$$

This equation, discussed in more detail in the section on room temperature ionic liquids predicts a sigmoidal temperature dependence about a critical temperature T_0 to a spectroscopic observable $\Phi(T)$ with a broadening factor D . The spectroscopic observable is typically an intensity or peak position proportional to the number of molecules in a particular phase, however, here the KMC simulation is able to directly measure the absolute number of molecules in a particular phase. As such, we observe that the KMC predictions for the number of molecules in a phase match the expected sigmoidal shape.

The temperature dependent concentrations of a phase transitions can be expected to show discontinuities or hysteresis[1, 3, 13]. Hysteresis is characterized by increasing and decreasing the temperature of an ensemble of molecules while monitoring the densities of each phase. Preliminary results using 1K per 1×10^4 time steps have observed small hysteresis and no discontinuities. Discontinuities can also occur due to the finite size of a system, and the continuity we observe suggests an adequate size ensemble. From these results, it can be determined that the time-scale for molecular equilibrium is exceeded, and more detailed studies are under way.

Coverage dependent phase can be expected to show a discontinuity, or more commonly, a hysteresis in the relative abundance of each phase. This phenomena is commonly observed in the absorption isotherms of noble gases[33]. Because the coverage dependent or pressure dependent change in phase is a true phase transition, kinetic barriers can be expected. The most prominent kinetic barrier results from metastable clusters. Surface tension will allow a larger cluster to be more stable than a smaller cluster. During absorption isotherm experiments, the concentration of cluster phase molecules at a given ensemble coverage is higher during desorption than absorption because of these metastable clusters.

Hysteresis in concentration of 2D-cluster phase and 2D-island phases is explored by an a simulation of an adsorption-desorption experiment. During adsorption, a molecule is randomly placed on an empty location on the lattice every 1×10^4 time steps. During desorption Figure 5.7 shows the ratio of island:gas phase while dosing and removing molecules at a temperature of 200K. Above 0.4 *Monolayers* and below 0.2 *Monolayers*, the ratio of island:gas are identical upon dosing and removal. The system is in equilibrium above and below these critical coverages. Between 0.2 and 0.4 *Monolayers*, however, the system shows notable hysteresis. The ratio of island:gas phase molecules is significantly higher upon removal than during adsorption. This directly supports a first order phase transition in this system.

5.8 Future Work

In the preceding sections, we have laid some of the groundwork for determining the nature of the phase transition between the 2D-cluster and 2D-gas phases of phthalocyanines on Ag(111).

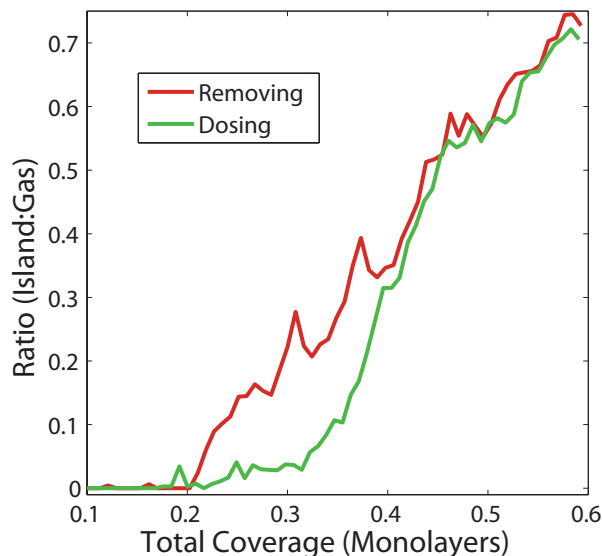


Figure 5.7: Hysteresis in the relative coverages of each phase upon dosing and removal indicates a nonequilibrium first order phase change.

Several notable advances have been accomplished. We have experimentally shown that the transition between the gas and cluster phases can be observed by the IPS energy and intensity. This transition has been observed as a function of temperature, coverage, and sample relaxation time. We have also experimentally shown that the dipole moment of TiOPc relative to the zero dipole of CuPc is relatively unimportant to understanding the phase transition on Ag(111). We have also developed a quantitative KMC model. This model suggests that the intermolecular enthalpy is attractive, strongly favoring one side of a current debate in the literature. The KMC has been used to qualitatively predict temperature, coverage, and kinetic effects.

A quantitative comparison between simulation and experiment is still lacking. This is partly due to the qualitative measures so far implemented in analyzing the KMC simulation output. Implementation of the script for identifying individual clusters is important to this. Up to this point, an arbitrary distinction between the island and gas phase has been made, based upon number of nearest neighbor bonds. This distinction can be formalized by counting the number of molecules in a cluster. Pairs or triples of molecules may spontaneously occur in the gas phase, but they may be unstable. The distinction between the gas and cluster phases can be formalized by finding the minimum in a histogram of cluster size. The code to identify clusters will also aid in identifying a metastable cluster size. Finally, adding a script to identify the 2D-pressure of the gas phase molecules will aid in a more quantitative analysis of the thermodynamic parameters of this phase change.

The KMC simulation was able to identify a phase transition based upon the hysteresis in the adsorption/desorption curve. A desorption curve is not available experimentally, as the molecules are grown by molecular beam and do not desorb up to temperatures above 600K. As a result, experimental evidence for hysteresis, a first order phase transition, or kinetic barriers is limited. The slow kinetics of cluster reorganization observed in the non-equilibrium growth at 200K may be the only method for observing this kinetic barrier. In order to better quantify this, the reorganizational experiment will be repeated at a few different coverages. At a critical coverage and temperature, the reorganizational kinetics are expected to be strongly observed, while above

and below that temperature, the system is expected to be closer to equilibrium. The system is also expected to show a different hysteresis as a function of temperature at a given coverage. The current experimental results show that the relative abundances of each phase can be observed as a function of temperature, but possible hysteresis has not been explored[29]. Hysteresis will be explored by cycling the temperature of sample.

In conclusion, we have produced experimental results that suggest a non-equilibrium phase transition between a 2D-gas phase and 2D-cluster phase molecular adlayer. Our analysis draws heavily on the statistics of 2-dimensional phase transitions, which have been well studied and understood for several decades. Our analysis is the first to apply these methods to a large molecule like phthalocyanines. We draw a quantitative connection between well understood adsorption isotherms of noble gases and less well understood mechanisms of epitaxial growth from a molecular beam. We expect our results will be general and applicable to understanding growth mechanisms in a wide range of molecules and substrates.

Chapter 6

Selection Rules and Classical Quenching at the Molecule / Metal Interface

6.1 Introduction

Two photon photoemission spectroscopy is sensitive to several types of surface and bulk states existing at the interface between two materials. These states include both occupied and unoccupied states belonging to both a molecular adlayer or to the substrate, which is commonly an inorganic semiconductor or metal. Successful experiments require a prior knowledge of what states may be observed. Further, given experimental spectra, assignment of these states may be difficult and easy to confuse.

Molecular orbital derived states at the interface may have a significantly different energy than than the bulk, solution, or gas phase of the same material. Surface states also have dramatically different energies and dispersions as a result of interaction with the dielectric constant of the overlayer or as a result of mixing of molecular orbitals. The image states at the metal-vacuum interface is expected to form a Rydberg progression, with a minimum energy of 0.85 eV below the vacuum level. The presense of a an overlayer dramatically moves this energy level. For a molecular film with a repulsive electron affinity, the image state will be higher in energy, and the maximum intensity of the wavefunction moves towards the vacuum. Similarly, a molecular overlayer with an attractive electron affinity pulls the electron towards the metal interface and lowers the energy of the image state. This energy shift can be complicated by quantum well formation of the first two image states. The surface state of a metal substrate is also found either above or below the Fermi level. The surface state of clean Ag(111) resides 100 meV below the Fermi level. With the addition of 3,4,9,10-Perylenetetracarboxylic dianhydride (PTCDA), however, the surface state moves $0.6 - 1.0\text{ eV}$ above the Fermi level. This state is expected to be coincident in energy with the LUMO+1 of the PTCDA. Investigations of the this band by multiple techniques have alternately assigned the spectral feature as a surface state or a LUMO+1 state. Only recently two photon photoemission spectroscopy has the upshifted surface state is due to a mixing of the surface state of Ag(111) with the molecular orbitals of PTCDA. These results rely heavily on computationally expensive planewave density functional theory calculations. The computational and experimental difficulty in assigning metal to molecule optical excitations suggests the need for additional and simpler theoretical approaches.

The mechanism for charge transfer excitation has been debated at the metal-molecule

interace. In general, charge transfer excitations have significantly lower optical cross section due to the small overlap between the initial and final wavefunctions. As a result, photoinduced indirect electron transfer has been proposed as a mechanism for metal-molecule charge transfer excitations. In this mechanism, hot electrons is excited within the metal substrate. Hot electrons travel to the surface and subsequently relax to a molecular state or a surface state residing in the molecule.

Photoinduced direct charge transfer electronic excitations are optically allowed, however, and can be understood through group theory and resultant optical selection rules. We propose here that the direct charge transfer excitation is strongly favored at the metal-molecule interface. We have found no evidence for indirect electron tranfer of hot electrons in systems of adsorbed molecules on Ag(111). Because the direct process is strongly favored, group theory can be applied to identify spectroscopic observations. Further, we propose that optical selection rules can allow selective excitation of one of two degenerate levels with different symmetry. In this method, the properties of degenerate states can be distinguished in a manner inaccessible to all optical techniques.

6.2 Orbital Symmetry and Optical Selection Rules

Optical selection rules are derived from an application of group theory to the electronic wavefunctions of a system. It is perhaps trivial to the reader that molecules have symmetry, and they can be assigned to point groups. Electrons are Fermions, and as a result, they mus occupy orthonormal wavefunctions. In a molecule, electronic wavefunctions also have symmetry which can be assigned a symmetry label within the point group of the molecule. The transition dipole of an vibronic excitation is calculated as:

$$\mu_{fi} = \langle \epsilon_f \nu_f | \hat{\mu} | \epsilon_i \nu_i \rangle \quad (6.1)$$

Here, μ_{fi} is the transition dipole moment and $\hat{\mu}$ is the transition dipole operator. The wavefunctions of the initial and final state are defined by $\epsilon_f \nu_f$ and $\epsilon_i \nu_i$. This equation treats all vibronically allowed excitations, however, for excitations from the ground vibrational state we typically only need consider the electronic term. In a group theory, an excitation is determined to be optically allowed or disallowed by replacing the matrix elements in the above equation with the symmetry labels of each of the components. A transition is electronically allowed if:

$$A_1 \in \Gamma(\epsilon_f) \times \Gamma(\vec{\mu}) \times \Gamma(\epsilon_i) \quad (6.2)$$

where we have replaced the wavefunctions and electric field vectors used in calculating the transition dipole moment by the matrices characterizing the symmetry of each component. The term Γ refers to the irreducible representations of the wavefunctions and the transition dipole operator. An optical transition is allowed if the direct product of these irreducible representations is A_1 , which always refers to the totally symmetric irreducible representation. Transitions with character A_1 are allowed because the probability of transition is calculated as square of the integral over all space. Only symmetric solutions can be nonzero.

The term $\Gamma(\vec{\mu})$ in equation 6.2 is the electric field vector of the incident light. The electric field vector (x, y, or z) has a irreducible representation which can be determined from the character table for the molecule or system in question. At the surface of a metal, electric fields parallel to the metal surface are cancelled by the induced dipole within the metal. This results in the metal surface selection rule, which states that transitions are only allowed with electric field vectors perpendicular to the plane of the surface. The electric field vecotor for an allowed surface exitation, z, will always have the totally symmetric character A_1 for any system.

While the surface selection rule is completely true for infrared excitations, this rule becomes less strong near the surface plasmon resonance. The surface plasmon resonance is a resonance

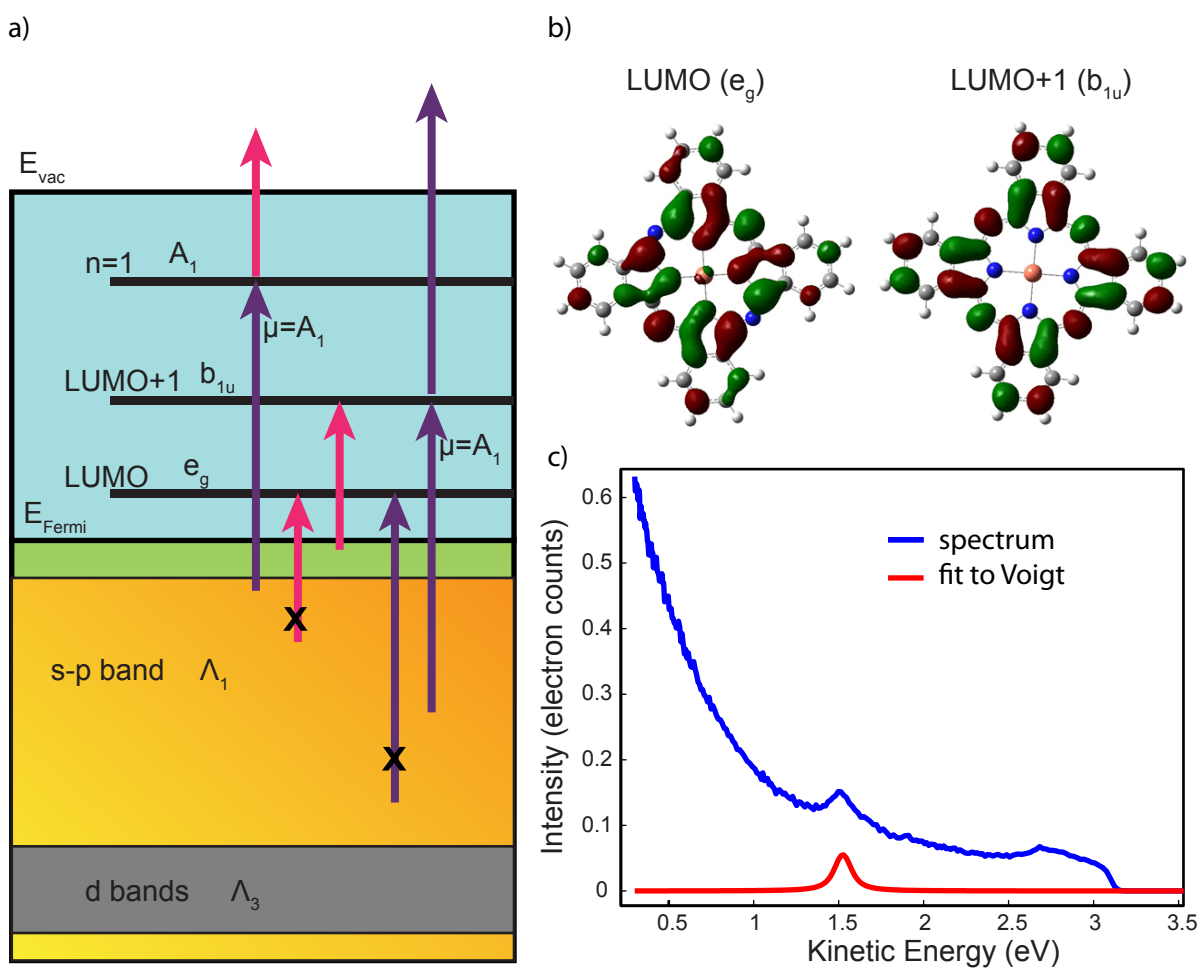


Figure 6.1: a) Optical selection rules for CuPc / Ag(111). b) symmetry of the LUMO and LUMO+1. c) TPPE spectrum of the LUMO+1

CuPc				C60	
C4v	C2v	C2v		I	C3
	σ_v	σ_d		A	A2
A1	A1	A1	LUMO+1	T1	A+E
A2	A2	A2		T2	A+E
B1	A1	A2	HOMO	G	2A+E
B2	A2	A1		H	A+2E
E	B1+B2	B1+B2	LUMO		

Table 6.1: Correlation tables for gas phase and adsorbed CuPc and C_{60}

that occurs due to the maximum rate with which the electrons in a metal can respond to an oscillating electric field. For Ag(111) the surface plasmon resonance is 3.5 eV, and as a result, optical excitations parallel to the interface in the frequencies considered will be dampened by 1 – 2 orders of magnitude. These selection rules become less stringent for Au and Cu, which have lower energy surface plasmon resonances.

The symmetry labels of the molecular orbitals can be calculated using computationally inexpensive density functional theory. The calculated symmetries of the LUMO and LUMO+1 molecular orbitals of copper phthalocyanine are shown in figure 6.2 a). When the molecule adsorbs on a metal surface, however, the symmetry of the molecule and the irreducible representations of the molecular orbitals will change. The relations between the irreducible representations of a high symmetry gas phase molecule and those of a lower symmetry molecule adsorbed on a metal surface can be calculated by hand or looked up in a correlation table or a table of compatibility relations.

For CuPc, the gas phase symmetry of the molecule is D_4 , while for TiOPc, the oxygen atom lowers the symmetry slightly to C_{4v} . In both cases, the symmetry of the molecular orbitals reduces to C_2 upon adsorption to the surface. From the correlation tables (Table 6.2), the LUMO+1 of CuPc reduces to A1 symmetry, while the LUMO of E symmetry reduces to $B1 + B2$. Similarly for the metal, the SP-orbitals have A1 symmetry, while the D-orbitals have E or $B1 + B2$ symmetry. We take the opportunity to point out that, in extended systems, Greek letters are typically used as symmetry labels. The Λ symmetry in Figure 6.2 refers to the line from the center of the Ag(111) Brillouin zone to the corner of a hexagonal face of the Brillouin zone ($\bar{\Gamma} - \bar{M}$).

These symmetry labels are used to calculate the selection rules excitations from the bulk bands of the metal to the conduction bands of CuPc. The optical transition from the Ag SP band to the LUMO+1 of CuPc is allowed, with transition dipole perpendicular to the surface. The optical transition from the Ag D-bands to the CuPc LUMO is optically allowed, with transition dipole perpendicular to the interface. The image state also has A symmetry, and as a result, has transition dipole perpendicular to the interface.

Because only transition dipoles perpendicular to the surface are observed due to the metal surface selection rule, only the IPS and the LUMO+1 will be allowed transitions from the SP-band. Further, because the D-bands are 3.5 eV below the Fermi level, or 4.5 eV below the CuPc LUMO level, and the workfunction is 4.1 eV, the CuPc LUMO will never be observed in a two color TPPE experiment on Ag(111). Although an empirical null proof is always impossible, we can point out

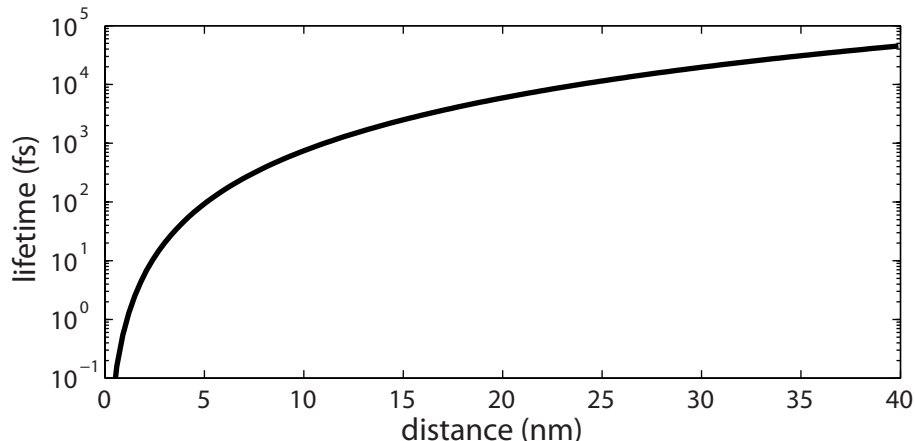


Figure 6.2: Lifetimes from classical quenching of the top monolayer of thick films of ZnPc / Ag(111)

that we have observed image state of CuPc. We have also observed the LUMO+1. The LUMO+1 spectra is shown in figure 6.2. The LUMO is located approximately 2.2 eV above the Fermi level. To observe this peak, we have used one-color TPPE with 3.8 eV light. Preliminary wavelength surveys confirm that this peak moves with the wavelength of the UV light. Although the LUMO cannot be observed by TPPE on Ag(111), the d-bands of Au and Cu are known to be significantly higher in energy. As a result, the optical transition from the Au or Cu D-band to the CuPc LUMO will be possible using light with energy less than the workfunction. Further, optical transitions parallel to the surface may also be observed, as the surface plasmon is lower in energy, and screening of electric fields parallel to the interface will be less stringent for visible and ultraviolet wavelengths.

We can generalize these results: an unoccupied electronic state with A symmetry has an optically allowed transition from the SP-bands, while an unoccupied electronic state with E symmetry has an optically allowed transition from the D-bands. Further, as A bands are dispersive, while E bands are flat (by symmetry), angle resolved TPPE on Ag(111) will strongly favor observation of dispersive features. The LUMO of CuPc is also found to be dispersive, with a positive curvature (data not shown).

A question remains as to the strength of these selection rules. Can TPPE be used to selectively excite degenerate electronic bands with different symmetry? The highly symmetric molecule C_{60} has icosahedral symmetry, and the HOMO through LUMO+N bands are 2 – 5 fold symmetric, as pointed out in the correlation table for C_{60} (Table 6.2). Upon adsorption on a 3-fold symmetric substrate, these bands collapse to degenerate or nearly degenerate electronic states with dispersive or non-dispersive character. By selective excitation from the SP-band or D-bands using different wavelength pump pulses, the dispersive and non-dispersive modes may be separable.

6.3 Identifying Excitons

TPPE is a potentially very powerful technique for understanding exciton dynamics. TPPE is uniquely capable of probing the energy of the electronic state relative to the Fermi level. Further TPPE has the femtosecond time resolution required to follow exciton dynamics, which typically occur on the time scales of 10 fs to several ns. As a result, such effort has recently made on investigations of molecular exciton dynamics using TPPE.

Several groups have recently been able to observe excitons in thin films of anthracene,

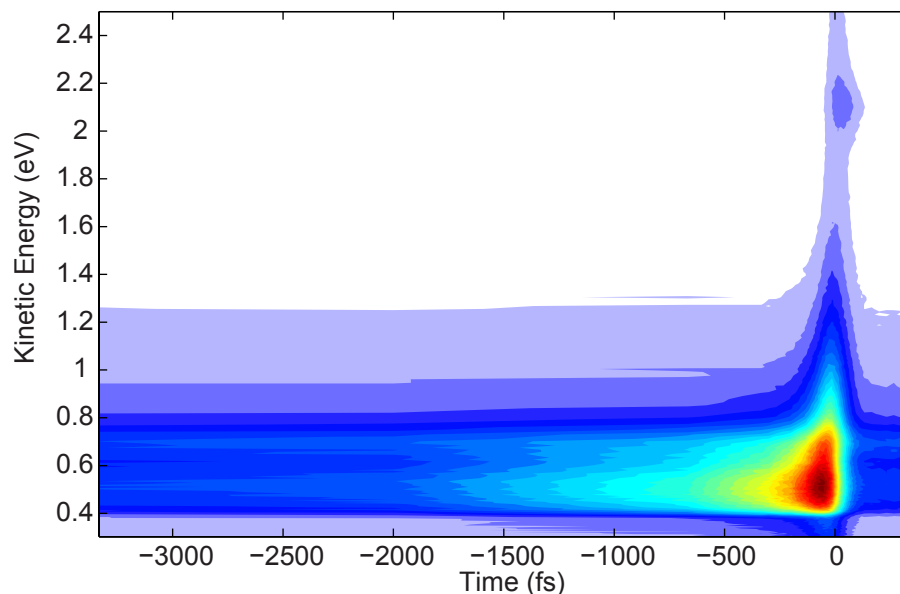


Figure 6.3: Exciton or low energy scatter of CuPc / Ag(111)

sixithiophene, and CuPc. In order to observe the exciton, however, each of these studies has had to overcome classical dipole quenching by the metal substrate. Classical dipole quenching will cause the exciton lifetime in thin films on a metal surface to decrease by several orders of magnitude, as shown for *ZnPc/Ag(111)* in Figure 6.3. In this figure, the lifetime of the exciton in a monolayer ZnPc is plotted using a spacer layer of some number of molecules of ZnPc. It is seen here that in the first 1-2 ML of an adsorbate on a metal substrate, classical quenching will reduce the exciton lifetime to below 10 fs. The lifetime does not extend beyond a picosecond until tens of molecules of a spacer layer have been placed between the molecular film and metal substrate. Although we have only plotted results here for a thin film of *ZnPc/Ag(111)*, the same trend holds qualitatively for any molecular semiconductor on a metal substrate.

In order to circumvent the limitations of classical quenching, several molecules were used as spacer layers to separate a molecular layer of CuPc from the Ag(111) substrate. Attempts to use spacer layers of alkylthiophenes and fullerenes were unsuccessful. Finally, a thick film of 50 *ML* CuPc was used in order to simulate a spacer layer of CuPc on CuPc on Ag(111). With this thin film, a large low energy feature was observed (Figure 6.3). This feature had a large negative lifetime on the order of a 1 – 2 picoseconds. The negative lifetime of this feature results from a visible-pump UV-probe spectrum in our experimental setup. Further, the this feature is located 0.5 eV above the Fermi level, in close agreement with the expected 0.9 eV above the vacuum level based upon vacuum level alignment. Finally, this state has a lifetime that is much longer lived than other states previously observed in this material. The 1 – 2 *ps* lifetime is in close agreement with the expectation for lifetime of an image state based upon classical quenching for a 10 *nm* thick film.

Upon closer inspection, however, the IPS of the 1 *ML CuPc/Ag(111)* is clearly visible in this spectrum. Under the dosing conditions used in this spectrum, the growth mode is found to be a 1 *ML* wetting layer followed by island-type growth of crystalline needles. The IPS remains in the spectrum because large sections of the substrate are only covered with a single *ML*. The high temperature substrate, 475 *K* in the data here, was necessary to maintain a crystalline coverage in LEED spectra. It may be possible that the low energy feature is an exciton from the regions of

needle crystals. Also supporting this, a recent study of *CuPc/C₆₀/Ag(111)* found a feature in the same region, and this was assigned as an exciton of the CuPc.

To more carefully investigate this, we examined a highly ordered single *ML* of *CuPc/Ag(111)*. In this coverage, the same spectral feature was observed, with a somewhat shorter lifetime. A shorter lifetime is expected for an exciton in a single *ML*, though the lifetime is much longer than the $< 10fs$ expected. Further, the transition dipole moment of the HOMO-LUMO gap is in the plane of the substrate, as determined by the symmetry labels of the HOMO and LUMO and the orientation of the molecule on the substrate. Breaking of the surface selection rule near the surface plasmon resonance, however polarization experiments did not reveal any state upon using a p-polarized pump pulse.

The exciton is not expected to be observed for flat-lying *CuPc/Ag(111)*, and the assignment of this low energy feature as another type of state is supported by unsuccessful studies coverage and polarization dependence. We tentatively assign this state to be a surface state, upshifted from the Fermi level by hybridization with the molecular orbitals of CuPc. The symmetry expected for a surface state may be able to distinguish it from non-resonant low-energy scattering. The surface state, like the image state, has an *A1* symmetry, and is dipole allowed. This state is expected to be dispersive. Further studies are under way to examine the band curvature of this state. A positive curvature of the low energy state may confirm its identity as an upshifted surface state.

Bibliography

- [1] GS AGARWAL and SR SHENOY. Observability of hysteresis in 1st-order equilibrium and non-equilibrium phase-transitions. *Physical Review a*, 23(5):2719–2723, 1981.
- [2] JS ALPER and RI GELB. Standard errors and confidence-intervals in nonlinear-regression - comparison of monte-carlo and parametric statistics. *Journal of Physical Chemistry*, 94(11):4747–4751, 1990.
- [3] D Arndt, S Fassbender, M Enderle, and K Knorr. 2d ising critical behavior at an isomorphous structural phase transition in c2f6 monolayers physisorbed on graphite. *Physical Review Letters*, 80(8):1686–1689, 1998.
- [4] S Arzhantsev, H Jin, GA Baker, and M Maroncelli. Measurements of the complete solvation response in ionic liquids. *Journal of Physical Chemistry B*, 111(18):4978–4989, 2007.
- [5] R Atkin, SZ El Abedin, R Hayes, LHS Gasparotto, N Borisenko, and F Endres. Afm and stm studies on the surface interaction of [bmp]tfsa and (emim)tfsa ionic liquids with au(111). *J. Phys. Chem. C*, 113(30):13266–13272, 2009.
- [6] S Baldelli. Surface structure at the ionic liquid-electrified metal interface. *Accounts of Chemical Research*, 41(3):421–431, 2008.
- [7] LE ”Barrosse-Antle, AM Bond, RG Compton, AM O’Mahony, EI Rogers, and DS” Silvester. Voltammetry in room temperature ionic liquids: Comparisons and contrasts with conventional electrochemical solvents. *Chemistry-an Asian Journal*, 5(2):202–230, 2010.
- [8] S Berner, M Brunner, L Ramoino, H Suzuki, HJ Guntherodt, and TA Jung. Time evolution analysis of a 2d solid-gas equilibrium: a model system for molecular adsorption and diffusion. *Chemical Physics Letters*, 348(3-4):175–181, 2001.
- [9] I. Bezel, K. J. Gaffney, S. Garrett-Roe, S.H. Liu, A.D. Miller, P. Szymanski, and C.B. Harris. Measurement and dynamics of the spatial distribution of an electron localized at a metal-dielectric interface. *J. Chem. Phys.*, 120:845–856, 2004.
- [10] ML Blumenfeld, MP Steele, and OLA Monti. Near- and far-field effects on molecular energy level alignment at an organic/electrode interface. *Journal of Physical Chemistry Letters*, 1(1):145–148, 2010.
- [11] U Bovensiepen, C Gahl, and M Wolf. Solvation dynamics and evolution of the spatial extent of photoinjected electrons in d2o/cu(111). *J. Phys. Chem. B*, 107(33):8706–8715, 2003.
- [12] L Burgi, N Knorr, H Brune, MA Schneider, and K Kern. Two-dimensional electron gas at noble-metal surfaces. *”Applied Physics A—Materials Science & Processing”*, 75(1):141–145, 2002.

- [13] BK Chakrabarti and M Acharyya. Dynamic transitions and hysteresis. *Reviews of Modern Physics*, 71(3):847–859, 1999.
- [14] AR Choudhury, N Winterton, A Steiner, AI Cooper, and KA Johnson. In situ crystallization of low-melting ionic liquids. *Journal of the American Chemical Society*, 127(48):16792–16793, 2005. Cited References Count:30.990QV.AMER CHEMICAL SOC.1155 16TH ST, NW, WASHINGTON, DC 20036 USA.ISI Document Delivery No.:990QV.
- [15] PK Chowdhury, M Halder, L Sanders, T Calhoun, JL Anderson, DW Armstrong, X Song, and JW Petrich. Dynamic solvation in room-temperature ionic liquids. *J. Phys. Chem B*, 108(29):10245–10255, 2004.
- [16] E. V. Chulkov, A. G. Borisov, J. P. Gauyacq, D. Sanchez-Portal, V. M. Silkin, V. P. Zhukov, and P. M. Echenique. Electronic excitations in metals and at metal surfaces. *Chem. Rev.*, 106:4160–4206, 2006.
- [17] T Cremer, M Stark, A Deyko, HP Steinruck, and F Maier. Liquid/solid interface of ultrathin ionic liquid films: [c(1)c(1)lm][tf2n] and [c(8)c(1)im][tf2n] on au(111). *Langmuir*, 27(7):3662–3671, 2011.
- [18] M. F. Crommie, C. P. Lutz, and D. M. Eigler. Confinement of electrons to quantum corrals on a metal-surface. *Science*, 262(5131):218–220, OCT 8 1993.
- [19] JF Douglas, J Dudowicz, and KF Freed. Lattice model of equilibrium polymerization. vii. understanding the role of "cooperativity" in self-assembly. *Journal of Chemical Physics*, 128(22), 2008. Cited References Count:124 Document Delivery No.:312XS.
- [20] MJ Earle and KR Seddon. Ionic liquids. green solvents for the future. *Pure Appl. Chem.*, 72(7):1391–1398, 2000.
- [21] T. Fauster and W. Steinmann. *Electromagnetic Waves*, volume 2, chapter 8. Elsevier, Amsterdam, 1994.
- [22] P. J. Feibelman and D. E. Eastman. Photoemission spectroscopy - correspondence between quantum-theory and experimental phenomenology. *Phys. Rev. B*, 10:4932–4947, 1974.
- [23] R Foulston, S Gangopadhyay, C Chiutu, P Moriarty, and RG Jones. Mono- and multi-layer adsorption of an ionic liquid on au(110). *Phys. Chem. Chem. Phys.*, 14(17):6054–6066, 2012.
- [24] H Fukagawa, S Hosoumi, H Yamane, S Kera, and N Ueno. Dielectric properties of polar-phthalocyanine monolayer systems with repulsive dipole interaction. *Physical Review B*, 83(8), 2011.
- [25] KJ Gaffney, CM Wong, SH Liu, AD Miller, JD McNeill, and CB Harris. Femtosecond electron dynamics at the benzene/ag(111) interface. *Chemical Physics*, 251(1-3):99–110, 2000.
- [26] G GENSTERBLUM, K HEVESI, BY HAN, LM YU, JJ PIREAUX, PA THIRY, R CAUDANO, AA LUCAS, D BERNAERTS, S AMELINCKX, G VANTENDELOO, G BENDELE, T BUSLAPS, RL JOHNSON, M FOSS, R FEIDENHANSL, and G LELAY. Growth mode and electronic-structure of the epitaxial c-60(111)/ges(001) interface. *Physical Review B*, 50(16):11981–11995, 1994.

- [27] TG Gopakumar, T Brumme, J Kroger, C Toher, G Cuniberti, and R Berndt. Coverage-driven electronic decoupling of fe-phthalocyanine from a ag(111) substrate. *Journal of Physical Chemistry C*, 115(24):12173–12179, 2011.
- [28] J. Y. Grand, T. Kunstmann, D. Hoffmann, A. Haas, M. Dietsche, J. Seifritz, and R. Moller. Epitaxial growth of copper phthalocyanine monolayers on ag(111). *Surf. Sci.*, 366(3):403–414, 1996.
- [29] S HASEGAWA, Y NAGAI, T OONISHI, and S INO. Hysteresis in phase-transitions at clean and au-covered si(111) surfaces. *Physical Review B*, 47(15):9903–9906, 1993.
- [30] Richard C. Hatch, David L. Huber, and Hartmut Höchst. Electron-phonon coupling in crystalline pentacene films. *Phys. Rev. Lett.*, 104(4):047601, Jan 2010.
- [31] R Hayes, N Borisenko, MK Tam, PC Howlett, F Endres, and R Atkin. Double layer structure of ionic liquids at the au(111) electrode interface: An atomic force microscopy investigation. *J. Phys. Chem. C*, 115(14):6855–6863, 2011.
- [32] TL HILL. Statistical mechanics of multimolecular adsorption .4. the statistical analog of the bet constant $a_1 b_2 b_1 a_2$ - hindered rotation of a symmetrical diatomic molecule near a surface. *Journal of Chemical Physics*, 16(3):181–189, 1948.
- [33] TL HILL. Statistical mechanics of adsorption .5. thermodynamics and heat of adsorption. *Journal of Chemical Physics*, 17(6):520–535, 1949.
- [34] A. Hotzel, M. Wolf, and J.P. Gauyacq. Phonon-mediated intraband relaxation of image-state electrons in adsorbate overlayers: N-2/Xe/Cu(111). *J. Phys. Chem. B*, 104(35):8438–8455, 2000.
- [35] VM Hultgren, AWA Mariotti, AM Bond, and AG Wedd. Reference potential calibration and voltammetry at macrodisk electrodes of metallocene derivatives in the ionic liquid [bmim][pf6]. *Anal. Chem.*, 74(13):3151–3156, 2002.
- [36] H. Ishii, K. Sugiyama, E. Ito, and K. Seki. Energy level alignment and interfacial electronic structures at organic metal and organic organic interfaces. *Adv. Mat.*, 11(3):605, 1999.
- [37] WH Kirchoff and IW Levin. Description of the thermotropic behavior of membrane bilayers in terms of raman spectral parameters - a 2-state model. *J. Res. Nat. Bur. of Stand.*, 92(2):113–128, 1987.
- [38] F. Klappenberger, D. Kühne, W. Krenner, I. Silanes, A. Arnau, F. J. García de Abajo, S. Klyatskaya, M. Ruben, and J. V. Barth. Tunable quantum dot arrays formed from self-assembled metal-organic networks. *Phys. Rev. Lett.*, 106(2):026802, Jan 2011.
- [39] MN Kobrak and HL Li. Electrostatic interactions in ionic liquids: the dangers of dipole and dielectric descriptions. *Physical Chemistry Chemical Physics*, 12(8):1922–1932, 2010.
- [40] M. Koini, T. Haber, O. Werzer, S. Berkebile, G. Koller, M. Oehzelt, M. G. Ramsey, and R. Resel. Epitaxial order of pentacene on cu(110)-(2 x 1)o: One dimensional alignment induced by surface corrugation. *Thin Solid Films*, 517:483–487, 2008.

- [41] S Krischok, M Eremtchenko, M Himmerlich, P Lorenz, J Uhlig, A Neumann, R Ottking, WJD Beenken, O Hofft, S Bahr, V Kempster, and JA Schaefer. Temperature-dependent electronic and vibrational structure of the 1 ethyl 3 methylimidazolium bis(trifluoromethylsulfonyl)amide room-temperature ionic liquid surface: A study with xps, ups, mies, and hreels. *J. Phys. Chem. B*, 111(18):4801–4806, 2007.
- [42] Ingo Kroeger, Benjamin Stadtmueller, Christoph Stadler, Johannes Zirotz, Mario Kochler, Andreas Stahl, Florian Pollinger, Tien-Lin Lee, Joerg Zegenhagen, Friedrich Reinert, and Christian Kumpf. Submonolayer growth of copper-phthalocyanine on ag(111). *New J. Phys.*, 12:83038, 2010.
- [43] R. D. Kronig and W. G. Penney. Quantum mechanics of electrons on crystal lattices. *Proc. R. Soc. A.*, 130(814):499–513, FEB 1931.
- [44] M. Kulawik, H. P. Rust, M. Heyde, N. Nilius, B. A. Mantooth, P. S. Weiss, and H. J. Freund. Interaction of co molecules with surface state electrons on ag(111). *Surf. Sci.*, 590:253–258, 2005.
- [45] Y Lauw, MD Horne, T Rodopoulos, V Lockett, B Akgun, WA Hamilton, and ARJ Nelson. Structure of [c(4)mpyr][ntf2] room-temperature ionic liquid at charged gold interfaces. *Langmuir*, 28(19):7374–7381, 2012.
- [46] Jun Lei, Hong Sun, K. W. Yu, Steven G. Louie, and Marvin L. Cohen. Image potential states on periodically corrugated metal surfaces. *Phys. Rev. B*, 63(4):045408, Jan 2001.
- [47] A Lewandowski and A Swiderska-Mocek. Ionic liquids as electrolytes for li-ion batteries-an overview of electrochemical studies. *J. Power Sources*, 194(2):601–609, 2009.
- [48] A. L. Linsebigler, G. Q. Lu, and J. T. Yates. Photocatalysis on tio2 surfaces - principles, mechanisms, and selected results. *Chem. Rev.*, 95(3):735–758, 1995.
- [49] SH Liu, AD Miller, KJ Gaffney, P Szymanski, S Garrett-Roe, I Bezel, and CB Harris. Direct observation of two-dimensional electron solvation at alcohol/ag(111) interfaces. *Journal of Physical Chemistry B*, 106(50):12908–12915, 2002.
- [50] Jorge Lobo-Checa, Manfred Matena, Kathrin Muller, Jan Hugo Dil, Fabian Meier, Lutz H. Gade, Thomas A. Jung, and Meike Stohr. Band formation from coupled quantum dots formed by a nanoporous network on a copper surface. *Science*, 325(5938):300–303, 2009.
- [51] K. Manandhar, T. Ellis, K. T. Park, T. Cai, Z. Song, and J. Hrbek. A scanning tunneling microscopy study on the effect of post-deposition annealing of copper phthalocyanine thin films. *Surf. Sci.*, 601(17):3623–2631, 2007.
- [52] CJ Margulis, HVR Annapureddy, PM De Biase, D Coker, J Kohanoff, and MG Del Popolo. Dry excess electrons in room-temperature ionic liquids. *J.A.C.S.*, 133(50):20186–20193, 2011.
- [53] M Marks, C Schmidt, CH Schwalb, T Breuer, G Witte, and U Hofer. Temperature dependent structural phase transition at the perfluoropentacene/ag(111) interface. *J. Phys. Chem. B*, 116(2):1904–1911, 2012.
- [54] M Maroncelli, XX Zhang, M Liang, D Roy, and NP Ernsting. Measurements of the complete solvation response of coumarin 153 in ionic liquids and the accuracy of simple dielectric continuum predictions. *Faraday Discussions*, 154:409–424, 2012.

- [55] H Matsumoto, H Sakaebe, K Tatsumi, M Kikuta, E Ishiko, and M Kono. Fast cycling of li/licoo2 cell with low-viscosity ionic liquids based on bis(fluorosulfonyl)imide [fsi](-). *Journal of Power Sources*, 160(2):1308–1313, 2006.
- [56] A. Mayer. Finite-difference calculation of the green’s function of a one-dimensional crystal: Application to the kronig-penney potential. *Phys. Rev. E*, 74:046708, 2006.
- [57] CP Mehnert, RA Cook, NC Dispenziere, and M Afeworki. Supported ionic liquid catalysis - a new concept for homogeneous hydroformylation catalysis. *J.A.C.S.*, 124(44):12932–12933, 2002.
- [58] A. D. Miller, I. Bezel, K. J. Gaffney, S. Garrett-Roe, S. H. Liu, P. Szymanski, and C.B. Harris. Electron solvation in two dimensions. *Science*, 297(5584):1163–1166, AUG 16 2002.
- [59] AD Miller, I Bezel, KJ Gaffney, S Garrett-Roe, SH Liu, P Szymanski, and CB Harris. Electron solvation in two dimensions. *Science*, 297(5584):1163–1166, 2002.
- [60] T. Miller, W. E. McMahon, and T. C. Chiang. Interference between bulk and surface photoemission transitions in ag(111). *Phys. Rev. Lett.*, 77:1167–1170, Aug 5 1996.
- [61] A. Mugarza, A. Mascaraque, V. Repain, S. Rousset, K. N. Altmann, F. J. Himpsel, Y. M. Koroteev, E. V. Chulkov, F. J. G. de Abajo, and J. E. Ortega. Lateral quantum wells at vicinal au(111) studied with angle-resolved photoemission. *Phys. Rev. B*, 66:245419, FEB 2002.
- [62] M Muntwiler and XY Zhu. Formation of two-dimensional polarons that are absent in three-dimensional crystals. *Physical Review Letters*, 98(24), 2007.
- [63] K. L. Mutolo, E. I. Mayo, B. P. Rand, S. R. Forrest, and M. E. Thompson. Enhanced open-circuit voltage in subphthalocyanine/c-60 organic photovoltaic cells. *J.A.C.S.*, 128:8108–8109, 2006.
- [64] J. E. Ortega, A. Mugarza, V. Repain, S. Rousset, V. Perez-Dieste, and A. Mascaraque. One-dimensional versus two-dimensional surface states on stepped au(111). *Phys. Rev. B*, 65(16):165413, 2002.
- [65] D. G. Oteyza, A. El-Sayed, J. M. Garcia-Lastra, E. Goiri, T. N. Krauss, A. Turak, E. Barrena, H. Dosch, J. Zegenhagen, A. Rubio, Y. Wakayama, and J. E. Ortega. Copper-phthalocyanine based metalorganic interfaces: The effect of fluorination, the substrate, and its symmetry. *J. Chem. Phys.*, 133:214703, 2010.
- [66] V Petrauskas, S Lapinskas, and EE Tornau. Phase diagram of subphthalocyanine ordering on ag(111). *Journal of Chemical Physics*, 120(24):11815–11821, 2004.
- [67] C Pinilla, MG Del Popolo, J Kohanoff, and RM Lynden-Bell. Polarization relaxation in an ionic liquid confined between electrified walls. *J. Phys. Chem. B*, 111(18):4877–4884, 2007.
- [68] B POELSEMA, LK VERHEIJ, and G COMSA. ”direct evidence for two-dimensional xe gas–solid phase-transition on pt(111) by means of thermal he scattering”. *Physical Review Letters*, 51(26):2410–2413, 1983.
- [69] Peter Puschnig, Stephen Berkebile, Alexander J. Fleming, Georg Koller, Konstantin Emtsev, Thomas Seyller, John D. Riley, Claudia Ambrosch-Draxl, Falko P. Netzer, and Michael G. Ramsey. Reconstruction of molecular orbital densities from photoemission data. *Science*, 326(5953):702–706, OCT 30 2009.

- [70] S. Sachs, C.H. Schwalb, M. Marks, A. Scholl, F. Reinert, E. Umbach, and U. Hofer. Electronic structure at the perylene-tetracarboxylic acid dianhydride/ag(111) interface studied with two-photon photoelectron spectroscopy. *J. Chem. Phys.*, 131(14):144701, 2009.
- [71] J. D. Sau, J. B. Neaton, H. J. Choi, S. G. Louie, and M. L. Cohen. Electronic energy levels of weakly coupled nanostructures: C-60-metal interfaces. *Phys. Rev. Lett.*, 101:026804, 2008.
- [72] A Scholl, L Kilian, Y Zou, J Ziroff, S Hame, F Reinert, E Umbach, and RH Fink. Disordering of an organic overlayer on a metal surface upon cooling. *Science*, 329(5989):303–305, 2010.
- [73] KL Sebastian, A Chakraborty, and M Tachiya. The dynamics of solvation of an electron in the image potential state by a layer of polar adsorbates. *Journal of Chemical Physics*, 123(21), 2005.
- [74] M. Shibuta, K. Yamamoto, K. Miyakubo, T. Yamada, and T. Munakata. Resonant effects on two-photon photoemission spectroscopy: Linewidths and intensities of occupied and unoccupied features for lead phthalocyanine films on graphite. *Phys. Rev. B*, 81(11):115426, 2010.
- [75] S Sowmiah, V Srinivasadesikan, MC Tseng, and YH Chu. On the chemical stabilities of ionic liquids. *Molecules*, 14(9):3780–3813, 2009. Cited References Count:147 deleted.
- [76] C Stadler, S Hansen, I Kroger, C Kumpf, and E Umbach. Tuning intermolecular interaction in long-range-ordered submonolayer organic films. *Nature Physics*, 5(2):153–158, 2009.
- [77] Christoph Stadler, Soeren Hansen, Ingo Kroeger, Christian Kumpf, and Eberhard Umbach. Tuning intermolecular interaction in long-range-ordered submonolayer organic films. *Nat. Phys.*, 5(2):153–158, 2009.
- [78] MP Steele, ML Blumenfeld, and OLA Monti. Experimental determination of the excited-state polarizability and dipole moment in a thin organic semiconductor film. *Journal of Physical Chemistry Letters*, 1(13):2011–2016, 2010.
- [79] R. Stiufuc, L. M. A. Perdigão, B. Grandidier, D. Deresmes, G. Allan, C. Delerue, D. Stiévenard, P. H. Beton, S. C. Erwin, M. Sassi, V. Oison, and J.-M. Debierre. Above-barrier surface electron resonances induced by a molecular network. *Phys. Rev. B*, 81(4):045421, Jan 2010.
- [80] ML Strader, S Garrett-Roe, P Szymanski, ST Shipman, JE Johns, A Yang, E Muller, and CB Harris. The ultrafast dynamics of image potential state electrons at the dimethylsulfoxide/ag(111) interface. *J. Phys. Chem. C*, 112(17):6880–6886, 2008.
- [81] Tomohide Takami, Clarisa Carrizales, and K. W. Hipps. Commensurate ordering of iron phthalocyanine on ag(111) surface. *Surf. Sci.*, 603(21):3201–3204, 2009.
- [82] J. Voit, L. Perfetti, F. Zwick, H. Berger, G. Margaritondo, G. Gruner, H. Hochst, and M. Grioni. Electronic structure of solids with competing periodic potentials. *Science*, 290:501–503, 2000.
- [83] HM Wang, SQ Liu, KelongHuang, XG Yin, YN Liu, and SJ Peng. Bmimbf4 ionic liquid mixtures electrolyte for li-ion batteries. *International Journal of Electrochemical Science*, 7(2):1688–1698, 2012.

- [84] P Wang, SM Zakeeruddin, P Comte, I Exnar, and M Gratzel. Gelation of ionic liquid-based electrolytes with silica nanoparticles for quasi-solid-state dye-sensitized solar cells. *J.A.C.S.*, 125(5):1166–1167, 2003.
- [85] W Xu, EI Cooper, and CA Angell. Ionic liquids: Ion mobilities, glass temperatures, and fragilities. *J. Phys. Chem. B*, 107(25):6170–6178, 2003.
- [86] A Yang, ST Shipman, S Garrett-Roe, J Johns, M Strader, P Szymanski, E Muller, and C Harris. Two-photon photoemission of ultrathin film ptcda morphologies on ag(111). *J. Phys. Chem. B*, 112(7):2506–2513, 2008.
- [87] DH Zaitsau, GJ Kabo, AA Strechan, YU Paulechka, A Tschersich, SP Verevkin, and A Heintz. Experimental vapor pressures of 1-alkyl-3-methylimidazolium bis(trifluoromethylsulfonyl) imides and a correlation scheme for estimation of vaporization enthalpies of ionic liquids. *Journal of Physical Chemistry a*, 110(22):7303–7306, 2006.
- [88] X Zhao, BM Sanchez, PJ Dobson, and PS Grant. The role of nanomaterials in redox-based supercapacitors for next generation energy storage devices. *Nanoscale*, 3(3):839–855, 2011. Cited References Count:289 deleted.
- [89] Q Zhou, PD Boyle, L Malpezzi, A Mele, JH Shin, S Passerini, and WA Henderson. Phase behavior of ionic liquid-lix mixtures: Pyrrolidinium cations and tfsi- anions - linking structure to transport properties. *Chemistry of Materials*, 23(19):4331–4337, 2011.
- [90] ZB Zhou, H Matsumoto, and K Tatsumi. Low-melting, low-viscous, hydrophobic ionic liquids: 1-alkyl(alkyl ether)-3-methylimidazolium perfluoroalkyltrifluoroborate. *Chemistry-a European Journal*, 10(24):6581–6591, 2004.
- [91] XY Zhu. Electronic structure and electron dynamics at molecule-metal interfaces: implications for molecule-based electronics. *Surface Science Reports*, 56(1-2):1–83, 2004.
- [92] X.Y. Zhu and C.D. Lindstrom. Image potential states on periodically corrugated metal surfaces. *Chem. Rev.*, 106:4281, Jan 2006.

Chapter 7

Appendix A

Script for Kronig Penney Model

```
%{
```

Kronig Penney Model. Run this as a script from the working directory or as part of the path. This code also requires the functions voight.m, centeredfft.m, and roundarb.m.

This code calculates the energies of the kronig penney band structure at different k-points using a planewave basis. Wavefunctions eigenfunctions are expressed as solutions to the Bloch equation. The code is divided into three sections:

Section 1 Calculates the wavefunction. According to the Bloch equation, the form of the wavefunction is independent of the k-vector, this can be seen from the equation [$\Psi(k)=\Psi(0)*e^{ikr}$]. This is calculated using the separation of variables technique.

Section 2 Fourier Transforms the wavefunction using the centeredfft function. The 1D momentum wavefunction is then formed into a 2D wavefunction, as possible with the separation of variables. These are then normalized and squared to give the probability density.

Section 3 Calculates the band structure of the Kronig Penney Model. The energies are calculated at different angles and radii in order to plot the band structure dispersion. The energies are calculated separately for the x- and y- vectors of the dispersion using separation of variables. Calculations run radially along an angle defined relative to the Gamma-M direction, which corresponds to the x-direction These energies and momenta are then matched with the amplitude of the wavefunction at that point in order to create contourplots. Band width is added as a voigt to represent the instrument response function using the function voight.m. The color of the contourplot represents the amplitude of the signal at different energies and k-vectors.

All input variables and output graphs are in eV and Angstroms

All calculations are performed in atomic units of hartree and bohr.

```
%}
```

```
% *****Section 1*****
```

```
clear
```

```

a=12.7/2;%Size of the box in Angst divided by 2
b=3/2;%Size of the box barrier in Angst divided by 2
c=2^7;%Number of points to sample. Should be >=2^7
e=0.4;%Height of the tunneling barrier in eV

%Solve for the solution at the center of the Brillouin Zone first
%We will FT this to obtain the k-space wavefunction
k=0;
global U;
%Use atomic units for simplicity
eHartree=e/27.2; %hartree
abohr=a/0.52918; %bohr
bbohr=b/0.52918; %bohr
hbar=1; %planck's
mass=1; % m_e
%Discretize the box.
x=linspace(-abohr-bbohr,abohr+bbohr,c); %box with c evenly spaced points
xspace=x(2)-x(1);%space between adjacent points
sect1=length(find(x<-abohr));%number of points defining barrier
sect2=length(x)-2*sect1;%number of points defining well

t=(hbar^2)/(2*mass*((2*abohr+2*bbohr)/c)^2);%Allows discrete secnd deriv.
planewave=exp(i*k*xspace);%k-space sampling

U=[ones(1,sect1) zeros(1,sect2) ones(1,sect1)].*eHartree;%P.E. surface
Usave=U;

%Write matrices
T=2*t*eye(c)-t*planewave*diag(ones(1,c-1),1)...
-t*conj(1)*diag(ones(1,c-1),-1); %Kinetic Energy of of Hamiltonian)
U=diag(U); %Potential Energy as a matrix

%Periodic Boundary Conditions
P=zeros(c,c);
P(1,c)=-t; P(c,1)=conj(-t); %Sets Psi(N)=Psi(1)
P(1,c)=P(1,c)*planewave; %planewave solutions
P(c,1)=P(c,1)*conj(planewave); %planewave solutions

% Sum the parts of the Hamiltonian into a matrix
%uncomment me for nonperiodic conditions
%H=T+U;

%uncomment me for periodic conditions
H=T+U+P;

%Solve for the eigenvalues and eigenvectors
[PSI,evals]=eig(H);
[evals,ind]=sort(real(diag(evals)));

```

```

PSI=PSI(:,ind);
eigenenergies=evals(1:30)*27.2;%Save the lowest 30 eigenenergies
fakephoton=1;%Added for density of final states
%eigenenergies=eigenenergies+fakephoton;

% Vertically plot a the eigenenergies of the lowest eigenenergies
figure(1);hold on;
ylabel( ['Energy (eV)' ],'FontSize',16,'FontName','Helvetica')
for j=1:10
plot(k,eigenenergies(j),'mo');
end

xangst=x*.529; %convert the x-axis to angstroms

%plot the psi^2 in real space
figure(2);
plot(xangst,PSI(:,1:3).*conj(PSI(:,1:3)));
xlabel( ['Momentum ( ' 197 ') ' ^{-1}' ],'FontSize',16,'FontName','Helvetica')
ylabel('PSI^2(x)','FontSize',16,'FontName','Helvetica');
title('RealSpace Wavefunction','FontSize',16,'FontName','Helvetica');
%plot the potential
hold on;plot(xangst,Usave);

% *****Section 2*****
%Fourier Transform each of the three wavefunctions
N=length(PSI(:,1))*2^7;
for ww=1:3;
[YfreqDomain(:,ww),frequencyRange] = centeredFFT(PSI(:,ww),length(xangst),N);
end

%Define the k-axis and plot it
figure(3);
momentumA=frequencyRange*pi/(a+b);
plot(momentumA,YfreqDomain.*conj(YfreqDomain));
xlim([- .31 .31])
xlabel( ['Momentum ( ' 197 ') ' ^{-1}' ],'FontSize',16,'FontName','Helvetica')
ylabel('Amplitude','FontSize',16,'FontName','Helvetica')
title('Using the centeredFFT function','FontSize',16,'FontName','Helvetica')

%This finds and plots a 2D momentum space wavefunction
figure(4);
croph=find(momentumA>=0.4,1); %This is a big matrix, we only want part of it
cropl=find(momentumA<=-0.4,1,'last'); %These crop psi to a reasonable size
% Multiply Psi(x)*Psi(y) to get the 2D wavefunction via sep. of variables.
psi11=YfreqDomain([cropl:croph],1)*(YfreqDomain([cropl:croph],1));
psi12=YfreqDomain([cropl:croph],1)*(YfreqDomain([cropl:croph],2));
psi22=YfreqDomain([cropl:croph],2)*(YfreqDomain([cropl:croph],2));

```

```

psi21=YfreqDomain([cropl:croph],2)*(YfreqDomain([cropl:croph],1))';
psi13=YfreqDomain([cropl:croph],1)*(YfreqDomain([cropl:croph],3))';
psi31=YfreqDomain([cropl:croph],3)*(YfreqDomain([cropl:croph],1))';

%Normalize each of the wavefunctions
psi11=psi11./sqrt(sum(sum(psi11.*conj(psi11))));
psi12=psi12./sqrt(sum(sum(psi12.*conj(psi12))));
psi21=psi21./sqrt(sum(sum(psi21.*conj(psi21))));
psi22=psi22./sqrt(sum(sum(psi22.*conj(psi22))));
psi13=psi13./sqrt(sum(sum(psi13.*conj(psi13))));
psi31=psi31./sqrt(sum(sum(psi31.*conj(psi31))));

%Square to get the probability density
psi11p=psi11.*conj(psi11);
psi12p=psi12.*conj(psi12);
psi21p=psi21.*conj(psi21);
psi22p=psi22.*conj(psi22);
psi13p=psi13.*conj(psi13);
psi31p=psi31.*conj(psi31);

%Plot one of the 2D wavefunctions in k-space
figure;
momentumAcrop=momentumA([cropl:croph]);
contourf(momentumAcrop(1,:),momentumAcrop(1,:),psi12.*conj(psi12),40);
shading flat; xlim([-0.4 0.4]); ylim([-0.4 0.4]);
xlabel( ['Momentum (' 197 ') ' '^{-1}'] , 'FontSize',16, 'FontName', 'Helvetica')
ylabel( ['Momentum (' 197 ') ' '^{-1}'] , 'FontSize',16, 'FontName', 'Helvetica')
title('2D Wavefunction in k-space')

figure;
momentumAcrop=momentumA([cropl:croph]);
contourf(momentumAcrop(1,:),momentumAcrop(1,:),psi13.*conj(psi13),40);
shading flat; xlim([-0.4 0.4]); ylim([-0.4 0.4]);
xlabel( ['Momentum (' 197 ') ' '^{-1}'] , 'FontSize',16, 'FontName', 'Helvetica')
ylabel( ['Momentum (' 197 ') ' '^{-1}'] , 'FontSize',16, 'FontName', 'Helvetica')
title('2D Wavefunction in k-space')

figure;
momentumAcrop=momentumA([cropl:croph]);
contourf(momentumAcrop(1,:),momentumAcrop(1,:),psi22.*conj(psi22),40);
shading flat; xlim([-0.4 0.4]); ylim([-0.4 0.4]);
xlabel( ['Momentum (' 197 ') ' '^{-1}'] , 'FontSize',16, 'FontName', 'Helvetica')
ylabel( ['Momentum (' 197 ') ' '^{-1}'] , 'FontSize',16, 'FontName', 'Helvetica')
title('2D Wavefunction in k-space')

% *****Section 3*****
%Let's try plotting the 3d Psi^2 vs E vs k
%{

```

```

Set the angles. 0degrees corresponds to gamma M and 45 to gamma X.
%angleset can be set to a single angle or multiple angles to allow
%integrating over a solid angle or all radial directions
%}
%angleset=30*pi/180:60*pi/180;
angleset=0*pi/180:30*pi/180:60*pi/180; % Integrate over multiple angles
%angleset=0*pi/180; % Look at only a single angle

radialbins=0.005; %sets the k-point spacing
radialset=0:radialbins:0.4; %the distance into k-space

gamma=find(momentumAcrop==0,1); %Finds the bin of the gamma point

energyspacing=.0005;%changes the spacing for binning the energies
energybins= -0.8:energyspacing:3.2; %Range of energies to plot over
Gfwhm=0.02; %Gaussian FWHM in eV for the Instr Resp Funct
Lfwhm=0.15; %Lorentzian FWHM in eV for the Instr Resp Funct

% Make empty matrices into which the amplitudes will be placed
dispersion11=zeros(length(radialset),length(energybins));
dispersion12=zeros(length(radialset),length(energybins));
dispersion21=zeros(length(radialset),length(energybins));
dispersion22=zeros(length(radialset),length(energybins));
dispersion13=zeros(length(radialset),length(energybins));
dispersion31=zeros(length(radialset),length(energybins));

figure(5);
xlabel( ['Momentum ( ' 197 ') ' ^{-1} ' ],'FontSize',16,'FontName','Helvetica');
ylabel( ['Energy (eV) ' ],'FontSize',16,'FontName','Helvetica');
title('Band Structure','FontSize',16,'FontName','Helvetica');

% Double for loop over the specified set of radii and angles
for angleindex=1:length(angleset);

    angler=angleset(angleindex);
    for radialindex=1:length(radialset);

        radius=radialset(radialindex);

        kx=radius*cos(angler); %Momentum in the x-direction
        planewavex=exp(i*kx*xspace); %Periodic Boundary Conditions
        Px=zeros(c,c);
        Px(1,c)=-t;Px(c,1)=conj(-t);
        Px(1,c)=Px(1,c)*planewavex;
        Px(c,1)=Px(c,1)*conj(planewavex);

        Ux=[ones(1,sect1) zeros(1,sect2) ones(1,sect1)].*eHartree;

```

```

Tx=2*t*eye(c)-t*planewavex*diag(ones(1,c-1),1)...
    -t*conj(planewavex)*diag(ones(1,c-1),-1);
Ux=diag(Ux);
Hx=Tx+Ux+Px; % Hamiltonian for x
[dummy,evals]=eig(Hx);
[evals,ind]=sort(real(diag(evals)));
xenergy=evals(1:3)*27.2;
xenergy=xenergy+fakephoton;

ky=radius*sin(angler); %Momentum in the y-direction
planewavey=exp(i*ky*xspace); %Periodic Boundary Conditions
Py=zeros(c,c);
Py(1,c)=-t;Py(c,1)=conj(-t);
Py(1,c)=Py(1,c)*planewavey;
Py(c,1)=Py(c,1)*conj(planewavey);
Ty=2*t*eye(c)-t*planewavey*diag(ones(1,c-1),1)...
    -t*conj(planewavey)*diag(ones(1,c-1),-1);
Uy=[ones(1,sect1) zeros(1,sect2) ones(1,sect1)].*eHartree;
Uy=diag(Uy);
Hy=Ty+Uy+Py; % Hamiltonian for y
[dummy,evals]=eig(Hy);
[evals,ind]=sort(real(diag(evals)));
yenergy=evals(1:3)*27.2;
yenergy=yenergy;

figure(55);hold on; %Plot Bandstructure
radius_Ang=radius/.529;
plot(radius_Ang,xenergy(1)+yenergy(1),'k.','linewidth',2);
plot(radius_Ang,xenergy(2)+yenergy(1),'k.','linewidth',2);
plot(radius_Ang,xenergy(1)+yenergy(2),'k.','linewidth',2);
plot(radius_Ang,xenergy(2)+yenergy(2),'k.','linewidth',2);
plot(radius_Ang,xenergy(1)+yenergy(3),'k.','linewidth',2);
plot(radius_Ang,xenergy(3)+yenergy(1),'k.','linewidth',2);

plot(-radius_Ang,xenergy(1)+yenergy(1),'k.','linewidth',2);
plot(-radius_Ang,xenergy(2)+yenergy(1),'k.','linewidth',2);
plot(-radius_Ang,xenergy(1)+yenergy(2),'k.','linewidth',2);
plot(-radius_Ang,xenergy(2)+yenergy(2),'k.','linewidth',2);
plot(-radius_Ang,xenergy(1)+yenergy(3),'k.','linewidth',2);
plot(-radius_Ang,xenergy(3)+yenergy(1),'k.','linewidth',2);

figure(22); hold on; %Plot Bandstructure
offset=0.15;
plot(radius_Ang,xenergy(1)+yenergy(1)+offset,'bo','linewidth',2);
plot(radius_Ang,xenergy(2)+yenergy(1)+offset,'bo','linewidth',2);
%plot(radius_Ang,xenergy(2)+yenergy(2)+offset,'bo');
plot(radius_Ang,xenergy(3)+yenergy(1)+offset,'bo','linewidth',2);
plot(radius_Ang,xenergy(1)+yenergy(3)+offset,'bo','linewidth',2);

```

```

plot(-radius_Ang,xenergy(1)+yenergy(1)+offset,'bo','linewidth',2);
plot(-radius_Ang,xenergy(2)+yenergy(1)+offset,'bo','linewidth',2);
%plot(-radius_Ang,xenergy(2)+yenergy(2)+offset,'bo');
plot(-radius_Ang,xenergy(3)+yenergy(1)+offset,'bo','linewidth',2);
plot(-radius_Ang,xenergy(1)+yenergy(3)+offset,'bo','linewidth',2);

% Put the calculated energy of the k-point into bins,
% and store them along with a Voigt width for InstRespFunc.
% roundarb.m puts the eigenenergies into the nearest energy bin.
% voight.m creates a voigt spread in energy around that bin.
xenergy=roundarb(xenergy,energyspacing);
yenergy=roundarb(yenergy,energyspacing);
radialsetA(radialindex)=radialset(radialindex)/.529; %Invers Angstrom

voigt11=voight(energybins-(xenergy(1)+yenergy(1)), [Lfwhm,Gfwhm]);
psi11kxy=psi11p(find(momentumAcrop>=kx,1),find(momentumAcrop>=ky,1));
broadening11=voigt11.*psi11kxy;
dispersion11(radialindex,:)=dispersion11(radialindex,:)+broadening11;
dispersion11(radialindex,:)=dispersion11(radialindex,:);%
dispersion11(radialindex,:)=dispersion11(radialindex,:)*10;

voigt12=voight(energybins-(xenergy(1)+yenergy(2)), [Lfwhm,Gfwhm]);
psi12kxy=psi12p(find(momentumAcrop>=kx,1),find(momentumAcrop>=ky,1));
broadening12=voigt12.*psi12kxy;
dispersion12(radialindex,:)=dispersion12(radialindex,:)+broadening12;
dispersion12(radialindex,:)=dispersion12(radialindex,:);%
dispersion12(radialindex,:)=dispersion12(radialindex,:)*10;

voigt21=voight(energybins-(xenergy(2)+yenergy(1)), [Lfwhm,Gfwhm]);
psi21kxy=psi21p(find(momentumAcrop>=kx,1),find(momentumAcrop>=ky,1));
broadening21=voigt21.*psi21kxy;
dispersion21(radialindex,:)=dispersion21(radialindex,:)+broadening21;
dispersion21(radialindex,:)=dispersion21(radialindex,:);%
dispersion21(radialindex,:)=dispersion21(radialindex,:)*10;

voigt22=voight(energybins-(xenergy(2)+yenergy(2)), [Lfwhm,Gfwhm]);
psi22kxy=psi22p(find(momentumAcrop>=kx,1),find(momentumAcrop>=ky,1));
broadening22=voigt22.*psi22kxy;
dispersion22(radialindex,:)=dispersion22(radialindex,:)+broadening22;
dispersion22(radialindex,:)=dispersion22(radialindex,:);%
dispersion22(radialindex,:)=dispersion22(radialindex,:)*10;

voigt13=voight(energybins-(xenergy(1)+yenergy(3)), [Lfwhm,Gfwhm]);
psi13kxy=psi13p(find(momentumAcrop>=kx,1),find(momentumAcrop>=ky,1));
broadening13=voigt13.*psi13kxy;
dispersion13(radialindex,:)=dispersion13(radialindex,:)+broadening13;
dispersion13(radialindex,:)=dispersion13(radialindex,:);%

```

```

dispersion13(radialindex,:)=dispersion13(radialindex,:)*10;

voigt31=voigt(energybins-(xenergy(3)+yenergy(1)), [Lfwhm,Gfwhm]);
psi31kxy=psi31p(find(momentumAcrop>=kx,1),find(momentumAcrop>=ky,1));
broadening31=voigt31.*psi31kxy;
dispersion31(radialindex,:)=dispersion31(radialindex,:)+broadening31;
dispersion31(radialindex,:)=dispersion31(radialindex,:);%
dispersion31(radialindex,:)=dispersion31(radialindex,:)*10;

end

end

%Plot a sample dispersion of a single band
for i= 1:length(dispersion13(:,1));
dispersion13fd(i,:)=dispersion13(i,:).*1./(exp((energybins-0.95)/.02)+1);
dispersion31fd(i,:)=dispersion31(i,:).*1./(exp((energybins-.95)/.02)+1);
end
figure(6);clf; hold on;
surf(radialsetA(1:20),energybins-1,(dispersion13fd(1:20,:)+
...dispersion31fd(1:20,:))','EdgeColor','none','FaceColor','interp');
figure(6);surf(-radialsetA(1:20),energybins-1,...
(dispersion13fd(1:20,:)+dispersion31fd(1:20,:))',...
'EdgeColor','none','FaceColor','interp');
xlim([-0.33 0.33]);ylim([-0.3 0.05]);
title('psi13','FontSize',16,'FontName','Helvetica');
xlabel( ['Momentum ( ' 197 ') ' ^{-1} ' ],'FontSize',16,'FontName','Helvetica')
ylabel('Energy (eV)', 'FontSize',16,'FontName','Helvetica')

% Add all the bands together to get the dispersion
dispersionT=dispersion11+dispersion12+dispersion21+dispersion22...
+dispersion13+dispersion31;
figure(21); hold on; %Plot the intensities and dispersions as a flat contour
contourf(radialsetA,energybins+offset,dispersionT',30);
contourf(-radialsetA,energybins+offset,dispersionT',30);
shading flat; xlim([-0.3 0.3]);
ylim([(min(energybins)+offset) (max(energybins)+offset)]);
xlabel( ['Momentum ( ' 197 ') ' ^{-1} ' ],'FontSize',16,'FontName','Helvetica')
ylabel( ['Energy (eV)' ],'FontSize',16,'FontName','Helvetica')
title('Calculated Dispersion','FontSize',16,'FontName','Helvetica');

%{
figure(9); hold on; %Plot the intensities and dispersions as a surface
surf(k_pts,Ek(10:150)-curr.hnu+0.13,Z(:,10:150)'
surf(radialsetA,energybins(0:150)+offset,dispersionT',...
'EdgeColor','none','FaceColor','interp');
surf(-radialsetA,energybins+offset,dispersionT',...
'EdgeColor','none','FaceColor','interp');

```

```

xlim([-0.32 0.32]);
xlabel( ['Momentum (' 197 ') ' ^{-1} ' ],'FontSize',16,'FontName','Helvetica')
ylabel('Energy (eV)', 'FontSize',16,'FontName','Helvetica')
title('Calculated Dispersion', 'FontSize',16,'FontName','Helvetica');
%}

%{
figure(9); hold on; %Plot the intensities and dispersions as a surface
surf(radialsetA,energybins(3000:3800)+offset,dispersionT(:,3000:3800)',...
'EdgeColor','none','FaceColor','interp');
surf(radialsetA,energybins(3000:3800)+offset,dispersionT(:,3000:3800)',...
'EdgeColor','none','FaceColor','interp');

xlim([-0.33 0.33]);
xlabel( ['Momentum (' 197 ') ' ^{-1} ' ],'FontSize',16,'FontName','Helvetica')
ylabel('Energy (eV)', 'FontSize',16,'FontName','Helvetica')
title('Calculated Dispersion', 'FontSize',16,'FontName','Helvetica');
%}

*****
function [X,freq]=centeredFFT2(x,Fs,N)
%Original? code found in Matlab online forums.
%fourier transforms while maintaining a proper x-axis
%x is signal, Fs is the sampling rate
%cases for N
if mod(N,2)==0
    k=-N/2:N/2-1; % N even
else
    k=-(N-1)/2:(N-1)/2; % N odd
end
T=N/Fs;    freq=k/T;    %the frequency axis
% FFT!
X=fft(x,N)/Fs; % normalize the data
X=fftshift(X); %shifts (centers) the fft data
*****
function out=roundarb(x,N);
%This function rounds a number, x, to an arbitrary spacing,
%as defined by N.
temp=x/N;temp=round(temp);out=temp*N;

```

Chapter 8

Appendix B

This is code generated for a kinetic Monte Carlo model of phthalocyanines diffusing on Ag(111)

```
call as : [molecules, grid, Erelax, distogram]
= phthego(40,.5,200,5e2,'test1');
```

phthego.m

```
function [molecules, grid, Erelax, distogram] =...
phthego(N,cover,T1,steps,outputname)
%temporary holding area
%{
Sample Command
[molecules, grid Erelax, distogram] = phthalolattice4(110,.2/29.25,300,2e4);
phthalolattice3 fully incorporates phthalocyanine molecules
diffusing on a Ag(111) substrate with rotations included.
phthalolattice4 begins to quantify molecular ordering. A short section at
the end histograms the nearest neighbors of each molecule.
The "4" series has interaction energies, the "5" series doesn't
phthalolattice5 allows "dosing" of molecules without an interaction Energy
phthalolattice4c includes subfunctions in order to make the code shorter
phthalolattice5c incorporates dosing of molecules, subfunctions, and
    interaction energies
phthalolattics5d removes the interaction energies
phthalolattice5d2 fixes normalization for g(r)
phthalolattice4d is a return from the 5 series 5d2. 4d adds interaction
    energies back in and looks for 1rst order phase change in P vs rho
phthego shortens previous code dramatically
by calling on several subfunctions
%}

distogram=[];
outputdirectory='.';
N; cover;T1;steps;E=0;
```

```

grid=zeros(N,N); newgrid=grid;
spp=10;%spp=steps;%Steps per plot. Makes it run faster and plot less often.
Erelax=zeros(1,steps/spp+1);
J = 50; % Strength of interaction (meV)
k = .083; % Kb in meV/K
Gnorm = Radisnorm(N,15);% Set binning for radial distribution
randTol = 1; % prefactor on boltzmann behavior. should be set to 1.

%% Generate an hexagonal grid
Xlength=sin(60*pi/180);
[X Y] = meshgrid(0:1:N-1); %Create meshgrid with correct number of points
X = Xlength * X;%Scale X by size of a hexagon
for i=2:length(Y),%Shift Y values to complete the rotation
    Y(:,i:end)=(Y(:,i:end)+0.5);
end
top= max(max(Y)); %used to set the bounds on the plot

coverage=round(cover*N^2/29.25)
rho=(1:coverage).*29.25/(N.^2);
slowness=zeros([coverage 1]);
Pressure=zeros([coverage 1]);
molecules=zeros([coverage 3]);
newmolecules=molecules;

EnerG=zeros(1,coverage);
Rho1=29.25/N^2;
BNeighbored=zeros(1,coverage);
BUnNeighbored=zeros(1,coverage);
BfreeRho=zeros(1,coverage);
BEnerG=zeros(1,coverage);

%% Place Molecules randomly on the grid
c=0;
while c<coverage;
    tic

    [grid, molecules, c] = addmol(N,grid,molecules,c);

%% Iterate for a defined number of steps
picklength=c;
for g=1:steps/spp,

    %% One time-step is 1 move per molecule
    [molecules,grid] = movestep(molecules,grid,...
    N,picklength,spp,J,T1);
    slowness(c)=toc;

```

```

%{
%% Count Nearest Neighbors to Create a Histogram
%% Distance Histogram & hard disc pressure removed ma17
%% Figure printing for videos went here. removed ma14
%}

end % end of iterations
%{
%% Plot Initial Molecular Centers
fignumber=6;
figure(fignumber);clf;
axis equal; axis square;
fighandle=molplot(N,molecules,fignumber);

%% Plot Initial Grid Occupation
fignumber=6;
figure(fignumber);hold on;
fighandle=gridplot(N,grid,fignumber);
plot(X,Y,'b.', 'MarkerSize',2)

%Calculate Number of Molecules and Energy
M=sum(sum(grid));
xlabel(sprintf('T = %0.2f, M = %0.2f, E = %0.2f,...
step = %0.2f', T1, M/N^2, E/coverage, g*spp));
set(gca,'YTickLabel',[],'XTickLabel',[]);
Erelax(1,g+1)=E/coverage;
%figure(9);plot((spp:spp:steps+spp),Erelax);
%}
save([outputdirectory '/' outputname num2str(c) '.mat'])
%figure(7);
%print('-depsc','-tiff','-r300',...
%[outputdirectory '/' outputname 'figure(7)' num2str(c)])

%{
slowness(c)=toc;
JB=3;
clustergram=clusdentify(molecules,grid,N,JB);
%}
end %we have now reached desired coverage

while c>1,

tic

JB=J*k*T1;
[grid, molecules, c] = rmmol(N,grid,molecules,picklength,JB);

for g=1:steps/spp,

```

```

[molecules,grid] = movestep(molecules,grid,N,c,spp,J,T1);
end

slowness(coverage+c)=toc;
%{
%% Plot Initial Molecular Centers
fignumber=6;
figure(fignumber);clf;
axis equal; axis square;
fighandle=molplot(N,molecules,fignumber);

%% Plot Initial Grid Occupation
fignumber=6;
figure(fignumber);hold on;
fighandle=gridplot(N,grid,fignumber);
plot(X,Y,'b.', 'MarkerSize',2)
%}

save([outputdirectory '/' outputname num2str(c+coverage) '.mat'])
end

***
addmol.m
function [grid, molecules, c] = addmol(N,grid,molecules,c)
%adds a molecule to a random empty spot in a premade grid
placeattempts=0;
while placeattempts<N^2
    %Pick a random spot
    placex=ceil(rand(1)*N);
    placey=ceil(rand(1)*N);
    placerot=ceil(rand(1)*3);
    newmoleculespot=( [placex,placey,placerot] );
    %circleshift the adjacent positions
    for i=1:6;
        xplus(i)=placex+i;
        if xplus(i)>N;
            xplus(i)=xplus(i)-N;
        end
        xminus(i)=placex-i;
        if xminus(i)<1,
            xminus(i)=xminus(i)+N;
        end
        yplus(i)=placey+i;
        if yplus(i)>N;
            yplus(i)=yplus(i)-N;
        end
        yminus(i)=placey-i;
    end
end

```

```

        if yminus(i)<1,
            yminus(i)=yminus(i)+N;
        end
    end
end
% Test if the Spot is Taken
taken = gridcheck(grid,newmoleculespot,N);
placeattempts=placeattempts+1;
% Mark Molecular Position in the Grid
if taken==0;
    grid = gridset(grid,newmoleculespot,N,c);
    c=c+1;
    molecules(c,1)=placex;
    molecules(c,2)=placey;
    molecules(c,3)=placerot;
    placeattempts=placeattempts+9e9;
end
end
end
***
rmmol.m
function [grid, molecules, c] = rmmol(N,grid,molecules,picklenght,JB)
%adds a molecule to a random empty spot in a premade grid
rmattempts=0;
c=picklenght;
while rmattempts<5000,
    %Pick a random spot
    picklenght=find(molecules(:,1)>0,1,'last');
    rmpick=ceil(rand(1)*picklenght);

    %circleshift the adjacent positions
    locatx=molecules(rmpick,1);
    locaty=molecules(rmpick,2);
    locatrot=molecules(rmpick,3);
    for j=1:6;%define nearby spots relative to picked molecule
        oxplus(j)=locatx+j;
        if oxplus(j)>N;
            oxplus(j)=oxplus(j)-N;
        end
        oxminus(j)=locatx-j;
        if oxminus(j)<1,
            oxminus(j)=oxminus(j)+N;
        end
        oyplus(j)=locaty+j;
        if oyplus(j)>N;
            oyplus(j)=oyplus(j)-N;
        end
        oyminus(j)=locaty-j;
        if oyminus(j)<1,
            oyminus(j)=oyminus(j)+N;
    end
end
end

```

```

        end
    end
    % define naborspot
    if locatrot==1;
        naborspot1=( [locatx oyplus(5) locatrot] );
        naborspot2=( [locatx oyminus(5) locatrot] );
        naborspot3=( [oxplus(6) oyminus(3) locatrot] );
        naborspot4=( [oxminus(6) oyplus(3) locatrot] );
    elseif locatrot==2;
        naborspot1=( [oxplus(5) locaty locatrot] );
        naborspot2=( [oxminus(5) locaty locatrot] );
        naborspot3=( [oxplus(3) oyminus(6) locatrot] );
        naborspot4=( [oxminus(3) oyplus(6) locatrot] );
    elseif locatrot==3;
        naborspot1=( [oxplus(3) oyplus(3) locatrot] );
        naborspot2=( [oxminus(3) oyminus(3) locatrot] );
        naborspot3=( [oxplus(5) oyminus(5) locatrot] );
        naborspot4=( [oxminus(5) oyplus(5) locatrot] );
    end

    % Test if the molecule has friends
    nabors=naborspot1+naborspot2+naborspot3+naborspot4;
    rmprob=rand(1);
    rm=(rmprob<nabors);
    rmattempts=rmattempts+1;
    % Mark Molecular Position in the Grid
    if rm==1;
        newmolecules=zeros(picklength-1,3);
        newmolecules(1:picklength-1,:)=molecules(1:picklength-1,:);
        if rmpick<picklength,
            newmolecules(rmpick:end,:)=molecules(rmpick+1:end,:);
        end
        molecules=newmolecules;

        grid=zeros(N,N);
        for w=1:length(molecules(:,1)),
            grid = gridset(grid,molecules(w,:),N,w);
        end

        rmattempts=rmattempts+9000;
        c=picklength-1;
    end
end

***
gridcheck.m
function [taken] = gridcheck(gridin,molecule,N);
% Test if the Spot is Taken

```

```

grid=gridin;
placex=molecule(1,1);
placey=molecule(1,2);
placerot=molecule(1,3);

for i=1:6;
    xplus(i)=placex+i;
    if xplus(i)>N;
        xplus(i)=xplus(i)-N;
    end
    xminus(i)=placex-i;
    if xminus(i)<1,
        xminus(i)=xminus(i)+N;
    end
    yplus(i)=placey+i;
    if yplus(i)>N;
        yplus(i)=yplus(i)-N;
    end
    yminus(i)=placey-i;
    if yminus(i)<1,
        yminus(i)=yminus(i)+N;
    end
end
occupied=0;
if molecule(1,3)==1,
    occupied=grid(xminus(1),yplus(3))+...
    grid(xminus(2),yplus(3))+...
    grid(xplus(1),yminus(3))+...
    grid(xplus(2),yminus(3))+...
    grid(xminus(2),yminus(1))+...
    grid(xminus(3),placey)+...
    grid(xminus(3),yplus(1))+...
    grid(xplus(3),yminus(1))+...
    grid(xplus(3),placey)+...
    grid(xplus(2),yplus(1));

elseif molecule(1,3)==2,
    occupied=grid(xplus(2),yplus(1))+...
    grid(xplus(1),yplus(2))+...
    grid(xplus(2),yminus(3))+...
    grid(xplus(3),yminus(2))+...
    grid(xplus(3),yminus(3))+...
    grid(xminus(2),yminus(1))+...
    grid(xminus(1),yminus(2))+...
    grid(xminus(2),yplus(3))+...
    grid(xminus(3),yplus(2))+...
    grid(xminus(3),yplus(3));

```

```

elseif molecule(1,3)==3,
    occupied=grid(xplus(3),yminus(1))+...
    grid(xplus(3),yminus(2))+...
    grid(xplus(1),yminus(3))+...
    grid(placex,yminus(3))+...
    grid(xminus(1),yminus(2))+...
    grid(xminus(3),yplus(1))+...
    grid(xminus(3),yplus(2))+...
    grid(xminus(1),yplus(3))+...
    grid(placex,yplus(3))+...
    grid(xplus(1),yplus(2));

end

if occupied==0,
    occupied=grid(xplus(2),placey)+...
    grid(xplus(1),yplus(1))+...
    grid(placex,yplus(2))+...
    grid(xminus(1),yplus(2))+...
    grid(xminus(2),yplus(2))+...
    grid(xminus(2),yplus(1))+...
    grid(xminus(2),placey)+...
    grid(xminus(1),yminus(1))+...
    grid(placex,yminus(2))+...
    grid(xplus(1),yminus(2))+...
    grid(xplus(2),yminus(2))+...
    grid(xplus(2),yminus(1));
end

%Checking the center isn't necessary except for error checking
if occupied == 0,
occupied=grid(placex,placey)+...
    grid(placex,yplus(1))+...
    grid(placex,yminus(1))+...
    grid(xplus(1),placey)+...
    grid(xminus(1),placey)+...
    grid(xplus(1),yminus(1))+...
    grid(xminus(1),yplus(1));
end

taken=occupied;

***

gridset.m
function [gridout] = gridset(gridin,molecule,N,value);

```

```

%{
This sets a selection of points on a grid to be a number
where "grid" is the 2D matrix of possible points, and molecule is a 3
vector setting the origin of the particle to be place and the rotation
%}
gridout=gridin;
grid=gridin;
placex=molecule(1,1);
placey=molecule(1,2);
placerot=molecule(1,3);

for i=1:6;
    xplus(i)=placex+i;
    if xplus(i)>N;
        xplus(i)=xplus(i)-N;
    end
    xminus(i)=placex-i;
    if xminus(i)<1,
        xminus(i)=xminus(i)+N;
    end
    yplus(i)=placey+i;
    if yplus(i)>N;
        yplus(i)=yplus(i)-N;
    end
    yminus(i)=placey-i;
    if yminus(i)<1,
        yminus(i)=yminus(i)+N;
    end
end
end
% %{
grid(placex,placey)=value;

grid(placex,yplus(1))=value;
grid(placex,yminus(1))=value;
grid(xplus(1),placey)=value;
grid(xminus(1),placey)=value;
grid(xplus(1),yminus(1))=value;
grid(xminus(1),yplus(1))=value;
% %}
grid(xplus(2),placey)=value;
grid(xplus(1),yplus(1))=value;
grid(placex,yplus(2))=value;

grid(xminus(1),yplus(2))=value;
grid(xminus(2),yplus(2))=value;
grid(xminus(2),yplus(1))=value;

grid(xminus(2),placey)=value;

```

```
grid(xminus(1),yminus(1))=value;
grid(placex,yminus(2))=value;

grid(xplus(1),yminus(2))=value;
grid(xplus(2),yminus(2))=value;
grid(xplus(2),yminus(1))=value;

if molecule(1,3)==1,
    grid(xminus(1),yplus(3))=value;
    grid(xminus(2),yplus(3))=value;

    grid(xplus(1),yminus(3))=value;
    grid(xplus(2),yminus(3))=value;

    grid(xminus(2),yminus(1))=value;
    grid(xminus(3),placey)=value;
    grid(xminus(3),yplus(1))=value;

    grid(xplus(3),yminus(1))=value;
    grid(xplus(3),placey)=value;
    grid(xplus(2),yplus(1))=value;

elseif molecule(1,3)==2,
    grid(xplus(2),yplus(1))=value;
    grid(xplus(1),yplus(2))=value;

    grid(xplus(2),yminus(3))=value;
    grid(xplus(3),yminus(2))=value;
    grid(xplus(3),yminus(3))=value;

    grid(xminus(2),yminus(1))=value;
    grid(xminus(1),yminus(2))=value;

    grid(xminus(2),yplus(3))=value;
    grid(xminus(3),yplus(2))=value;
    grid(xminus(3),yplus(3))=value;

elseif molecule(1,3)==3,
    grid(xplus(3),yminus(1))=value;
    grid(xplus(3),yminus(2))=value;

    grid(xplus(1),yminus(3))=value;
    grid(placex,yminus(3))=value;
    grid(xminus(1),yminus(2))=value;

    grid(xminus(3),yplus(1))=value;
    grid(xminus(3),yplus(2))=value;
```

```

    grid(xminus(1),yplus(3))=value;
    grid(placedx,yplus(3))=value;
    grid(xplus(1),yplus(2))=value;

end
gridout=grid;

***
gridplot.m
function fighandle=gridplot(N,grid,fignumber);
Xlength=sin(60*pi/180);
[X Y] = meshgrid(0:1:N-1);
top= max(max(Y));
gridx=zeros(length(sum(sum(grid))));
gridy=gridx;
count=0;
for i=1:N,
    for j=1:N,
        if grid(i,j)>=1,
            count=count+1;
            gridx(count)=Xlength*(i-1);
            gridy(count)=(j-1)+(i-1)*.5;
        end
    end
end
figure(fignumber);
fighandle=plot(gridx,gridy,'k. ');
%xlim([-1 top]);ylim([-1 top]);

***

molplot.m
function distogram=radiald(Gnorm,molecules,picklength,N);
%Determines radial distances on a hexagonal grid with PBC
% Detailed explanation goes here

    Gnorm(1,2)=3*(N^2/(29.25));
    distogram=Gnorm;
    distogram(:,2)=0;
    for i=1:picklength,
        for j=1:picklength,
            if molecules(i,1)>molecules(j,1),
                dxprd=N-molecules(i,1)+molecules(j,1);
                dxreg=molecules(i,1)-molecules(j,1);
                dxmin=min(dxprd,dxreg);
                directionx=(dxprd<dxreg)*2-1;
            end
        end
    end
end

```

```

elseif molecules(i,1)<molecules(j,1),
    dxprd=N-molecules(j,1)+molecules(i,1);
    dxreg=molecules(j,1)-molecules(i,1);
    dxmin=min(dxprd,dxreg);
    directionx=-(dxprd<dxreg)*2+1;
else
    dxmin=0;
    directionx=1;
end
if molecules(i,2)>molecules(j,2),
    dyprd=N-molecules(i,2)+molecules(j,2);
    dyreg=molecules(i,2)-molecules(j,2);
    dymin=min(dyprd,dyreg);
    directiony=(dyprd<dyreg)*2-1;
elseif molecules(i,2)<molecules(j,2),
    dyprd=N-molecules(j,2)+molecules(i,2);
    dyreg=molecules(j,2)-molecules(i,2);
    dymin=min(dyprd,dyreg);
    directiony=-(dyprd<dyreg)*2+1;
else
    dymin=0;
    directiony=1;
end
distance=sqrt((dxmin+.5*sign(directionx*directiony)*dymin)^2+...
    (sin(pi/3)*dymin)^2);
binspot=find(distance<=Gnorm(:,1),1);
distogram(binspot,2)=distogram(binspot,2)+1;

end
end
distogram(:,2)=((N^2)/(29.25*(picklength-1)))*3*distogram(:,2);

***

movestep.m
function [molecules,grid] =...
    movestep(molecules,grid,N,picklength,spp,J,T1)
% Moves molecules on the grid 1 time each *spp
% Detailed explanation goes here
randTol=1;
k = .083; % Kb in meV/K
for h=1:picklength*spp,

    %% Pick a Molecule

    pick=ceil(rand(1)*picklength);
    molecule=molecules(pick,:);

```

```

%% Define Adjacent Spaces
up=[1 0 0]+molecule;
if up(1,1)>N;
    up(1,1)=1;
end
down=[-1 0 0]+molecule;
if down(1,1)<1;
    down(1,1)=N;
end
right=[0 1 0]+molecule;
if right(1,2)>N;
    right(1,2)=1;
end
left=[0 -1 0]+molecule;
if left(1,2)<1;
    left(1,2)=N;
end
upleft=[1 -1 0]+molecule;
if upleft(1,2)<1;
    upleft(1,2)=N;
end
if upleft(1,1)>N;
    upleft(1,1)=1;
end
downright=[-1 1 0]+molecule;
if downright(1,2)>N;
    downright(1,2)=1;
end
if downright(1,1)<1;
    downright(1,1)=N;
end
clock=[0 0 1]+molecule;
if clock(1,3)>3;
    clock(1,3)=1;
end
counterclock=[0 0 -1]+molecule;
if counterclock(1,3)<1;
    counterclock(1,3)=3;
end

%% guess direction
direction=(ceil(rand(1)*8));%Set to 8 for all moves allowed
newmolecule=[0 0 0];
if direction==1;
    newmolecule=up;
elseif direction==2;

```

```

    newmolecule=down;
elseif direction==3;
    newmolecule=left;
elseif direction==4;
    newmolecule=right;
elseif direction==5;
    newmolecule=upleft;
elseif direction==6;
    newmolecule=downright;
elseif direction==7;
    newmolecule=clock;
elseif direction==8;
    newmolecule=counterclock;
end

%% Define New Spot
placex=newmolecule(1,1);
placey=newmolecule(1,2);
placerot=newmolecule(1,3);
%% circleshift the New adjacent positions
for i=1:6;
    xplus(i)=placex+i;
    if xplus(i)>N;
        xplus(i)=xplus(i)-N;
    end
    xminus(i)=placex-i;
    if xminus(i)<1,
        xminus(i)=xminus(i)+N;
    end
    yplus(i)=placey+i;
    if yplus(i)>N;
        yplus(i)=yplus(i)-N;
    end
    yminus(i)=placey-i;
    if yminus(i)<1,
        yminus(i)=yminus(i)+N;
    end
end

end

% circleshift the old adjacent positions
locatx=molecule(1,1);
locaty=molecule(1,2);
locatrot=molecule(1,3);
for i=1:6;
    oxplus(i)=locatx+i;
    if oxplus(i)>N;
        oxplus(i)=oxplus(i)-N;
    end
end

```

```

    oxminus(i)=locatx-i;
    if oxminus(i)<1,
        oxminus(i)=oxminus(i)+N;
    end
    oyplus(i)=locaty+i;
    if oyplus(i)>N;
        oyplus(i)=oyplus(i)-N;
    end
    oyminus(i)=locaty-i;
    if oyminus(i)<1,
        oyminus(i)=oyminus(i)+N;
    end
end

% Delete Molecule from Old Grid Postions
newgrid=grid;
newgrid = gridset(newgrid,molecule,N,0);

% Look to See if Spot is Taken
taken = gridcheck(newgrid,newmolecule,N);

%% attempt move
if taken==0;
    %% Cases of molecule orientations
    if locatrot==1;
        naborspot1=( [locatx oyplus(5) locatrot] );
        naborspot2=( [locatx oyminus(5) locatrot] );
        naborspot3=( [oxplus(6) oyminus(3) locatrot] );
        naborspot4=( [oxminus(6) oyplus(3) locatrot] );
    elseif locatrot==2;
        naborspot1=( [oxplus(5) locaty locatrot] );
        naborspot2=( [oxminus(5) locaty locatrot] );
        naborspot3=( [oxplus(3) oyminus(6) locatrot] );
        naborspot4=( [oxminus(3) oyplus(6) locatrot] );
    elseif locatrot==3;
        naborspot1=( [oxplus(3) oyplus(3) locatrot] );
        naborspot2=( [oxminus(3) oyminus(3) locatrot] );
        naborspot3=( [oxplus(5) oyminus(5) locatrot] );
        naborspot4=( [oxminus(5) oyplus(5) locatrot] );
    end

    %% Count Old Nearest Neighbors
    nabors=0;
    for i=1:picklength,
        if molecules(i,:)==naborspot1;
            nabors=nabors+1;
        elseif molecules(i,:)==naborspot2
            nabors=nabors+1;

```

```

elseif molecules(i,')==naborspot3
    nabors=nabors+1;
elseif molecules(i,')==naborspot4
    nabors=nabors+1;
end
end
end

%% Define Location of Potential Nearest Neighbors for Rotation
if placerot==1;
    newnaborspot1=( [placex yplus(5) placerot] );
    newnaborspot2=( [placex yminus(5) placerot] );
    newnaborspot3=( [xplus(6) yminus(3) placerot] );
    newnaborspot4=( [xminus(6) yplus(3) placerot] );
elseif placerot==2;
    newnaborspot1=( [xplus(5) placey placerot] );
    newnaborspot2=( [xminus(5) placey placerot] );
    newnaborspot3=( [xplus(3) yminus(6) placerot] );
    newnaborspot4=( [xminus(3) yplus(6) placerot] );
elseif placerot==3;
    newnaborspot1=( [xplus(3) yplus(3) placerot] );
    newnaborspot2=( [xminus(3) yminus(3) placerot] );
    newnaborspot3=( [xplus(5) yminus(5) placerot] );
    newnaborspot4=( [xminus(5) yplus(5) placerot] );
else
    disp('error in placerot')
end

%% Count New Nearest Neighbors
newnabors=0;
for i=1:picklength,
    if molecules(i,')==newnaborspot1
        newnabors=newnabors+1;
    elseif molecules(i,')==newnaborspot2
        newnabors=newnabors+1;
    elseif molecules(i,')==newnaborspot3
        newnabors=newnabors+1;
    elseif molecules(i,')==newnaborspot4
        newnabors=newnabors+1;
    end
end

%% Find Energy and Probability of Hop
DeltaE = J *(newnabors-nabors);
p_trans = randTol*exp(DeltaE/(k * T1));
hop = (rand(1) < p_trans );

%Make Hop

```

```
if hop ==1
    % Make the hop on the vector
    molecules(pick,:)=newmolecule;
    % Set grid to be the old grid minus the new molecule
    grid=newgrid;
    grid = gridset(grid,newmolecule,N,pick);
    %disp('successful move');

end
elseif taken>0;
    %disp('occupied!!');
end % End of 1 move attempt

end %end of 1 full step (times spp)
end

***
```